

TIME-RESOLVED STRUCTURAL INVESTIGATIONS
ON BIOLOGICAL MACROMOLECULES

by

Tek Narsingh Malla

A Dissertation Submitted in
Partial Fulfillment of the
Requirements for the Degree of

Doctor of Philosophy
in Physics

at

The University of Wisconsin-Milwaukee

December 2023

ABSTRACT
TIME-RESOLVED STRUCTURAL INVESTIGATIONS ON BIOLOGICAL
MACROMOLECULES

by

Tek Narsingh Malla

The University of Wisconsin-Milwaukee, 2023
Under the Supervision of Professor Marius Schmidt

X-ray crystallography is a key method in determining the 3-dimensional (3D) structures of proteins at near atomic resolution. A more complete understanding of the protein function requires that structural changes are investigated as they happen during reaction. With time-resolved crystallography (TRX), it is possible to unify protein structure determination with reaction dynamics. A reaction is initiated in a macromolecular crystal, and the resulting change in the structure is investigated by X-ray diffraction. The structures of intermediates that form and decay during the reaction can be determined. Similarly, the fundamental displacements of atoms associated with chemical reactions in proteins can be observed.

In the last decade, X-ray free electron laser (XFEL) facilities became available for macromolecular structure determination. X-rays generated by XFELs feature highly brilliant, femtosecond (fs) pulses. Good quality diffraction data can be collected from a microcrystal with a single X-ray pulse that lasts only a few fs. This enormous X-ray intensity destroys the crystal after a single exposure. Due to the ultrashort nature of the X-ray pulses, a diffraction pattern is recorded before the crystal is destroyed. A complete radiation damage free dataset is, therefore, collected from thousands of tiny crystals serially injected into the X-ray interaction region. Since each diffraction is collected from a fresh crystal, reversible and irreversible reactions may be studied equally well at room temperatures.

If the protein is naturally photoactive, the reaction can be initiated (pumped) by exposing the crystal to a laser light pulse with an appropriate wavelength. After a delay (that can be femtoseconds or longer) the resulting change is probed by an X-ray pulse. For non-photosensitive proteins a more general method to trigger a reaction is required. Mix-and-inject serial crystallography (MISC) was developed to explore irreversible enzymatic reactions. Microcrystals are mixed with a substrate before injecting the mixture into the X-rays. The diffusion of the substrate into the active sites of the enzymes inside the crystal starts the reaction. The resulting structural changes are investigated by X-rays.

In this dissertation results from four projects are described that involve enzymes suitable for time-resolved structure determination. In the first project MISC is applied to understand the inhibition of the Mycobacterium tuberculosis beta(β) lactamase enzyme (BlaC) by a suicide inhibitor. Here, the β -lactam inhibitor sulbactam is used and mixed with BlaC microcrystals. From a time series of MISC data spanning from 3 ms to 700 ms, ligand gating and tunneling, cooperativity, induced fit and conformational selection mechanisms are observed and described with near-atomic precision.

The second project aims at the determination of the structure of the main protease (Mpro) of the severe acute respiratory syndrome coronavirus 2 (SARS-CoV-2) at room temperature. This structure was determined at an XFEL during the COVID-19 pandemic. It will be a prerequisite for future MISC experiments.

In a third project, early events of signal propagation in a photoactive enzyme called phytochrome are investigated. X-ray structures were determined at an XFEL on picosecond (ps) time-scales

using the pump probe technique. A reaction is started with a 640 nm laser light pulse. The ps structural changes show how the central chromophore responds to photon absorption.

Large flexible proteins are difficult to crystallize and are unsuitable for investigation with crystallography. In these cases, structures can be determined using single particle cryo-EM. Here, the structure of a full length intact phytochrome has been determined with cryo-EM. This structure is the starting point for future, ground-breaking time-resolved experiments with cryo-EM.

© Copyright by Tek Narsingh Malla, 2023
All Rights Reserved

To the members of
हाम्रो सानो घर,

कृष्ण बहादुर मल्ल
झीना कुमारी मल्ल
नमिता मल्ल
ममता मल्ल

TABLE OF CONTENTS

ABSTRACT.....	ii
LIST OF FIGURES	xi
LIST OF TABLES.....	xiii
ACKNOWLEDGEMENTS.....	xiv
1. Introduction	1
1.1 Background	1
1.2 Proteins.....	1
1.3 Imaging with X-rays.....	3
1.3.1 X-ray crystallography	3
1.3.2 Macromolecular X-ray crystallography	4
1.3.3 Macromolecular X-ray crystallography at Synchrotron Light Sources	5
1.3.4 Laue crystallography and time-resolved crystallography	6
1.3.5 Third-generation synchrotron sources	8
1.3.6 The X-ray free electron laser	10
1.3.7 Current state of Time-Resolved X-ray crystallography	11
1.4 Imaging with electrons	12
1.4.1 The roots of electron microscopy	12
1.4.2 Electron microscopy	13
1.5 Proteins investigated and reported in this thesis	14
2. Theories and principles.....	17
2.1 Theory of X-ray diffraction.....	17
2.1.1 Scattering by atoms.....	17
2.1.2 Scattering by a molecule	18
2.1.3 Scattering by a crystal.....	19
2.1.4 Reflection through crystal.....	21
2.1.5 Reciprocal Lattice	21
2.1.6 Ewald sphere.....	22
2.1.7 Structural heterogeneity	23
2.1.8 Mosaicity.....	24
2.1.8 The phase problem.....	25
2.2 Theory of transmission electron microscopy	26
2.2.1 Electron generation	26
2.2.2 Image formation.....	27

2.3	Sample preparation.....	29
2.3.1	Protein overexpression.....	30
2.3.2	Protein purification	30
2.3.3	Protein crystallization	31
2.4	Crystallography data collection.....	31
2.4.1	The rotation method.....	32
2.4.2	Processing of data from the single crystal rotation method.....	32
2.4.3	Serial crystallography	33
2.4.4	Data processing for serial crystallography.....	36
2.5	Time-Resolved Serial Femtosecond Crystallography (TR-SFX)	38
2.5.1	Pump-Probe TR-SFX.....	38
2.5.2	Mix-and-Inject Serial Crystallography (MISC).....	39
2.6	Crystallographic data analysis.....	43
2.6.1	Electron density maps and structure determination	43
2.6.2	Difference electron density maps.....	44
2.6.3	Omit difference map	45
2.6.4	Extrapolated electron density map.....	45
2.6.5	Analysis of DED maps by singular value decomposition	46
2.7	Cryo-EM.....	48
2.7.1	Cryo-EM data collection.....	49
2.7.2	Cryo-EM data processing and analysis.....	51
2.8	Application of the methods discussed above to various protein samples	55
3.	Beta (β) Lactamase	56
3.1	Introduction	56
3.2	Methods.....	60
3.2.1	Protein purification and crystallization.....	60
3.2.2	Data collection	61
3.2.3	Difference maps and structure determination	64
3.2.4	Adapting singular value decomposition for non-isomorphous datasets	65
3.2.5	Characterization of inhibitor diffusion and concentrations of intermediates.....	70
3.3	Results	73
3.3.1	Binding of sulbactam to BlaC.....	73
3.3.1	Temporal variation of difference electron density.....	76
3.3.3	Characterization of inhibitor diffusion and concentrations of intermediates.....	79

3.4	Discussion	82
3.4.1	Comparison of kinetics in subunits B/D versus A/C	82
3.4.2	Rapid diffusion and binding of sulbactam in BlaC microcrystals	84
3.4.4	The fate of the <i>trans</i> -enamine	85
3.5	Outlook.....	88
4.	Phytochrome.....	89
4.1	Introduction	89
4.2	Methods.....	93
4.2.1	Protein purification and crystallization.....	93
4.2.2	TR-SFX data collection	94
4.2.3	TR-SFX difference maps and structure determination	96
4.2.4	Cryo-EM data collection.....	97
4.2.5	Cryo-EM map reconstruction and structure determination	99
4.3	Results	100
4.3.1	Pump-probe TR-SFX at MFX and CXI.....	100
4.4.2	Cryo-EM structure of full length phytochrome	102
4.4	Discussion	105
4.4.1	Reaction initiation in SaBphP2 phytochrome.....	105
4.4.2	Full length phytochrome in Pr/Pfr heterodimeric form	107
4.4.3	Allosteric signal transfer in phytochrome.....	108
4.5	Outlook.....	111
5.	SARS CoV-2 Main Protease (3CLpro or Mpro).....	112
5.1	Introduction	112
5.2	Methods.....	114
5.2.1	Protein purification and crystallization.....	114
5.2.2	Data collection	115
5.2.3	Structure determination.....	117
5.2.4	Molecular docking simulations.....	118
5.3	Results	119
5.3.1	Three different crystal forms	119
5.3.1	Ebselen reacts with 3CLpro crystals.....	119
5.3.3	Binding of ligands to the 3CLpro	120
5.4	Discussion	122
5.4.1	Structure plasticity of the active site of 3CLpro	122

5.4.1	Potential binding of ascorbate to the 3CLpro	125
5.5	Outlook.....	127
6.	Summary.....	128
	References.....	129
	Curriculum Vitae	151

LIST OF FIGURES

Figure 1.1	Composition of protein	2
Figure 1.2	Length scale of important biological objects	3
Figure 2.1	Scattering of X-rays by an atom	17
Figure 2.2	Structure of a crystal	19
Figure 2.3	Ewald sphere construction	23
Figure 2.4	A schematic of magnetic lens	27
Figure 2.5	Single crystal method for X-ray crystallography	32
Figure 2.6	Serial crystallography setup	34
Figure 2.7	Schematics of a Gas Dynamic Virtual Nozzle	35
Figure 2.8	A schematic layout of AGIPD multi panel X-ray detector	37
Figure 2.9	Schematics for the two types of time-resolved serial crystallography	38
Figure 2.10	Cross section of the mixing injector	40
Figure 2.11	Diffusion inside a crystal	41
Figure 2.12	Singular Value Decomposition	47
Figure 2.13	Cross sectional schematics of transmission electron microscope	51
Figure 2.14	Typical work flow for cryo-EM data processing with <i>cryoSPARC</i> program	54
Figure 3.1	Structure of β -lactamase, ceftriaxone and sulbactam	57
Figure 3.2	Simplified mechanism of sulbactam inhibition reaction of BlaC	59
Figure 3.3	Structure of BlaC crystal	60
Figure 3.4	Flow chart for an SVD analysis	67
Figure 3.5	Establishing the region of interest from DED maps	69
Figure 3.6	A simple two-step mechanism of BlaC inhibition by sulbactam	71
Figure 3.7	BlaC gating mechanism	72
Figure 3.8	Difference electron density maps at the active site of subunit A	74
Figure 3.9	Difference electron density maps at the active site of subunit B	76
Figure 3.10	Right singular vectors	77
Figure 3.11	Concentration profile of reacting species in the active sites of subunits B/D	79
Figure 3.12	Concentration profile of reacting species in the active sites of subunits A/C	81
Figure 3.13	DED maps of the cryosoaked data	86

Figure 3.14	TEN on longer timescale	87
Figure 4.1	Full length structure of SaBPhP2	90
Figure 4.2	The photocycle of a typical bacteriophytochrome	92
Figure 4.3	Pump-probe data collection scheme	95
Figure 4.4	Reconstruction of cryo-EM map	100
Figure 4.5	TR-SFX structures of the SaBphP2 on the picosecond time scale	101
Figure 4.6	The cryo-EM map and structure of full length phytochrome	103
Figure 4.7	Comparison between crystal and cryo-EM structure	104
Figure 4.8	Close view on the structural changes of ring D at 3 ps	105
Figure 4.9	Close view on the structural changes of ring D at 100 ps	106
Figure 4.10	Signal transfer in bacteriophytochrome	109
Figure 5.1	The biologically active form of 3CLpro	112
Figure 5.2	Chemical structures of compounds detected near the active site of 3CLpro	113
Figure 5.3	Molecular docking	117
Figure 5.4	Different crystal forms of 3CLpro	118
Figure 5.5	Low resolution diffraction pattern of 3CLpro	119
Figure 5.6	ASC and DTT bound in the active site of 3CLpro	121
Figure 5.7	Comparison of room and cryo temperature structures of 3CLpro	123
Figure 5.8	Plasticity of 3CLpro	124
Figure 5.9	Interaction pattern of the ASC and TFE with the active site of 3CLpro	126

LIST OF TABLES

Table 3.1	Injector geometry and sample flow rates	62
Table 3.2	Data collection statistics for BlaC	63
Table 3.3	Refinement statistics for BlaC	65
Table 3.4	Important distances in the active centers of subunit A and B	75
Table 3.5	Relaxation times and amplitudes of right singular vectors	78
Table 3.6	Characterization of SUB diffusion and reaction rate coefficients	80
Table 4.1	SFX data collection statistics for phytochrome	95
Table 4.2	Cryo-EM data collection and refinement statistics	98
Table 5.1	Data collection and refinement statistics for 3CLpro	116

ACKNOWLEDGEMENTS

During the course of my PhD program, I have received unimaginable support and assistance.

First and foremost, I would like to express my deepest gratitude to my supervisor and mentor Professor Marius Schmidt. Without his support and guidance, it would not have been possible to carry on the research work and make it into the final shape of this dissertation. His enthusiasm and dedication for research excellence is contagious and motivational, which has shaped me to become a better researcher. I am extremely grateful towards my committee members and collaborators Professor Peter Schwander and Professor Emina Stojkovic. Emina and her lab has supported unmeasurably with samples for different experiments, and Peter played a pivotal role in kickstarting the cryo-EM project. I am also equally grateful to other committee members Professor Valerica Raicu and Professor Ionel Popa for taking time to serve on this committee. I have learnt a lot from them not only as members of committee and their insights during preliminary examination, but also from their classes.

The projects that I have been part of became fruitful only because of the combined effort of a lot of collaborators who participated. I am particularly grateful to Lois Pollack and her team for making injectors for the BlaC project. In addition, I would like to thank George Philips, Petra Fromme, Sebastian Westenhoff, Joshua Mendez and their teams for continuous collaboration. I would also like to thank all the scientists at LCLS, EuXFEL, SACLA, ESRF, APS, NYSBC who collected the data for our experiments.

I thank the past members of the Schmidt lab, Ishwor and Suraj who helped me grasp a strong knowledge on the lab when I had none. I also thank the present lab members Gabriel, Srinivasan, Prabin and Shishir for all the lively group discussions.

My gratitude extends to the staff in the UWM Physics department, who has supported in myriad ways outside of research. I take this opportunity to thank my professors and teachers from undergraduate, high school and school who helped me find my way towards science and research.

Lastly, I would like to thank my family for their love, care and support. My deepest respect and admiration to my parents Krishna Malla and Jheena Malla for the sacrifices they have made for me and the family. A mountain of respect to my sisters Nameeta Malla and Mamata Malla who I consider second only to my parents. Finally, lots of love to my girlfriend Cassy Broeren, for always supporting and encouraging me especially during my lowest times. This achievement belongs to all of us.

1. Introduction

1.1 Background

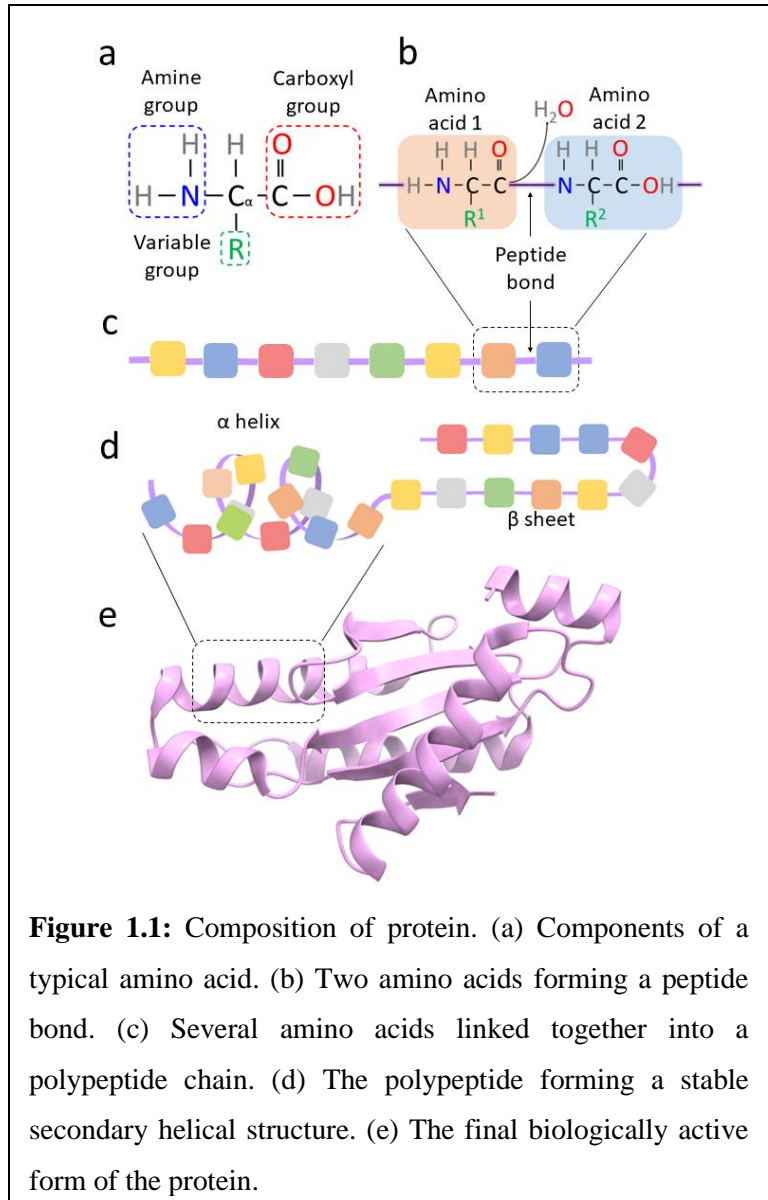
The cell is the structural and functional unit of all living organisms (Alberts et al., 2022). Each cell hosts many types of biomolecules to perform its functions. They range from large macromolecules like proteins, deoxy ribonucleic acids (DNA), ribonucleic acids (RNA), to small molecules like lipids, carbohydrates water, ions, nutrients, etc. Biological macromolecules are in charge for a variety of functions essential for the growth and survival of living organisms (Dhara & Nayak, 2022). Proteins are of special interest. They are very versatile and do most of the work in the cells (Raicu & Popescu, 2008). They replicate and transcribe DNA, produce and process other proteins. They participate in metabolism, cell division, and the flow of matter and information through the cell membrane. Some may provide structure and rigidity to the organisms. Understanding how proteins function is the first step to the understanding how life works.

1.2 Proteins

Proteins are biological macromolecules made up of small compounds called amino acids (Popa & Berkovich, 2023). Each amino acid contains a central carbon atom (C_{α}), an amino group, a carboxyl group, and a side chain (Fig. 1.1 a). The side chain, also called the R-group (R for *residue*), is the only component that differs among amino acids. It determines the type and the characteristics (size, charge and polarity) of the amino acids. There are only 20 biogenic amino acids, and all proteins found in organisms are combinations of these amino acids.

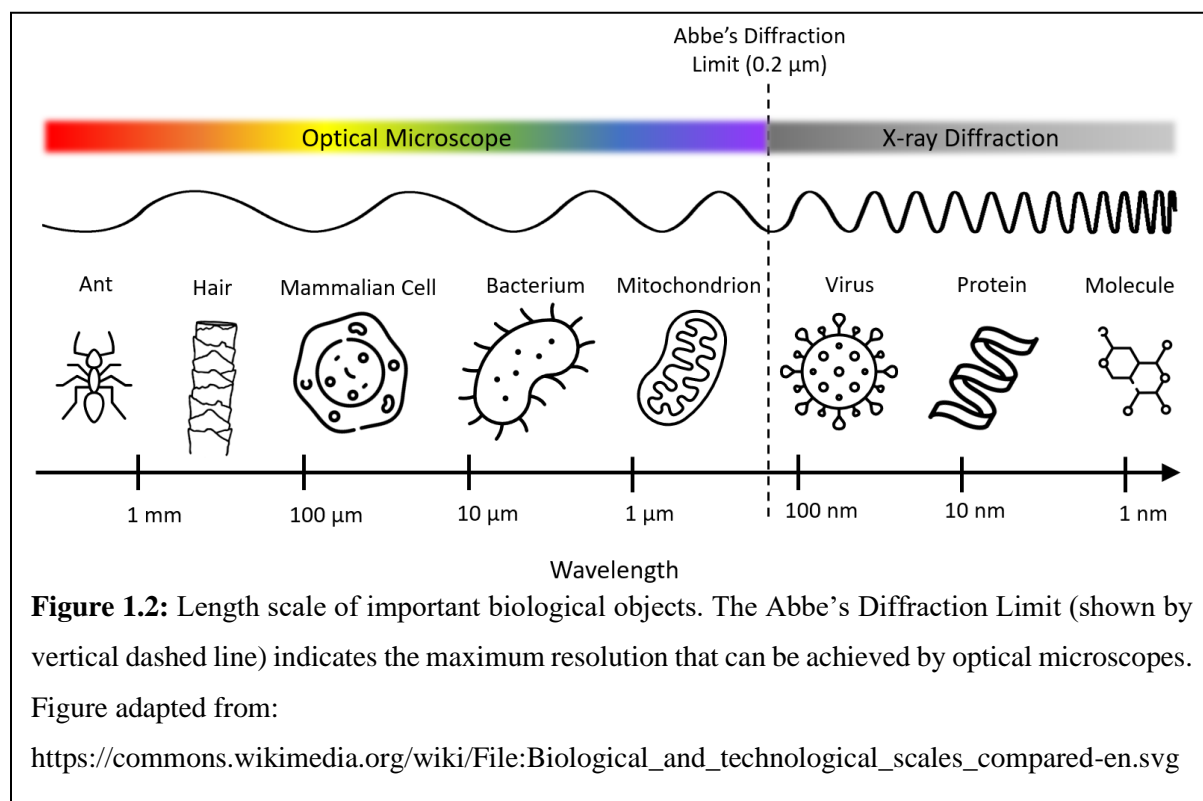
Amino acids can bind to one another by establishing a peptide bond between them (Fig. 1.1 b) to form a long polypeptide chain (Fig. 1.1 c). The sequence of the amino acids determines the way the chain will fold (Popa & Berkovich, 2023). The polypeptides go through successive levels of

folding to form secondary structure elements such as α -helices and β -sheets as shown in (Fig. 1.1 d). The secondary structure elements will further fold into a unique tertiary structure (Fig. 1.1 e). Folding patterns are mediated by several non-covalent interactions between the residues such as electrostatic interactions, hydrogen bonds, hydrophobic packing, Van der Waals forces and polar interactions. Certain proteins can have more than one polypeptide chain linked together to form a quaternary structure.



The function of protein depends on its complex 3D structure (Hess & Rupley, 1971). A defect during protein synthesis will result in a misshaped protein. The severity of misfolded proteins ranges from losing their normal function to outright toxicity in cells (Luheshi et al., 2008). Such proteins are linked to human diseases like Alzheimer's, Parkinson's and many others (Dobson, 2003). To understand the functions of proteins, it is essential to determine their structure at the molecular level.

A typical human cell contains from 20,000 to over 100,000 types of proteins averaging 2.5 nm in size (Netzer & Hartl, 1998). This size is much smaller than an optical microscope can resolve. Light can only resolve elements of a structure that are larger than about half the wavelength of the light. As the lowest wavelength of the visible spectrum is around 400 nm, the maximum resolution achievable is ~200 nm (Abbe, 1873). To reach near atomic resolution, comparably shorter wavelengths are necessary. Suitable wavelengths are in the X-ray regime of the electromagnetic spectrum (Fig. 1.2). Alternately, a beam of electrons can also be used to illuminate and image the specimen.



1.3 Imaging with X-rays

1.3.1 X-ray crystallography

X-rays are electromagnetic (EM) waves whose wavelengths lie between 0.01 nm and 10 nm in the EM spectrum. They were discovered in 1895 by Wilhelm Conrad Röntgen (Röntgen,

1898). X-rays are highly energetic and penetrating radiation that cannot be focused by lenses. However, they scatter weakly when they interact with the electron cloud of the atoms. In 1912, Max von Laue and colleagues showed that X-rays are diffracted by crystals of the mineral zinc sulfide (Friedrich et al., 1913). The scattered waves from different atoms arranged in periodic order in crystals will interfere with each other, producing a diffraction pattern (DP). Essentially, the crystal behaves like a 3D diffraction grating for X-rays (Mair, 1926). In 1913, William Lawrence Bragg and William Henry Bragg introduced a formula for determining an object's structure based on the pattern formed by X-rays. They reasoned that the positions of the diffraction spots depend on the size and shape of the molecules inside the crystal. They published the structure of small salt molecules using X-ray diffraction photographs (M. W. L. Bragg et al., 1913; W. H. Bragg & Bragg, 1913). Furthermore, the intensities diffracted into the diffraction spots are related to the electron density distribution of the molecules in the crystal (Von Laue et al., 1962). The structure is obtained by placing atoms into the electron density map. That was the cornerstone for structure determination using X-ray diffraction. Theory and more details will be presented in Chapter 2.

1.3.2 Macromolecular X-ray crystallography

The structures of many inorganic and organic molecules were determined in the subsequent years using X-ray crystallography. Then in 1934, J. Desmond Bernal and Dorothy Crowfoot observed X-ray diffraction from hydrated pepsin protein crystals (Bernal & Crowfoot, 1934). Proteins were known to crystallize almost a century before this. However, this observation made it clear that the structure of proteins can be studied by crystallizing them. Finally, the first 3D structure of a protein was solved by John C. Kendrew and his colleagues in 1958 (Kendrew et al., 1958) at a resolution of 6 Å. The team used the naturally occurring crystals of the sperm whale myoglobin discovered on ship decks. Two years later, the group solved the structure of myoglobin

at 2 Å resolution (Kendrew et al., 1960), reaching the near atomic resolution milestone for protein structures. Five years later in 1965, Blake and colleagues published the structure of Hen Egg-White Lysozyme, the first structure of an enzyme (Blake et al., 1965). Until then, the data were collected at room temperature over a duration of days or even weeks. During data collection, the protein crystals can suffer radiation damage from the ionizing X-rays. Sometimes crystals had to be replaced and the complete dataset is collected from multiple crystals. A publication in 1970 by David J. Haas demonstrated reduced radiation damage in protein crystals (Haas, 1968) when the crystals were cryo-cooled with liquid nitrogen. At the same time, more powerful X-ray sources (discussed in the next section) became available that significantly reduced the time required to collect a dataset. Cryo-cooling was not used seriously until the invention of the cryo-loop in the 1990s (Teng, 1990). Since then, cryo-cooling is universally used with intense synchrotron sources (Haas, 2020).

1.3.3 Macromolecular X-ray crystallography at Synchrotron Light Sources

Synchrotrons were first introduced in 1940s to study collisions between high energy particles (Elder et al., 1947). In synchrotrons, charged particles travel close to the speed of light in a curve path. When relativistic charged particles like electrons are subjected to acceleration, synchrotron radiation (SR) is emitted. SR spans a broad range of wavelengths, from the visible to hard X-rays, each with very high brilliance. The bright light generated by these 1st-generation synchrotrons were unwanted in the collision experiments. Protein crystallographers started making use of the X-rays drawn from a particle collider (Phillips et al., 1976). Being much brighter than home laboratory sources, the number of experiments using synchrotron light increased. Realizing the potential of powerful X-rays for biological application, work began on the development of 2nd-generation synchrotron sources dedicated to the production of X-rays. X-rays were generated using

bending magnets. The first 2nd-generation synchrotron was commissioned by the UK in 1980 (Munro, 1997). Apart from high brilliance, another advantage of the synchrotrons is the ability to change the wavelength of the X-ray beam. Tunable wavelength motivated the development of the anomalous dispersion technique (Keenan et al., 1988). In contrast to already existing methods, it provided an easier and direct solution to the *phase problem* (see section 2.1.8) in crystallography. This *de novo* phasing opened up the avenue for wider range of proteins to be investigated for structure determination.

1.3.4 Laue crystallography and time-resolved crystallography

The availability of polychromatic synchrotron radiation led to renewed interest in Laue crystallography. When a stationary crystal is illuminated by a polychromatic beam of X-rays, a Laue diffraction pattern is generated (Moffat et al., 1984). Although Laue diffraction was widely used for structure analysis in the early days of crystallography, it was quickly superseded by simpler and more readily quantifiable monochromatic techniques (Moffat, 2006). When monochromatic X-ray radiation is used, the crystal needs to be rotated. The rotation ensures that the integrated reflection intensity is recorded for each reciprocal lattice point (the theory is discussed more in chapter 2). The long exposure times required to collect the integrated reflection intensities with the rotation method limits the speed with which the data can be acquired. In contrast, with the polychromatic beam (Moffat, 2019) more reciprocal lattice points can be sampled within a single exposure. No rotation is necessary. Laue patterns can be obtained in less than 1 second, and significant radiation damage does not occur over the course of an exposure (Moffat et al., 1984).

The structures obtained from X-ray diffraction are static in nature. Although they may provide some insight into protein function, it is difficult to visualize dynamics (Moffat, 2001, 2014) with

static structures alone. Proteins undergo several conformational changes while they perform their functions. To thoroughly understand how proteins work, one must also observe how the structure changes as protein perform their functions. This is possible with time-resolved crystallography (TRX) (Moffat, 1989). A reaction is triggered in crystals such as by photoexcitation in case of photoactive proteins or more generally, by chemical mixing (Bourgeois & Royant, 2005; Schmidt, 2020). Several intermediates may form and decay during the reaction. Distinct intermediate states are probed by X-rays to determine their structure. Each structure acts as a snapshot of a reaction in progress. When many X-ray datasets are collected during the reaction, it is possible to infer the dynamics of the of the crystalline ensemble by determining relative occupancies of the intermediate states visited by reacting molecules during the reaction.

With the Laue technique, multiple diffraction patterns can be collected from the same crystal at ambient temperature. The first TRX experiments were conducted by rapidly initiating reaction in crystals by a laser light pulse (Schlichting et al., 1990; Šrajer et al., 1996). A dataset is collected in the dark (without laser illumination) as a reference. A reaction can then be triggered in the same crystal by illuminating with an appropriate laser light pulse (pump pulse). After the reaction is initiated, the progress of the reaction may be examined with an X-ray pulse (probe pulse) at a time-delay Δt . The pump-probe technique is expanded upon in section 2.5.1. In addition, the Laue method has been applied to the study of ligand photolysis, enzymatic reactions, etc (Šrajer et al., 1996; Stoddard et al., 1998).

The broad bandwidth X-rays used in Laue crystallography can produce streaky reflections that cannot be easily analyzed. Good crystals with small mosaic spreads (around 0.1°) are required. Many protein crystals show much larger mosaicities, since they can be fragile and receptive to

long range dislocations. Despite the improvements been made in experimental or computational approaches to streamline the analysis of the Laue data (Ren et al., 1999), the full treatment of the distribution of single and multiple Laue spots, an assessment of the extent of the overlapping orders problem proved challenging. For quantitative measurements of more complicated structures, Laue diffraction was thus largely supplanted by the somewhat simpler monochromatic diffraction (Moffat, 2019).

1.3.5 Third-generation synchrotron sources

Third-generation synchrotrons were designed to significantly increase the intensity and stability of the X-ray radiation. These synchrotrons made use of insertion devices called wigglers and undulators (Helliwell, 1992). These devices were inserted in straight sections between the bending magnets that kept the electron beam on a circle. Several such facilities became operational in the 1990s starting with European Synchrotron Radiation Facility (ESRF) in Grenoble, France (Lieuvin, 1994). An equivalent of a 24-hour exposure at a laboratory source can be achieved in few seconds. The Advanced Photon Source (APS) located at Argonne National Laboratory in Illinois is the closest advanced X-ray source to the Schmidt lab at the University of Wisconsin-Milwaukee. Some of the experiments described in this thesis were performed at APS beamline 19-ID-D. 19-ID-D is designed for monochromatic X-rays. It can produce a flux of 1.5×10^{12} photons/sec at 12.6 keV (Rosenbaum et al., 2006).

These synchrotron sources are built as national research facilities. General users can access and use the synchrotron. Both Laue and monochromatic techniques experienced widespread adoption and technological advancements (Ihee et al., 2005; Jung et al., 2013; Schmidt et al., 2004; Schotte et al., 2003, 2012). By the year 2000 more structures were determined using synchrotron sources

than with X-ray generators in individual laboratories (Grabowski et al., 2021). The structure of one of the largest protein complexes, the 30S ribosomal subunit, was also solved in the year 2000 with data collected at 3rd-generation synchrotron sources (Wimberly et al., 2000). Today, at the state-of-art synchrotrons such as the APS, complete datasets can be measured in seconds with crystal rotation speeds exceeding 90° s^{-1} and detector frame rates exceeding 100 Hz (Young et al., 2021). The diffraction quality is monitored in real time and transferred to automated processing pipelines to simplify data analysis (Holton & Alber, 2004; Monaco et al., 2013). Despite these advantages, there are certain limitations inherent with the synchrotron technology which are outlined below.

i. Even with the brilliance available at 3rd generation synchrotron sources, it is still difficult to obtain a DP from an X-ray pulse generated by a single electron bunch. This required either an increase in exposure time or the growth of large crystals. Growing large crystals is not easy and has been extensively discussed elsewhere (McPherson, 1991; Rayment, 2002).

ii. Longer exposure times lead to significant radiation damage. The effect might be subtle as loss in high-resolution data to severe structural damage of protein molecules (Garman & Owen, 2006). This problem is dealt with by keeping the crystals at cryogenic temperatures during data collection (Hope, 1988). However, cryo-cooling might have an impact on the determination of the protein structure in its physiological state. It also renders the protein nonfunctional as most of the dynamics is frozen out.

iii. The temporal resolution of time-resolved experiment at a synchrotron is limited by the pulse duration of the X-rays (~100 ps). Only intermediates that are populated on longer timescales (> 100 ps) can be investigated. Other important intermediates that are generated on significantly faster timescales cannot be assessed (Jung et al., 2013).

iv. Since a single X-ray pulse does not have enough photons (see also (i)). Diffraction from multiple X-ray pulses must be accumulated on the detector. This means mainly cyclic reactions can be studied in time-resolved fashion. In cyclic reactions, the crystalline protein returns to the reference state. A new pump-probe sequence can be applied and the diffraction data superposed on the previously collected data. In irreversible cases, the protein ends up in a state different from the reference state, and the experiment cannot be repeated. This becomes even more problematic when monochromatic X-rays are used. For each rotation, the crystal must be brought back to its original state and the pump-probe sequence repeated.

1.3.6 The X-ray free electron laser

At X-ray free electron laser (XFEL) facilities, X-rays are generated by the principle of self-amplified spontaneous emission (SASE) (Huang & Kim, 2007; Madey, 1971). Electrons are accelerated to relativistic speed. They pass through long undulators banks that consist of alternating magnets that force the electron onto a sinusoidal trajectory. This causes the electrons to emit X-rays. The electrons further interact with their own radiation field. Through this interaction all electrons begin emitting coherent radiation. The result is an exponential increase of X-ray-radiation. This leads to high beam intensities and laser-like properties.

The first XFEL, the Linac Coherent Light Source (LCLS), became operational in 2009 at Stanford Linear Accelerator Center (SLAC) National Laboratory in California (Emma et al., 2010). The LCLS can produce 10^{12} photons per pulse which is about 100 times larger than that found in the broadband synchrotron radiation ($\sim 10^{10}$ photons per pulse). The spectral bandwidth of X-rays generated by XFELs is also about a factor of 25 smaller (0.2 % compared to 5 % for X-rays generated by synchrotron sources). Consequently, the number of photons per 0.1% bandwidth is

about 2500 times larger compared to synchrotron radiation. Because the XFEL emits spatially coherent X-rays, the beam can be well focused without loss onto a spot much smaller than 1 μm . The peak brilliance of LCLS is a billion times greater than that at the most powerful 3rd-generation synchrotrons (Robinson et al., 2010). Currently, five XFELs are operational and several others are under construction.

Due to the large brilliance, diffraction data can be collected from small crystals. With the ultrashort pulses, diffraction occurs much faster than the time required for radiation damage to evolve. The diffraction patterns are essentially damage-free. This principle called ‘diffraction before destruction’ was first proposed by computer simulation (Neutzo et al., 2000) and later experimentally verified (Chapman et al., 2006, 2011). The intense XFEL pulse damages the crystal upon single fs exposure. A new crystal is required for each exposure which led to the development of serial crystallography (discussed more in chapter 2). Since the crystal cannot be rotated during the ultrashort X-ray pulse, each DP is a still image. Only partial reflection intensities are collected. To obtain the integrated reflection intensity (details in section 2.4.3) the partial intensities observed in a large number of DPs are averaged. Since each crystal is exposed in random orientation, this method has been called Monte Carlo averaging (Kirian et al., 2011). As a fresh crystal must be provided each time, the need for cryo-cooling is alleviated, and the protein molecules can be studied at physiological temperature. Because each diffraction image is serially obtained from a fresh crystal, reversible and irreversible processes may be investigated in the same manner. With the ultrashort fs pulses, the temporal resolution can be extended to the fs regimes.

1.3.7 Current state of Time-Resolved X-ray crystallography

TRX is booming with the advent of XFELs. Advancement in this technique now allows the structure determination of reaction products on the femtosecond time scale (Tenboer et al.,

2014). This is a revolutionary advancement in the domain of ultrafast structural biology. Conformational changes on the time scale of chemical bond dissociation (Barends et al., 2015) or isomerization (Claesson et al., 2020; Pande et al., 2016), and the electron transfer between cofactors can now be studied (Dods et al., 2020). X-ray crystallography has been elevated to a new level (Schmidt, 2019, 2020).

The popularity and the capability of X-ray crystallography is evident in the depositions at the Protein Data Bank (PDB) (Berman et al., 2000). The PDB is an online database for storing experimentally determined 3D structures of proteins, nucleic acids and complex assemblies. At the time of writing, there are ~200,000 structures of macromolecules deposited in the PDB. More than 85% (174,000) of all the structures have been determined by X-rays.

1.4 Imaging with electrons

1.4.1 The roots of electron microscopy

Electrons were discovered by J.J. Thomson in 1897 (Thomson, 1897). In 1924 Louis de Broglie introduced the idea that electrons are not only particles but also have wave-like character (Broglie, 2009). Han Bush, in 1926, suggested that magnetic and electric fields could be used to direct the beams of electrons in a way similar to how light is refracted by optical lenses (Busch, 1926). His proof that a small angle electron beam can be focused to a point by a cylindrical magnetic lens was the foundation of electron microscopy. Building upon this idea, Ernst Ruska and Max Knoll created the first electron microscope in 1931 (E. Ruska & Knoll, 1931). Details up to 450 μm could be resolved, which was still within the limit of conventional optical microscopy. Two years later, Ernst Ruska developed the original model further. With this, he was able to go beyond the resolution limit of optical microscopy (E. Ruska, 1934). In 1937, he was joined by

Helmut Ruska and Bodo von Borries to build an electron microscope for biological application (H. Ruska et al., 1939). Using this microscope, ‘sub-microscopic’ structures of bacteriophages and various viruses were investigated.

1.4.2 Electron microscopy

In 1969, De Rosier and Klug used electron microscope images to calculate a 3D map of the tail of bacteriophage T4 (De Rosier & Klug, 1968). Later in 1975, Joachim Frank introduced the single particle analysis method (Frank, 1975). This study provided the framework for taking noisy microscopy data for large numbers of biomolecules, averaging them and ultimately convert them into a potential map. The images produced by electron microscopy suffered from extremely low signal-to-noise ratio. Increasing the electron dose damages the delicate biological samples beyond use. In 1981, Jacques Dubochet and colleagues demonstrated a technique how sub 1 μm thick vitrified water films can be produced. The water film is rapidly frozen by immersing it into liquid ethane (Dubochet & McDowell, 1981). Vitrification increases the resolution by reducing electron induced radiation (Henderson, 1990), by protecting the samples in the vacuum environment and by locking water molecules in place around samples. The same team, in 1984, presented micrographs of single, undamaged virus particles embedded within a layer of vitrified water (Adrian et al., 1984). Cryogenic electron microscopy (cryo-EM) was born. The introduction of direct electron detectors in 2000s vastly improved the signal-to-noise ratio (Milazzo et al., 2011) of the collected micrographs. In previous detectors, electrons are incident on a scintillator in which they are converted to photons. These photons are then transferred to the sensor of the detector via a fiber optic plate. Noise and loss of signal increase due to electron to photon conversion in a scintillator, and photon transfer through a fiber-optic. Direct detectors eliminate such systematic noises and produce clearer micrographs. Continuous progress in microscope hardware

complemented by improved software and computing power made it possible that cryo-EM structures can be determined with near atomic resolution.

In current cryo-EM experiments, an electron beam travels through the vitrified protein sample capturing a 2D view, or projection, of the specimen. Since the proteins are frozen in random orientations, exposure with the electrons will produce a variation of projections, each from a different orientation. These projections are averaged together to generate higher signal to noise ratio which show much more detail than the individual projections. The 2D projections are combined again into a 3D reconstruction of the molecule (Further details are presented in chapter 2).

One advantage of cryo-EM over X-ray crystallography is that crystallization is not required. Crystallization requires large quantity of pure protein and can be very time consuming (Callaway, 2015). Large flexible proteins and complexes are challenging to crystallize. Some proteins may not crystallize at all (Gorrec, 2021). Because of this cryo-EM is becoming a popular method in the past few years. In 2015 there were only ~1000 cryo-EM structures in the PDB which has surged past 15,000 in just 7 years.

1.5 Proteins investigated and reported in this thesis

During my PhD I have been involved in several projects with varying level of involvements. Only three of them are reported in this dissertation. In these projects, I have been involved in sample preparation before the experiment, data collection during the experiment, data analysis after the experiment, and writing manuscripts. The underlying theme for all projects is to understand the dynamics of the proteins.

All projects are concerned with establishing ways to perform time-resolved experiments. TRX was traditionally performed on photoactive proteins due to the relative ease of the pump-probe technique. As such, it was easier to apply the same method when serial crystallography was introduced at XFELs. A pioneering experiment was performed on photoactive yellow protein (PYP) which showcased the capacity of room temperature serial crystallography in time-resolved studies (Tenboer et al., 2014). However, PYP is a small protein and is already well studied. Soon, the focus was shifted towards bigger proteins. One such protein studied in our lab is the phytochrome (Carrillo et al., 2021; Sanchez et al., 2019). The phytochrome is a photoreceptor which regulates various essential physiological processes in plants, fungi and bacteria (Nagatani, 2010). Upon photoexcitation, the protein undergoes distinct conformational changes on ps to ms timescales. In this protein, we are investigating the early stages of signal propagation upon photoexcitation using pump-probe TRX.

Enzymes that catalyze essential life functions are usually not photoactive by nature with few exceptions like phytochrome. Before XFELs became available, TRX experiments on enzymes were limited. They made use of inactive, caged substrates that can be activated by a laser pulse (Schlichting et al., 1990; Stoddard et al., 1998). More general methods to trigger reactions in enzymes are required. In one of these methods, called the mix-and-inject serial crystallography (more in section 2.5.2), substrate is mixed with enzyme microcrystals to trigger reactions chemically. Our laboratory in collaboration with multiple researchers pioneered this method by using β -lactamase a model system. The β -lactamase enzyme confers antibiotic resistance in bacteria. Thus, it is a prime drug target for novel therapeutics. The experiment set the scene for structure-based enzymology at XFELs. Following that, few more experiments were performed that helped establish the technique as a go-to for TRX experiments in enzymes (Olmos et al., 2018;

Pandey et al., 2021). In the current project presented here, we are pushing the boundaries of structure-based enzymology. From the same set of X-ray data, ligand gating and tunneling, cooperativity, induced fit and conformational selection mechanisms are observed and described with near-atomic precision. At the same time, it shines light on working mechanism of antibiotic degradation, and enzyme inhibition at the molecular level.

With the lesson learned from β -lactamase in TRX, we were aiming to perform similar experiments with the main protease of the severe acute respiratory syndrome coronavirus 2 (SARS-CoV-2). SARS-CoV-2 is the causative agent of covid-19 disease and the pandemic. The main protease is a key enzyme in coronaviruses and has a crucial role in virus replication. In addition, we wanted to assess the viability of repurposing existing drugs as effective and immediate treatments.

With cryo-EM the structures of large flexible proteins can be investigated that are otherwise hard to crystallize. Here, structures of a myxobacterial full length, intact phytochrome are determined with cryo-EM. These structures will lay the foundation for future time-resolved experiments with cryo-EM.

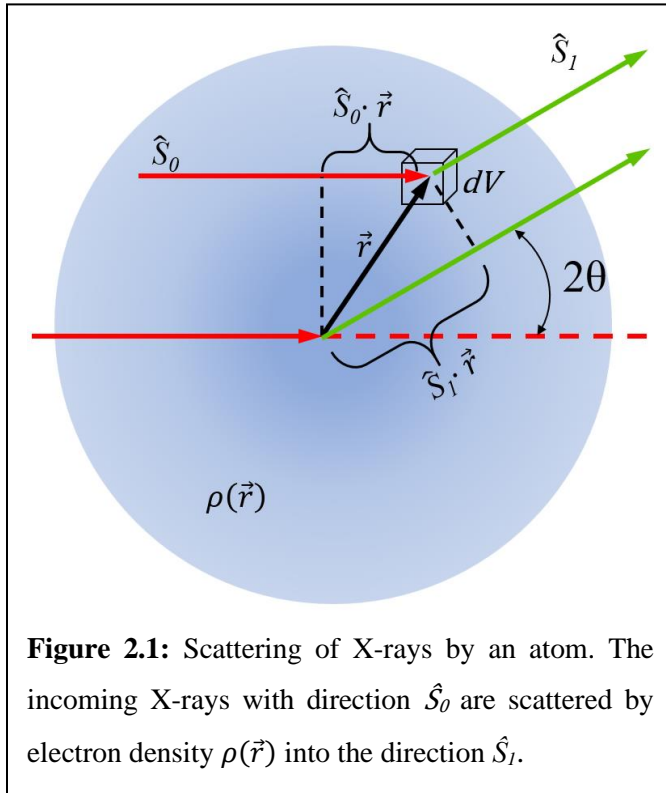
2. Theories and principles

This chapter offers in depth detail about the theory and principles behind each imaging technique. In section 2.1, the theory of X-ray diffraction is presented. Likewise, in section 2.2, the theory of imaging by electron microscopy is described.

2.1 Theory of X-ray diffraction

2.1.1 Scattering by atoms

Charged particles oscillate upon interacting with the electric field of the electromagnetic radiation like X-rays. Since the nucleus is orders of magnitude heavier than the electrons, X-rays are scattered by the electron cloud of the atom. The elastic scattering of the radiation from an electron is governed by Thomson scattering. The cross section of this process is known as the Thomson cross section.



Consider scattering from an infinitesimal volume element dV (Fig. 2.1) within the spherical electron cloud of an atom. The path difference (δ) between the incoming rays from direction \hat{S}_0 scattered into direction \hat{S}_1 is given by,

$$\delta = \hat{S}_1 \cdot \vec{r} - \hat{S}_0 \cdot \vec{r} = \hat{S} \cdot \vec{r} \quad 2.1$$

where $\hat{S} = \hat{S}_1 - \hat{S}_0$. The phase difference φ is

$$\varphi = \frac{2\pi}{\lambda} \times \delta = 2\pi \vec{H} \cdot \vec{r}, \text{ with } \vec{H} = \frac{\hat{S}}{\lambda} \quad 2.2$$

The scattering from the volume element is identical to that of Thomson scattering by a single electron, but it is weighted with the probability of finding an electron in the volume element i.e.

$$\sqrt{\sigma_e} \rho(\vec{r}) dV \quad 2.3$$

where $\sqrt{\sigma_e}$ is the Thomson scattering length (equivalent to the classic electron radius).

The total scattering is obtained by integration over the whole electron density distribution of an atom as

$$f(\vec{H}) = \sqrt{\sigma_e} \int \rho(\vec{r}) e^{2\pi i \vec{H} \cdot \vec{r}} dV . \quad 2.4$$

$f(\vec{H})$ in Eqn. 2.4 is called the *atomic form factor* (or the *atomic scattering factor*). The *atomic form factor* is the measure of the scattering power of an isolated atom. It decreases as the scattering angle increases. The *atomic form factor* for each atom and its angular dependence are experimentally determined and are available from *International Table of Crystallography*.

Also, it is important to note from Eqn. 2.4 that the *atomic form factor* is the Fourier transform of the electron density of the atom.

2.1.2 Scattering by a molecule

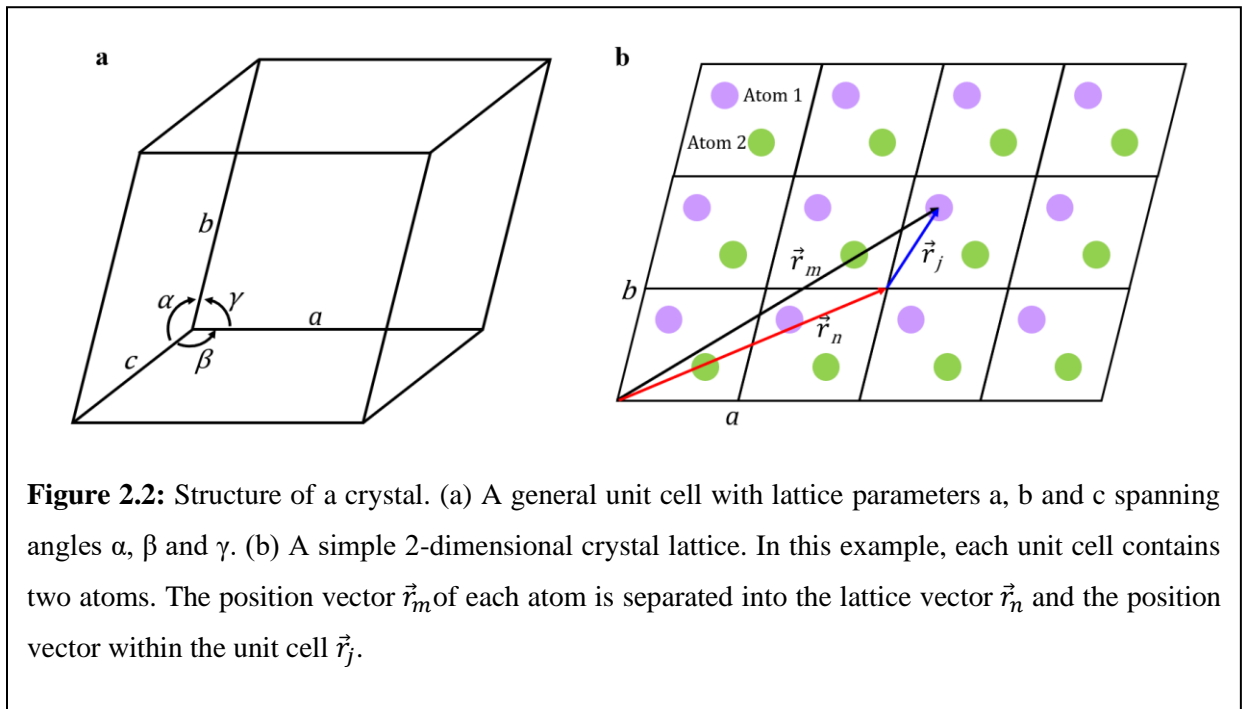
A molecule is a group of atoms, each scattering the incident X-rays according to their form factors. For a molecule consisting of J atoms, the *structure factor of the molecule* is given by

$$F^M(\vec{H}) = \sum_{j=1}^J f_j e^{2\pi i \vec{H} \cdot \vec{r}_j} \quad 2.5$$

The sum is taken over all J atoms located at positions \vec{r}_j with each atom scattering with its atomic form factor f_j .

2.1.3 Scattering by a crystal

A crystal is a periodic array of atoms or molecules in three dimensions. The smallest repeating unit in the crystal is called a unit cell. The shape of any unit cell is described by three vectors \vec{a} , \vec{b} , \vec{c} which have lengths a, b, c , and angles α , β , γ in between (Fig. 2.2 a). These vectors are called the crystallographic axes of the unit cell. The lengths and angles are known as the lattice constants or lattice parameters.



The *structure factor of the crystal* may be calculated as

$$F^C(\vec{H}) = \sum_{m=1}^M f_m e^{2\pi i \vec{H} \cdot \vec{r}_m} \quad 2.6$$

where the sum is taken over all M atoms in the crystal.

Since the crystal is periodic, the position vector of each atom, \vec{r}_m , is a vector sum of \vec{r}_n , the vector to the origin of an arbitrary unit cell and \vec{r}_j the vector to an atom within that particular unit cell (Fig 2.2 b). For a crystal with $n=1..N$ unit cells and $j=1..J$ atoms in each unit cell, the *structure factor of the crystal* can be re-written as

$$F^C(\vec{H}) = \sum_{n=1}^N \sum_{j=1}^J f_j e^{2\pi i \vec{H} \cdot (\vec{r}_n + \vec{r}_j)} \quad 2.7$$

$$F^C(\vec{H}) = \sum_{n=1}^N e^{2\pi i \vec{H} \cdot \vec{r}_n} \sum_{j=1}^J f_j e^{2\pi i \vec{H} \cdot \vec{r}_j} \quad 2.8$$

The first sum in Eqn. 2.8 is the *lattice factor* G , and the second the *structure factor of the molecule* within the unit cell as in Eqn. 2.5.

The lattice vector \vec{r}_n itself is a linear combination of the unit cell (basis) vectors a , b and c . If the crystal has U unit cells along \vec{a} , V unit cells along \vec{b} , and W unit cells along \vec{c} such that $U \cdot V \cdot W = N$, G can be rewritten as

$$G = \sum_{u=0}^{U-1} \sum_{v=0}^{V-1} \sum_{w=0}^{W-1} e^{2\pi i \vec{H} \cdot (u\vec{a} + v\vec{b} + w\vec{c})} \quad 2.9$$

$$G = \sum_{u=0}^{U-1} e^{2\pi i u \vec{H} \cdot \vec{a}} \sum_{v=0}^{V-1} e^{2\pi i v \vec{H} \cdot \vec{b}} \sum_{w=0}^{W-1} e^{2\pi i w \vec{H} \cdot \vec{c}} \quad 2.10$$

For large values of U , V and W (i.e. large number of molecules in a crystal), each of the sums in Eqn. 2.10 converges to zero for all non-integer values of $\vec{H} \cdot \vec{a}$, $\vec{H} \cdot \vec{b}$, and $\vec{H} \cdot \vec{c}$. However, with integer values, the sum is not zero. The conditions,

$$\vec{H} \cdot \vec{a} = h, \quad \vec{H} \cdot \vec{b} = k, \quad \vec{H} \cdot \vec{c} = l, \quad 2.11$$

with h, k and l integers are very important and are called the *Laue conditions*.

2.1.4 Reflection through crystal

In a crystal, there exist a set of planes that pass through the atom centers at regular intervals. These planes are described by the Miller indices, hkl . An hkl plane intercepts the unit cell axes at a/h , b/k and c/l respectively. If d is the distance between two hkl lattice planes, it follows from *Laue conditions*,

$$|\vec{H}| = \frac{1}{d}. \quad 2.12$$

Incident X-rays with a glancing angle θ are reflected from the lattice planes in the crystal with an angle of reflection also equal to θ . The constructive interference would occur only when the path length difference between reflected rays would be an integer multiple wavelengths of the radiation.

2.1.5 Reciprocal Lattice

For any real space crystal lattice, a reciprocal lattice exists such that the *Laue conditions* are automatically satisfied. If a crystal lattice has unit cell vectors \vec{a} , \vec{b} and \vec{c} , the corresponding reciprocal lattice vectors, \vec{a}^* , \vec{b}^* and \vec{c}^* are calculated as

$$\vec{a}^* = \frac{\vec{b} \times \vec{c}}{V}, \quad \vec{b}^* = \frac{\vec{c} \times \vec{a}}{V}, \quad \vec{c}^* = \frac{\vec{a} \times \vec{b}}{V} \quad 2.14$$

where, V is the volume of the unit cell given as $V = \vec{a} \cdot (\vec{b} \times \vec{c})$. The reciprocal lattice consists of a periodic arrangement of reciprocal space basis vectors. A vector \vec{H}_{hkl} drawn from the origin of the reciprocal lattice to any point having coordinates hkl is perpendicular to the set of planes in the real space crystal lattice with Miller indices hkl . The scattering vector, \vec{H} , may now be

expressed as a linear combination of the reciprocal lattice vectors with the Laue integers as the constants,

$$\vec{H}_{hkl} = h\vec{a}^* + k\vec{b}^* + l\vec{c}^* \quad 2.15$$

These are also the solutions to the *Laue equations*. The length of this vector is equal to the reciprocal of the spacing d of the planes with Miller indices hkl (or an integer multiple of them).

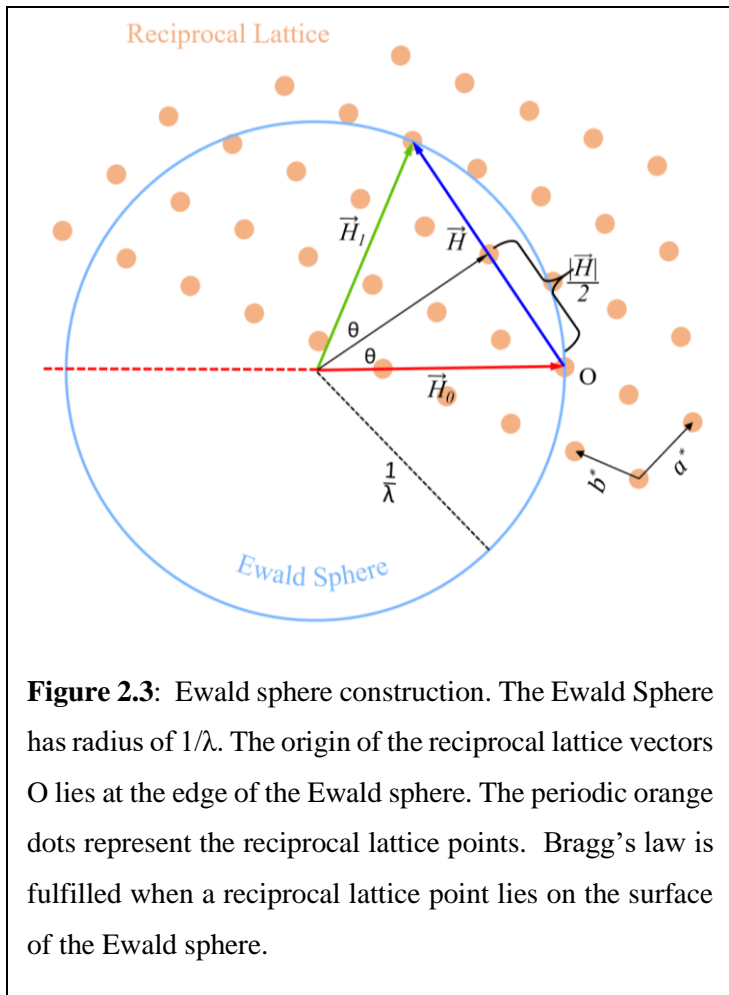
$$|\vec{H}_{hkl}| = \frac{1}{d_{hkl}} \quad 2.16$$

Each reciprocal lattice point is related to a set of planes in the crystal and represents the orientation and the spacing of the corresponding set of planes. The reciprocal lattice is a crystal property as it reflects the periodicity of the real lattice. From the unit cell (in real space) and its orientation with respect to the incident radiation of known wavelength, the reciprocal lattice positions for a given Bragg reflection can be determined. Conversely, it is possible to determine the unit cell parameters and the orientation from the Bragg reflections. A rotation of the crystal will cause similar rotation of the crystal lattice as well as of the reciprocal lattice.

2.1.6 Ewald sphere

X-ray scattering is considered an elastic process. That is, the wavelength of the incident and the diffracted radiation is the same. Consider a graphical representation of reciprocal lattices as shown in Fig. 2.3. Since the incident and scattered wave vectors have equal magnitudes $1/\lambda$, the scattering vector, \vec{H} will cover a sphere in reciprocal space. This sphere is called the Ewald sphere. Let the sphere intersect the origin, O at forward scattering direction.

Consider a reciprocal lattice point lying on the surface of the Ewald sphere. From the Fig. 2.3



$$\sin \theta = \frac{|\vec{H}_{hkl}|}{\frac{2}{\lambda}}$$

Using Eqn. 2.16, we get

$$2d \sin \theta = n \lambda \quad 2.17$$

which is Bragg's law for constructive interference. Bragg's law is satisfied only when the scattering vectors lie on the Ewald sphere.

Fig. 2.3. shows that it is not possible for all the reciprocal lattice points to lie on the Ewald sphere at once. During data collection, the crystal is rotated to

sample complete diffraction data. In serial crystallography, the same effect is obtained by collecting diffraction patterns from many randomly oriented crystals (Kirian et al., 2011).

2.1.7 Structural heterogeneity

Proteins do not form perfect crystals. In a crystal, unit cells are repeated in a regular manner in three dimensions. All the molecules in each unit cell have the same positions as well as the same orientations. However, both static and dynamic disorder are found in protein crystals. Proteins are large and flexible molecules. The conformation of the molecules can be slightly different in each unit cell from their equilibrium position. In addition, the molecules or parts of the molecules may not align in the same position and in the same orientation. These are examples of static disorders.

Molecules might fluctuate between different conformations giving rise to dynamic disorder. All of these disorders contribute to the Debye Waller Factor (*DWF*)

$$DWF = \exp \left[-8 \pi^2 \langle x^2 \rangle \left(\frac{\sin \theta}{\lambda} \right)^2 \right] \quad 2.18$$

where, $\langle x^2 \rangle$ is the mean square displacement of an atom, and $8 \pi^2 \langle x^2 \rangle$ is called the *B-factor*. The *DWF* only reduces the intensity of the Bragg peaks and does not change the shape or the sharpness of the peaks. The atomic scattering factor for an atom with DWF correction is,

$$f = f^o \exp \left[-B \left(\frac{\sin \theta}{\lambda} \right)^2 \right] \quad 2.19$$

where, f^o is the scattering factor for the atom without any displacement.

2.1.8 Mosaicity

Another disorder in protein crystals is the *mosaicity*. During crystallization, all the molecules (and the real space lattice planes) throughout the crystal do not align perfectly. A single crystal consists of multiple domains (mosaic blocks) which are oriented slightly different from each other. The effect of *mosaicity* is an angular broadening of the reciprocal lattice points spanning a small angular range, χ . Consequently, when such a broad point intersects with the Ewald sphere, the intensity of only a part of the reflection is collected. When the crystal is rotated during data collection, the subsequent diffraction images will record the remainder of the reflection. However, the intensity integrated over the entire reflection range is required. Crystallographic software packages are capable of integrating the full reflection intensities across multiple diffraction images. In serial crystallography where crystal rotation is not possible, this issue is

solved by averaging a large number of observations for the same Bragg reflection (see section 2.3.2) with the crystals in slightly different orientations.

2.1.8 The phase problem

The inverse Fourier transform of the structure factor of the molecule, F^M , yields the electron density of the molecule.

$$\rho(\vec{r}) = \int F^M(\vec{H}) e^{-2\pi i \vec{H} \cdot \vec{r}} dH \quad 2.20$$

Since $F(\vec{H})$ is nonzero only at the lattice points, the integral may be written as a discrete sum:

$$\rho(xyz) = \frac{1}{V} \sum_{hkl} F_{hkl}^M e^{-2\pi i (hx+ky+lz)} \quad 2.21$$

Since F_{hkl}^M is a complex quantity, $F_{hkl}^M = |F_{hkl}^M| e^{i \varphi_{hkl}}$

$$\rho(xyz) = \frac{1}{V} \sum_{hkl} |F_{hkl}^M| e^{-2\pi i (hx+ky+lz - \varphi_{hkl})} \quad 2.22$$

The diffracted intensity is proportional to the square of the *structure factor amplitude*. X-ray detectors measure the intensities of the diffracted beams. Although the *structure factor amplitudes* may be measured directly, all information about the phase is lost. However, the phases must be known to reconstruct the electron density. This leads to the *phase problem* in crystallography (Taylor, 2003).

Various techniques exist to retrieve the phase of the diffracted waves (Millane, 1990). One such approach is Molecular Replacement (MR) (Rossmann, 1990). The structure of a homologous protein is used to determine the unknown orientations and positions of the protein molecules in the crystal. Phases are calculated from the oriented model and combined with the measured

amplitudes to calculate new electron density maps to solve the unknown structure of the protein of interest. All phases of the structures presented in this dissertation are determined using the MR method.

2.2 Theory of transmission electron microscopy

2.2.1 Electron generation

Electron microscopes use a beam of electrons as a source of illumination. According to de Broglie's idea of wave-particle duality, the particle momentum p is related to its wavelength λ through Planck's constant h .

$$\lambda = \frac{h}{p} \quad 2.23$$

Electrons are produced by a cathode that may be a heated tungsten filament or a field emission gun. The electrons are made to accelerate by passing them through high voltage, V . The energy thus gained by the electron is equal to the kinetic energy of the electron.

$$eV = \frac{m_0 u^2}{2} \quad 2.24$$

Where e is the electronic charge of an electron, m_0 the mass of the electron and u the velocity acquired by the electron. Equating $p = m_0 u$ and adding the relativistic correction, the Eqn. 2.24 becomes

$$\lambda = \frac{h}{\sqrt{2m_0 eV \left(1 + \frac{eV}{2m_0 e^2}\right)}} \quad 2.25$$

A decrease in electron wavelength is accomplished by increasing the accelerating voltage. For example, the wavelength is 0.054 Å at 50 keV and 0.037 Å at 100 keV. Typically, an accelerating

voltage of 300 kV which is much higher than what is required to generate electrons with wavelength of $\sim 1 \text{ \AA}$. Higher accelerating voltage has been shown to be optimal for imaging thicker biological specimens due to reduced inelastic scattering (Herzik et al., 2017).

The electrons are guided by magnetic lenses that are analogous to glass lenses in optical microscopy. A schematic of a typical magnetic lens is shown in Fig. 2.4. The focusing effect is the Lorentz force as a result of the interactions between the magnetic field of the lenses and the moving electrons. The focal length can be varied by varying the current in the coil used to generate the magnetic field.

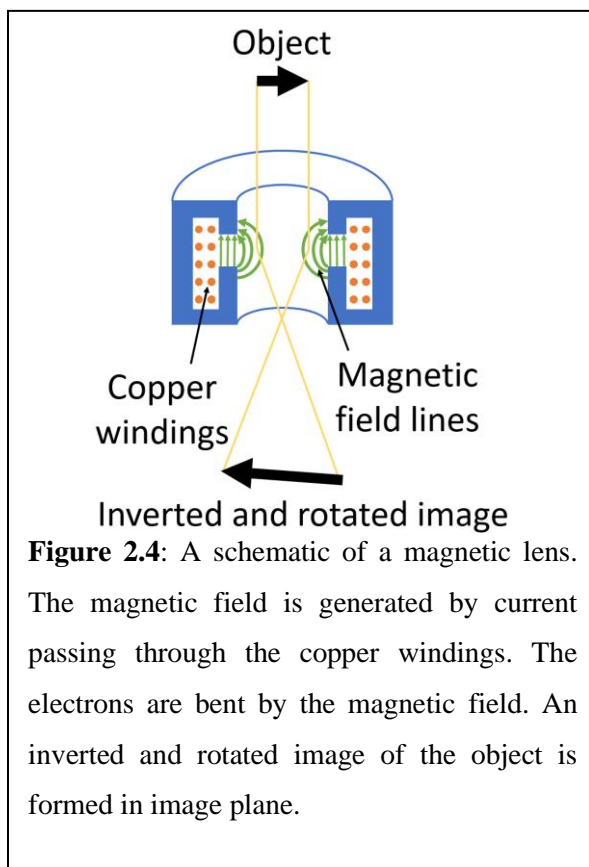


Figure 2.4: A schematic of a magnetic lens. The magnetic field is generated by current passing through the copper windings. The electrons are bent by the magnetic field. An inverted and rotated image of the object is formed in image plane.

2.2.2 Image formation

Electron microscopes can generate image both in scanning mode and transmission mode. Scanning electron microscope creates an image by detecting reflected or knocked-off electrons, while transmission electron microscope (TEM) uses transmitted electrons passing through the sample to create an image. The formation of an image in the electron microscope originates from the interaction of the electrons with the object. The negatively charged electrons interact with both the electrons and nuclei of the atoms via Coulomb forces. Thus, the electron wave resolves the ‘electrostatic potential’ of the object.

The electrons can interact with the object in different ways. They can pass through the sample as a transparent medium, scatter elastically or scatter inelastically (transfer part of their energy to the sample). With inelastic interaction, the amount of energy transferred from electron to sample is variable and random. When these electrons reach the imaging plane, they have unknown energy and angle of incidence. This generates noise in the image. Elastically scattered electrons however, maintain their energy. The strength of the scattering depends on the electric potential of the atom and the number of atoms in a molecule. Atoms with high atomic number possess more electrons around their nucleus, and thus more incident electrons will be scattered. Contrast in the image arises when there is interference between electrons coming in from different angles. If the thickness is homogeneous, areas in which heavy atoms are concentrated appear with darker contrast than such with light atoms (mass contrast). Similarly, more electrons are scattered in thick areas than in thin areas; thus, thick areas appear dark (thickness contrast).

In TEM, the electrons pass through the sample before reaching the detector. They contain the information on the structures of the sample. The images produced by TEM are not ‘shadows’ but rather a 2D projection of the object’s electron potential.

The relationship between the image contrast $I(x)$ and the object projection $O(x)$ can be written as the convolution:

$$I(x) = O(x) \otimes P(x) \quad 2.26$$

where $P(x)$ is the point spread function (PSF). The PSF determines how well a point in the object plane is imaged in the image plane. The PSF is determined mostly by the microscope aberrations (Shaw & Rawlins, 1991). The Fourier transform of the image contrast can be written as

$$I(k) = O(k)CTF(k) \quad 2.27$$

where $O(k)$ is the Fourier transform of the object projection and $CTF(k)$ is the Fourier transform of the PSF called the *Contrast Transfer Function* (CTF). The CTF mathematically describes how much contrast is present in a single micrograph and is dependent on both the microscope and the imaging conditions. The CTF is modeled as (Bendory et al., 2020):

$$CTF(k, \lambda, \Delta f, C_s) = -\sin\left(\pi\lambda |k|^2 \Delta f - \frac{\pi\lambda^3 |k|^4 C_s}{2} + \alpha\right) \cdot E(|k|) \quad 2.28$$

where λ is the electron wavelength, k is the wave number, Δf is the objective defocus, C_s is the spherical aberration, α is a phase shift factor and $E(|k|) = e^{-Bk^2}$ is an exponentially decaying envelope function (Bendory et al., 2020). The parameters λ and C_s are the function of the microscope. The Δf and α describe the imaging conditions. $E(|k|)$ is specified by a parameter called *B-factor* (Rohou & Grigorieff, 2015). Although B has the same form as the *B-factor* used in crystallography, it does not have the same significance. Instead, it is introduced due to the beam energy spread, the beam coherence, and the sample drift. The defocus value of the objective lens also has a pivotal role. High defocus value increases the period of the sine function. Although this increases the contrast, the rapid oscillation of the CTF causes a loss of signal and reduces the achievable resolution. On the other hand, at low defocus, there might not be enough contrast to distinguish the particle from the background noise (Bendory et al., 2020). An optimum value of defocus range needs to be determined during imaging.

2.3 Sample preparation

Here, the fundamental principle of sample preparation is explained briefly. A detailed description of these methods is beyond the scope of this dissertation and will not be discussed. The

exact protocols for sample preparation are presented for each protein under investigation in their respective chapters.

2.3.1 Protein overexpression

A large quantity of pure protein is required to make protein crystals. While some protein may naturally occur in large quantities and can easily purified from their host organism, most proteins either occur in small quantities or occur in organisms from which they cannot be easily purified. Protein overexpression protocols generate large quantities of desired protein. Fast replicating organisms like bacteria or yeast are genetically modified to carry a gene that codes for a desired protein (Demain & Vaishnav, 2009). The gene is carefully engineered such that the organism does not make the protein unless specifically induced to do so (Makrides, 1996; Stevens, 2000). The protein expressed in this way is called a recombinant protein (Baneyx, 1999). Usually, the bacteria are grown in large cultures and harvested for protein purification.

2.3.2 Protein purification

Protein purification requires a series of steps carried out to isolate the protein of interest from bacterial cells. The harvested cells undergo a lysis procedure which breaks the cell membrane. The lysate slurry contains, along with the protein of interest, all other kinds of proteins, nucleic acids, and other cell debris. The insoluble contaminants are immediately removed usually by high-speed centrifugation. The remaining solution is passed through a column packed with a material to which the recombinant protein binds. The other soluble proteins and nucleic acids will flow through. The recombinant protein adsorbed to the column material is eluted. The elution step introduces chemicals that could be detrimental to the protein's stability. The protein is transferred into a stabilizing solution through buffer exchange. This can be achieved either by dialysis or by

concentration and subsequent addition of stabilizing solution. Furthermore, there are strategies to separate the protein mixture based on size, charge, binding affinity, hydrophobicity, etc. This pure protein can be used immediately or stored in -80°C for extended period of time.

The purified protein is already suitable to be used in cryo-EM experiments. For crystallographic studies, the protein needs to be crystallized.

2.3.3 Protein crystallization

Crystallization is carried out by exposing highly purified protein to an aqueous precipitating agent. The precipitation agent weakens the hydration shell of the protein thereby allowing interactions between protein molecules (McPherson & Gavira, 2014). When the protein reaches the supersaturated state, it crystallizes. The solution in which the crystals are stable is also referred to as mother liquor. The formation of crystals depends on various factors such as pH, temperature, chemical additives, concentration, etc. Conformational heterogeneity may also hinder successful crystallization. So stable, and homogenous protein solutions are required. Determining the optimum crystallization condition is still a trial-and-error method (Rupp & Wang, 2004). Fortunately, high-throughput robotic methods exist to accelerate and streamline the large number of experiments required to explore the various conditions (Skarina et al., 2014).

2.4 Crystallography data collection

In section 2.4, the fundamentals of data collection with monochromatic X-rays, and general strategy for data processing are explained. Protein specific information is presented in their respective chapters.

There are two major ways of performing crystallography with monochromatic X-rays- the single crystal method and the serial method.

2.4.1 The rotation method

The single crystal method - also referred to as *rotating crystal* method - is mostly employed at synchrotron and lab X-ray sources (Giacovazzo, 1992). A single macroscopic crystal is isolated from the crystallization tray and cryo-cooled by dipping it immediately into liquid nitrogen. The X-ray interaction region also has a stream of cryo-cooled air to keep the crystal frozen (typically at 100 K) during data

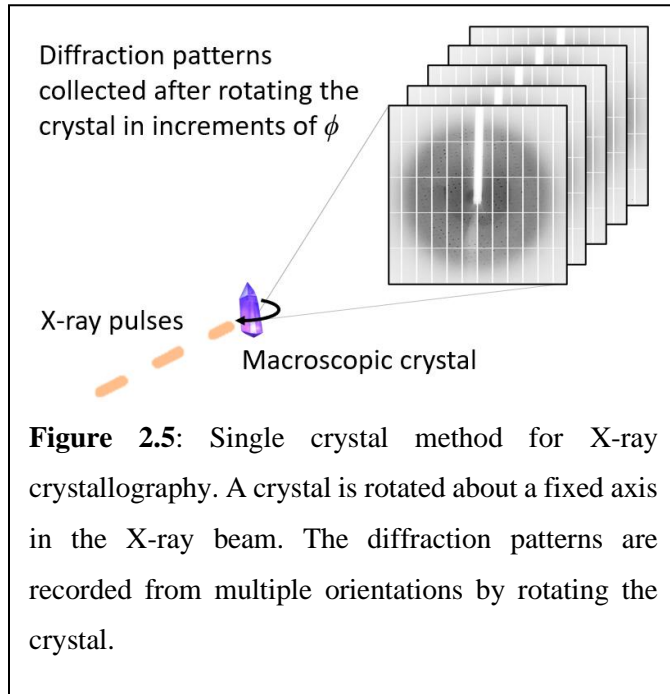


Figure 2.5: Single crystal method for X-ray crystallography. A crystal is rotated about a fixed axis in the X-ray beam. The diffraction patterns are recorded from multiple orientations by rotating the crystal.

collection. The crystal is aligned to the X-ray beam and is rotated in increments of ϕ (typically $0.1^\circ - 0.3^\circ$) during the X-ray exposure (Fig. 2.5). The rotation brings different atomic planes into position so that the intensities of Bragg reflections can be recorded. The diffraction pattern is recorded on the detector until the reciprocal space has been completely sampled. The total angular rotation depends on the symmetry of the crystal. The lower the symmetry, the larger the angular range necessary to sufficiently sample the reciprocal space.

2.4.2 Processing of data from the single crystal rotation method

Once a complete monochromatic dataset has been recorded, it is processed by specialized crystallographic software. Most popular are *iMosflm* (Battye et al., 2011) and *HKL3000* (Minor et al., 2006). Spot search is performed to determine the location of potential Bragg peaks. Based on the pattern of the spots, the initial orientation, space group and the dimension of the unit cell is determined. The spots are then indexed by assigning Miller Indices hkl to each of them. All the

diffraction images are related to previous ones by a rotation of the angle ϕ . Manual indexing of every diffraction image is not necessary. Although one image is mostly sufficient for determining an initial crystal orientation, a few images can also be used for accurate indexing. The *mosaicity* is also estimated during indexing which is further refined as the program proceeds through the integration of reflection intensities. Finally, the reflection intensities for each (hkl) are integrated and written into a single file.

Various tests are performed to assess the quality of the data like R_{merge} , *completeness*, *multiplicity*, etc. R_{merge} measures the spread of n independent measurements of the intensity of a reflection, $I_i(hkl)$, around their average, $\bar{I}(hkl)$ as:

$$R_{merge} = \sum_{hkl} \sum_{i=1}^n \frac{|I_i(hkl) - \bar{I}(hkl)|}{I_i(hkl)} \quad 2.29$$

The data is considered good when the R_{merge} is $< 10\%$. The *completeness* and *multiplicity* describe the amount of reciprocal space that has been sampled by the data and the average number of identical (or symmetry equivalent) reflections that have been observed, respectively. The *completeness* for a high-quality data is $> 95\%$ with a *multiplicity* > 3 . If the quality is not good enough, more data is collected from a new sample until the quality requirements are met.

2.4.3 Serial crystallography

Serial crystallography (SX) was originally developed for XFEL sources (Chapman et al., 2011). The high intensity XFEL beam destroys the single crystal upon a single exposure. Due to the ultrashort pulses of XFEL, the diffraction outruns the radiation damage (Hwu & Margaritondo, 2021). A damage free DP is recorded before the crystal disintegrates. The X-rays produced by the XFEL are quasi-monochromatic. Still-exposures with this type of radiation will yield partial

reflections. Rotation of the crystal is not feasible during the fs pulse duration. Thus, one diffraction pattern collected from one orientation is not sufficient to determine the structure. The complete

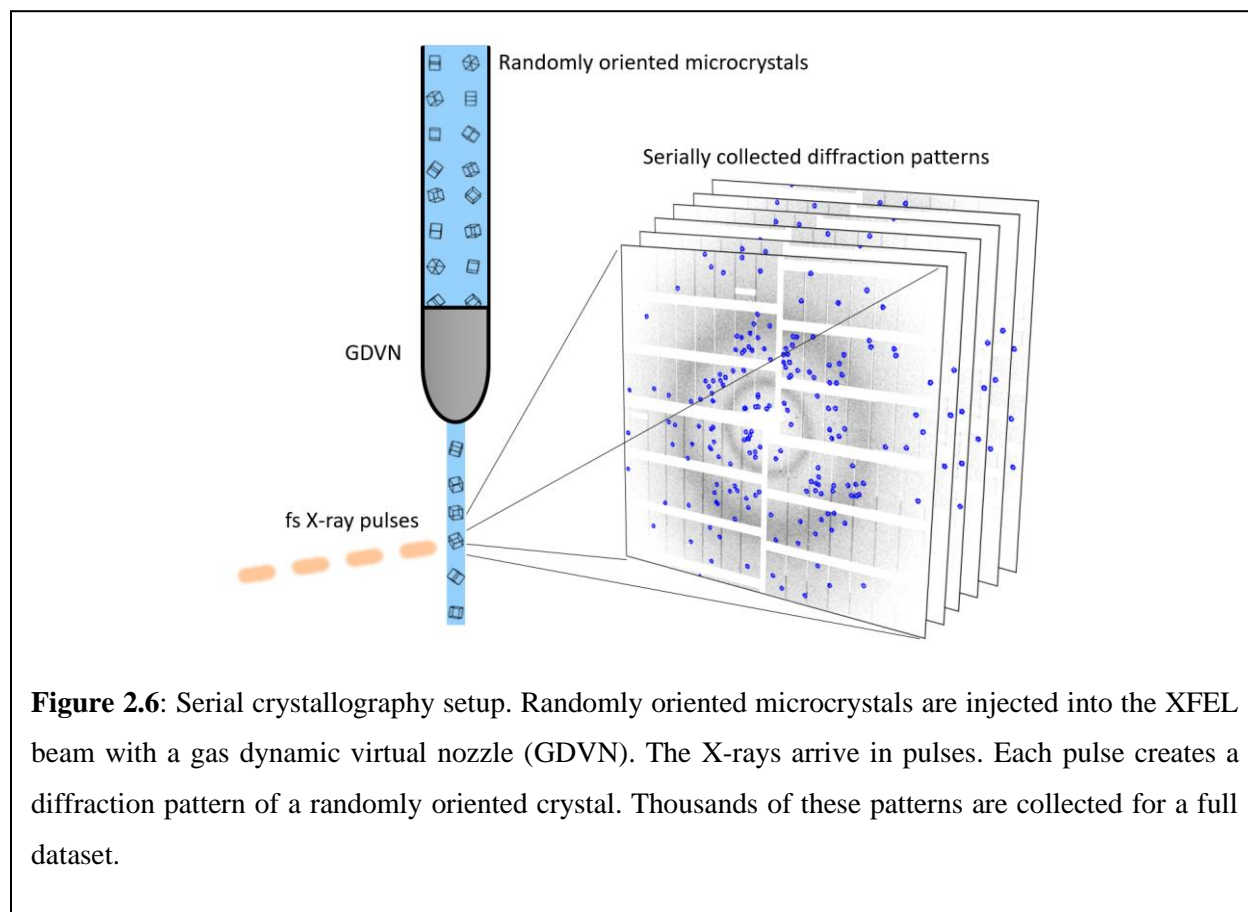
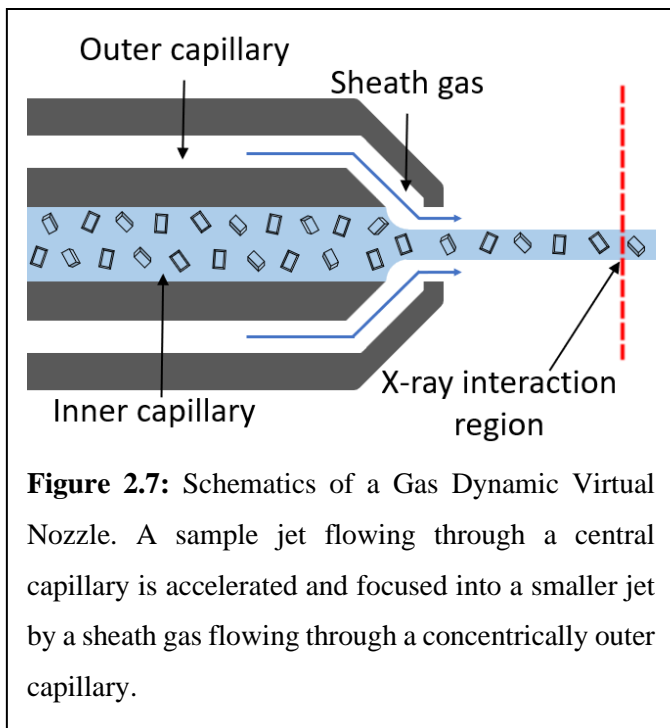


Figure 2.6: Serial crystallography setup. Randomly oriented microcrystals are injected into the XFEL beam with a gas dynamic virtual nozzle (GDVN). The X-rays arrive in pulses. Each pulse creates a diffraction pattern of a randomly oriented crystal. Thousands of these patterns are collected for a full dataset.

diffraction dataset needs to be collected from many crystals. The damaged crystal is discarded and immediately replenished by a new one in a *serial* fashion (Fig. 2.6). Each crystal contributes to a single diffraction image. Intensities from a large number of diffraction image are combined to a complete data set. The integrated intensity can be reconstructed from averaging many observations of partial reflections in slightly different, random orientations via Monte Carlo integration (Kirian et al., 2011). All of the reciprocal space is eventually sampled.

Different methods were developed to transport the microcrystals serially into the X-ray interaction region, which is sometimes placed inside the vacuum. One of the first design to emerge is the Gas

Dynamic Virtual Nozzle (GDVN(DePonte et al., 2008). Most newer versions are variations of the original GDVN. A typical GDVN consists of two concentric capillaries (Fig. 2.7). The crystalline sample flows through the central capillary and sheath gas, typically helium, is fed into the outer capillary. The pressure induced by surrounding gas stream accelerates the sample flowing out of the inner capillary



into a smaller liquid jet. The diameter of the emerging jet is much smaller than that of original *Rayleigh* jet from the inner capillary. The focusing effect is created by the geometry of the converging gas aperture. The jets are on the scale of a few microns with velocities on the order of 10-100 m/s. GDVN jets are stable in ambient pressure as well as in vacuum. Aside from GDVN which injects the sample in the liquid phase, the microcrystals can also be injected in viscous media (Weierstall, 2014). They can also be applied to tape drives that moves individual droplets containing crystals into the X-ray beam like a conveyor belt (Roessler et al., 2016) or deposited on fixed targets that are rapidly scanned through the X-ray beam (Hunter et al., 2014).

Serial femtosecond crystallography (SFX) refers to serial crystallography experiments performed with the femtosecond long pulses of the XFEL beam. SX has now been adapted to work in synchrotron sources. The method is termed *serial synchrotron crystallography* (SSX).

2.4.4 Data processing for serial crystallography

Since the crystals are randomly located in the jet but the X-rays arrive in well-defined order, not every X-ray pulse hits the crystal. Diffraction patterns without Bragg reflections take a significant amount of storage space. These empty frames must be identified and discarded. This is done by so called hit-finding programs. One such software package is *Cheetah* (Barty et al., 2014). *Cheetah* identifies diffraction patterns containing potential Bragg reflection and saves them. In addition, it has a convenient, built-in masking tool that allows masking of unwanted detector pixels. Currently, there are only three software that process SFX data: *CrystFEL* (White et al., 2012), *cctbx.xfel* (Sauter et al., 2013), and *nXDS* (Kabsch, 2014). All the data presented in this dissertation are processed with *CrystFEL*. *CrystFEL* includes a suite of programs which are briefly described below. More information can be found on the official website at (<https://www.desy.de/~twhite/crystfel>). The program *Indexamajig* performs spot finding, indexing and integration of reflection intensities. It requires an additional input called the *geometry file* which contains information such as the detector distance, the pixel size and the position and orientation of each detector tile (Fig. 2.8). *Indexamajig* is iteratively used with *geoptimiser* which is designed to refine and optimize the detector geometry (Yefanov et al., 2015)). In some cases, an indexing ambiguity may occur in crystals with higher symmetry. The unit cell parameters may be the same, but the molecular orientations will be different along different unit cell directions. If the lengths of the two axes a and b are same, they may be indexed either as (hkl) or as (khl) , yet the intensities $I(hkl)$ and $I(khl)$ will not be identical. In such cases, the program *ambigator* is used to resolve the indexing ambiguity. The final merging of the intensities of same reflections from multiple observations is performed by *partialator*. The programs *compare_hkl* and *check_hkl* are tools for assessing the data quality with different metrics.

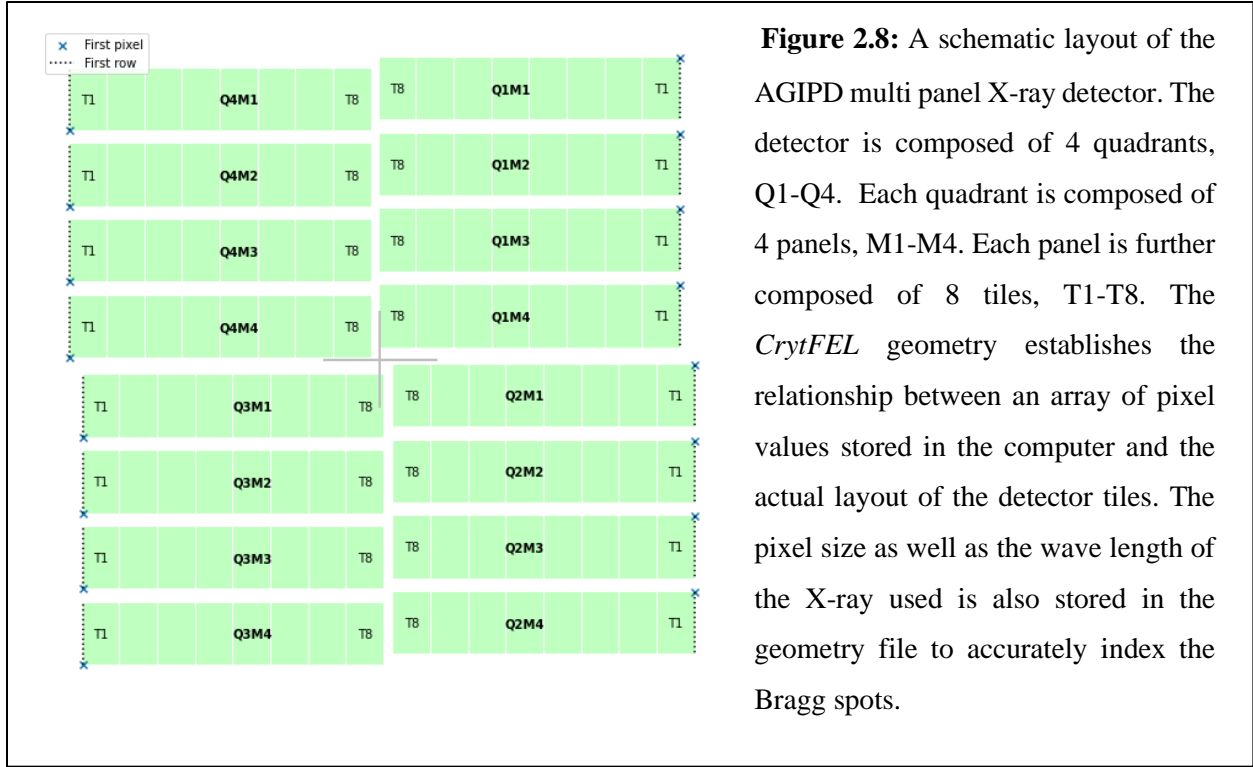


Figure 2.8: A schematic layout of the AGIPD multi panel X-ray detector. The detector is composed of 4 quadrants, Q1-Q4. Each quadrant is composed of 4 panels, M1-M4. Each panel is further composed of 8 tiles, T1-T8. The *CrytFEL* geometry establishes the relationship between an array of pixel values stored in the computer and the actual layout of the detector tiles. The pixel size as well as the wave length of the X-ray used is also stored in the geometry file to accurately index the Bragg spots.

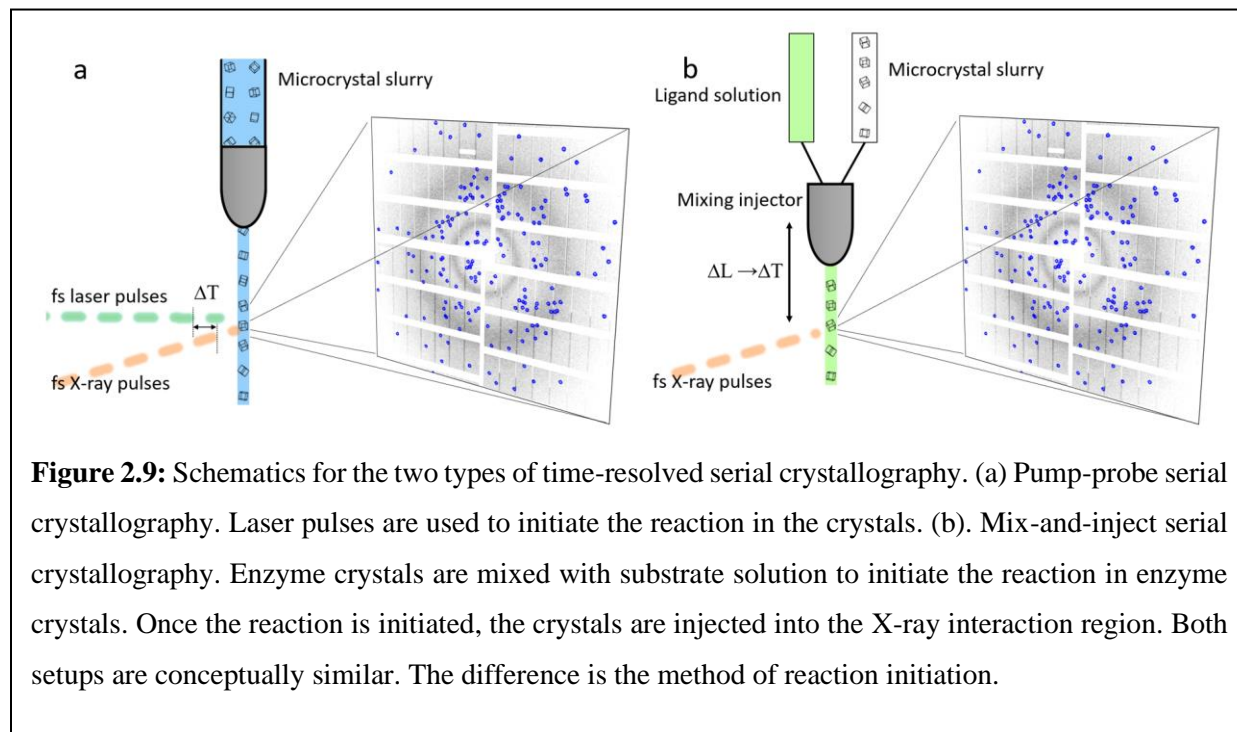
The R_{merge} that assesses data quality for the single crystal method is not suitable for serial data. Instead, a new metric R_{split} is defined as:

$$R_{split} = \frac{2 \sum |I_{even} - I_{odd}|}{\sqrt{2} \sum |I_{even} + I_{odd}|} \quad 2.30$$

where I_{even} represents the intensity of a reflection produced by merging even-numbered patterns, I_{odd} represents the intensity of the equivalent reflection from the odd numbered patterns and the sum is over all reflections. The *completeness* and *multiplicity* are evaluated in an identical way as single crystal data. Another meaningful variable is the Pearson correlation coefficient $CC_{1/2}$ that accounts for the correlation between intensities determined from half the data, each. It is calculated as:

$$CC_{1/2} = \frac{\sum |I_{even} - \langle I_{even} \rangle| |I_{odd} - \langle I_{odd} \rangle|}{\sqrt{\sum (I_{even} - \langle I_{even} \rangle)^2 \sum (I_{odd} - \langle I_{odd} \rangle)^2}} \quad 2.31$$

where the $\langle \rangle$ denotes an average. By evaluating the the $CC_{1/2}$ in resolution shells, they can be used to estimate the resolution limit of the SFX data. Typically, a $CC_{1/2}$ of $1/e = 0.37$ is used.



2.5 Time-Resolved Serial Femtosecond Crystallography (TR-SFX)

Two different methods were used to perform TR-SFX studies presented in this dissertation. They are the pump-probe method and the mix-and-inject method (Schmidt, 2013). They are explained below.

2.5.1 Pump-Probe TR-SFX

Pump-probe time-resolved crystallographic experiment are setup in the same as a serial crystallographic experiment except that pulses from an additional laser of appropriate wavelength are employed to start a reaction (Tenboer et al., 2014). The laser pulse arrival times are synchronized to the arrival times of the X-ray pulses from the XFEL (Fig. 2.9 a). As the

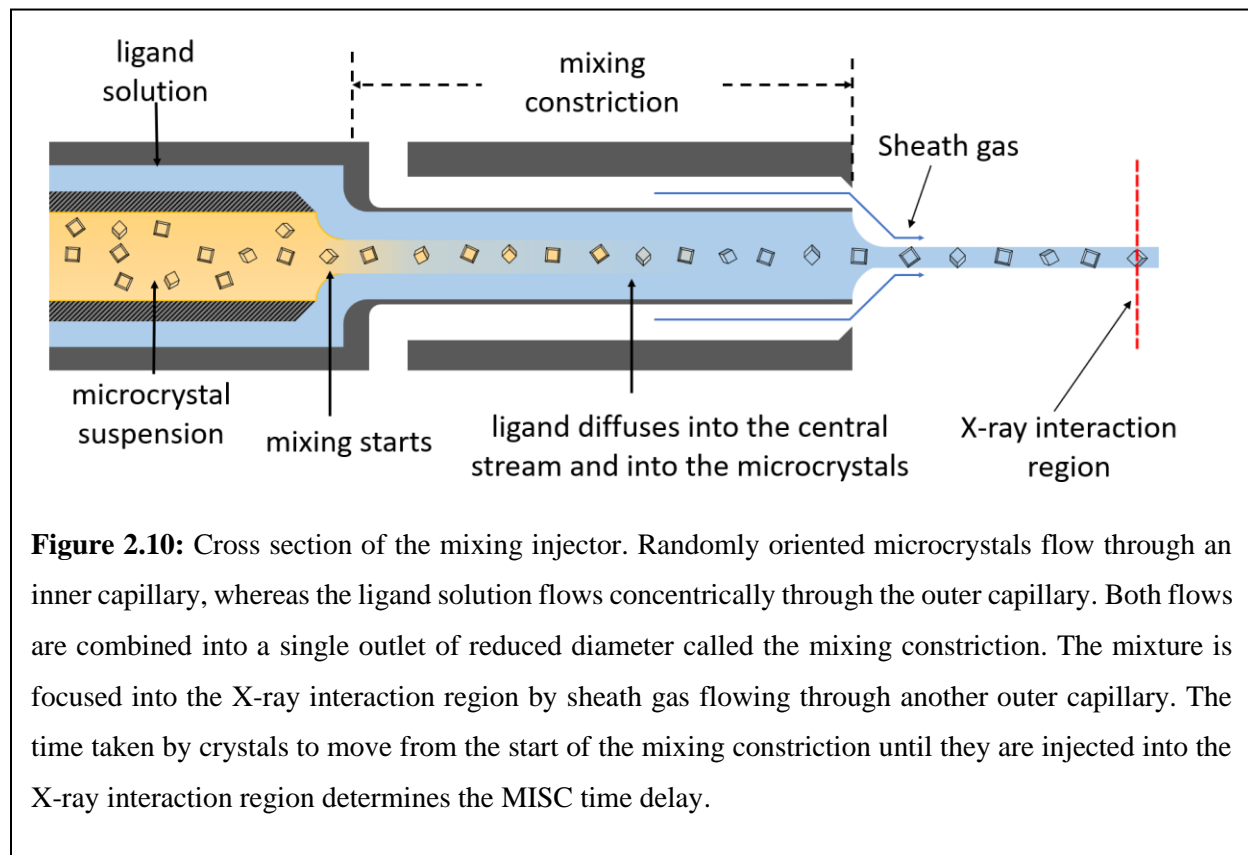
microcrystals travel down the jet, a section of the jet is illuminated by a brief laser flash, called the ‘pump’ pulse. After an adjustable time-delay Δt , the same section is exposed to an X-ray pulse, called the ‘probe’ pulse, which generates the diffraction pattern. At least one dataset is collected without laser illumination which provides a reference data set. Datasets with various pump-probe time delays are collected as required. The processes that occur on ultrafast time scales can be investigated by the use of femtosecond XFEL pulses in conjunction with femtosecond pump lasers (Barends et al., 2015; Pande et al., 2016)).

The pump-probe method works with proteins which are photoactive in nature. However, only 0.5% of all proteins are photo-reactive (Monteiro et al., 2021). Most biologically relevant proteins like enzymes are not photoactive and require alternative method of activation. Efforts have been made where the enzymatic reaction was triggered using caged substrates (Bourgeois & Weik, 2008; Givens et al., 2005). The target molecules are rendered biologically inert (or caged) by chemical modification with a photoremovable group. Upon photoexcitation, the caged compound is released which can then react with the enzyme. While this method has great potential (Mehrabi et al., 2019; Monteiro et al., 2021; Tosha et al., 2017), the complexity required to engineer such compounds may limit the widespread adoption. Here, another technique is outlined that does not required caged compounds to study enzymatic reaction in time-resolved fashion.

2.5.2 Mix-and-Inject Serial Crystallography (MISC)

In mix-and-inject serial crystallography (MISC), enzyme microcrystals are mixed with substrate (Schmidt, 2013). The reaction is initiated by diffusion of substrate towards the active site of every enzyme molecule in the crystal. Once the crystals are small enough, diffusion times can be faster than the duration of the enzymatic turnover. The mixture is injected in the X-ray

interaction region. The time-delay is the time required by the crystals to travel from the mixing region in the injector to the X-ray interaction region (Fig. 2.9 b).



Special injectors are required to achieve simultaneous mixing and serial injection of the crystals (Calvey et al., 2016, 2019). A schematic setup is shown in Fig. 2.10. The mixing region has two concentric capillaries. Enzyme crystals are flown through the inner capillary whereas the ligand solution flows through the outer capillary. Both flows are combined into a single outlet of reduced diameter called the mixing constriction. The end of mixing constriction is essential a GDVN where another concentric capillary with helium gas focuses the jet into the X-ray beam. The time delay is controlled by the geometry of the injector as well as the flow rates of the sample and the ligand.

2.5.2.1 Diffusion of substrate inside crystals

Diffusion of substrate molecules into protein crystals is governed by Fick's laws of diffusion. Particularly, Fick's second law predicts how diffusion changes the concentration of ligand in a crystal with respect to time:

$$\frac{\partial C}{\partial t} = D \nabla^2 C \quad 2.32$$

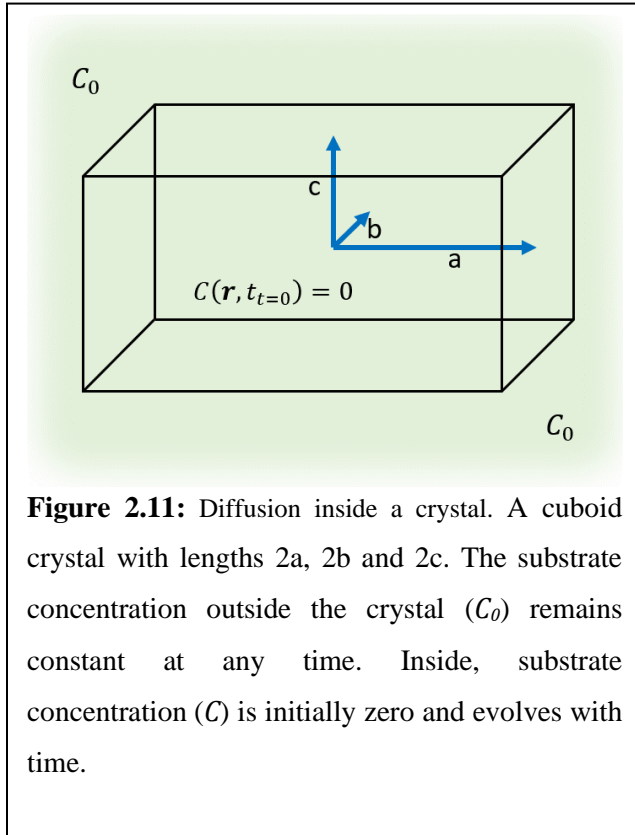


Figure 2.11: Diffusion inside a crystal. A cuboid crystal with lengths $2a$, $2b$ and $2c$. The substrate concentration outside the crystal (C_0) remains constant at any time. Inside, substrate concentration (C) is initially zero and evolves with time.

where $C = C(\mathbf{r}, t)$ is the concentration of substrate that depends both on time and position. D is the diffusion coefficient, and ∇^2 is the Laplacian operator which generalizes the second derivative in 3D space.

Eqn. 2.32 is a second order partial differential equation that can be solved by separation of variables. With appropriate boundary conditions, an analytic solution of Eqn. 2.32 can be found (Carslaw & Jaeger, 1959). A solution exists for cuboid shaped crystal with half edge lengths a , b , and c as shown in Fig.

2.11. The solution can be further simplified by assuming the following: (i) The substrate concentration outside the crystal (C_0) remains constant throughout, (ii) binding of substrate to the enzyme is neglected, so that the substrate diffuses freely into the crystal, and (iii) mixing of crystal with substrate is instantaneous at time $t = 0$, i.e. initially the concentration of the substrate, (C_0), inside the crystal is zero, and outside it is C_0 (Schmidt, 2013, 2020). With these boundary conditions, the solution of Eqn. 2.32 is given by:

$$\begin{aligned}
C(x, y, z, t) = & C_0 \left[1 - \frac{64}{\pi^3} \sum_{l=0}^{\infty} \sum_{m=0}^{\infty} \sum_{n=0}^{\infty} \frac{(-1)^{l+m+n}}{(2l+1)(2m+1)(2n+1)} \right. \\
& \times \cos \frac{(2l+1)\pi x}{2a} \cos \frac{(2m+1)\pi y}{2b} \cos \frac{(2n+1)\pi z}{2c} \\
& \left. \times \exp \left(-\frac{D\pi^2}{4} \left[\frac{(2l+1)^2}{a^2} + \frac{(2m+1)^2}{b^2} + \frac{(2n+1)^2}{c^2} \right] \cdot t \right) \right] \quad 2.33
\end{aligned}$$

where l , m , and n are integers. The concentration of substrate inside the crystal thus depends on the initial outside concentration C_0 , the position within the crystal, and a time dependent exponential term. The exponential term contains a characteristic time, τ_c in the form:

$$\tau_c = \frac{4}{D\pi^2 \left[\frac{(2l+1)^2}{a^2} + \frac{(2m+1)^2}{b^2} + \frac{(2n+1)^2}{c^2} \right]} \quad 2.34$$

τ_c , also defined as the diffusion time, is the time required by the diffusing substrate to reach 63% ($1 - 1/e$) of the concentration of the enzyme molecules in the crystal (Schmidt, 2013). For homogenous activation the ligand has to reach every unit cell inside the crystal relatively uniformly. This means, the diffusion time must be short. One ligand per enzyme active site is required for optimum reaction initiation (Schmidt, 2020). This 1:1 ratio of catalytic clefts to substrate is called a stoichiometric concentration (StC). From Eqn. 2.33, it is evident that such requirement can be met by having small crystal size, large diffusion coefficient and large concentration of ligand outside the crystal. With large outside ligand concentration, the stoichiometric concentration is reached much faster than the diffusion time (Schmidt, 2020). The size of crystal can be controlled during crystallization. The diffusion coefficient is large if the ligand is soluble in crystal mother liquor and there exist large solvent channels inside the crystal. And in an actual experiment, the

ligand can be supplied at large flow rate compared to that of crystals to maintain a large concentration difference inside and outside the crystal.

2.6 Crystallographic data analysis

2.6.1 Electron density maps and structure determination

The processing of data from both the rotation method and from the serial crystallography results in a list of reflection indices and their corresponding integrated intensities. Further processing can be done by existing software packages such as those available from the *Collaborative Computational Project Number 4 (CCP4)* suite of programs (Winn et al., 2011). From the reflection intensities structure factors amplitudes can be calculated essentially by taking the square root (French & Wilson, 1978). The unknown phases are determined by molecular replacement method. In practice, it is performed by the program *Phaser* (McCoy et al., 2007) which takes structure factor amplitudes and a homologous model as its inputs. Using a rotation function to determine the orientation of the model, and a translation function to determine its absolute position in the unit cell, *Phaser* calculates the phases and generates an electron density map along with an initial model. This model of the protein at this stage is not accurate. To determine a structural model that best represents the observed data, structural refinement is performed. Popular programs for refinement are *Refmac* (Murshudov et al., 2011) and *Phenix* (Liebschner et al., 2019). The structure is adjusted so that the amplitudes calculated from it fit the observed amplitudes as close as possible. Geometric restraints are used during the refinement to increase the observable to free parameter ratio (Urzhumtsev & Lunin, 2019).

The quality of the refined model is assessed by quality factors such as $R_{crystal}$ and R_{free} . $R_{crystal}$ is a measure of agreement between the amplitudes of the structure factors amplitudes calculated from a crystallographic model and those from the X-ray diffraction data. It is calculated as

$$R_{crystal} = \frac{\sum_h ||F_h| - |F_{calc}||}{\sum_h |F_h|} \quad 2.34$$

where $|F_h|$ are the observed structure factor amplitudes, and $|F_{calc}|$ are structure factor amplitudes calculated from the refined model. 5% of the reflections are selected randomly to calculate an R_{free} in the same way as the $R_{crystal}$. The R_{free} determines how well the structural model predicts the 5% that were not used in refinement. The refinement is performed until both the R-factors converge. For a well refined model, both R-factors are typically on the order of 20 % or less.

2.6.2 Difference electron density maps

In time-resolved experiments, the difference in electron density between the activated and non-activated state are analyzed to determine both the structures of the intermediates and the chemical, kinetic mechanism of the reaction. To obtain a difference electron density (DED) map, structure factor amplitudes for both the *dark* or reference data (without activation), $|F_{obs}^{dark}|$, and the *light* data (with activation), $|F_{obs}^{light}|$, are required. A structural model is refined against $|F_{obs}^{dark}|$, so that calculated structure factor amplitudes for dark state $|F_{calc}^{dark}|$, and the phases ϕ^{dark} can be obtained. The $|F_{obs}^{dark}|$ is scaled to the $|F_{calc}^{dark}|$, to bring the reference data to an absolute scale.

Once scaled, the difference structure factor amplitudes are calculated as

$$\Delta|F| = |F_{obs}^{light}| - |F_{obs}^{dark}| \quad 2.35$$

Usually a *weighting factor* w , is also applied to $\Delta|F|$, to reduce the effect of outliers (Ren et al., 2001a) which could be (i) too large an experimental error, and (ii) too large a difference that would otherwise dominate the difference map.

The time dependent difference electron density, $\Delta\rho(t)$, is calculated as

$$\Delta\rho(xyz, t) = \frac{1}{V} \sum_{hkl} w \Delta|F| e^{-2\pi i (hx+ky+lz - \varphi^{dark})} \quad 2.36$$

These DED maps contain both positive and negative features. Positive features appear in regions where electron densities are measured but are absent in the reference used. Conversely, negative features appear in regions where electron densities are not observed but are present in the reference.

2.6.3 Omit difference map

DED maps can only be calculated from isomorphous datasets. In isomorphous datasets, the unit cell parameters remain essentially unchanged. However, in some cases the unit cell parameters and even the space group of the crystal can change (Stagno et al., 2017). This is more common in MISC experiments because a bulky ligand is added that might induce large structural changes. In such case, an omit difference map (DED_{omit}) is calculated.

The atoms of interest are removed from the reference model before refinement. These atoms could be water molecules, ligand molecules or even a number of amino acid residues. With omit difference structure factors, $\Delta|F^{omit}| = |F_{obs}| - |F_{calc}|$, an omit difference electron density map is calculated. If the presence of atoms or ligands are supported by the observed data, an omit difference map will show a strong positive signal in the region where the atoms have been removed. This concept can be extended to a ligand bound dataset refined against a model without ligand. A positive signal will appear in the place where the ligand binds which can then be modeled and refined.

2.6.4 Extrapolated electron density map

In pump-probe type experiments, the pump pulse excites only a small fraction of molecules in the crystal. It is estimated that the population transfer from dark state to activated state is only

5-10%. A structure refinement against the structure factors of the activate state only would be impossible. Then an additional map called extrapolated electron density map (EED_{map}) is calculated (Genick et al., 1997; Pandey et al., 2019). The extrapolated structure factors amplitudes, $|F^{ext}|$, are calculated as

$$|F^{ext}| = |F_{calc}^{dark}| + N\Delta|F| \quad 2.37$$

where N is a multiplication factor. At the correct value of N the strong negative features in the EED_{map} just vanishes. If N is too low, structural displacements will be ill determined. And if N is too large, false-negative features will appear in the EED_{map}. Therefore, N must be estimated accurately to calculate meaningful EED_{map} from F^{ext} . The value of N is determined iteratively. Starting with $N=1$, F^{ext} is calculated and extrapolated electron density maps are produced. N is increased and the process is repeated. The negative electron density for each N is integrated and plotted as a function of N (Pandey et al., 2019). At a certain characteristic value N_C , the integrated negative features diverge. The EED map thus produced with the $N = N_C$ will be used for the structural refinement of the activated state. The occupancy of the intermediate is $2/N_C$ (Pandey et al., 2019). Since occupancies can be much less than 10 %, the factor N can be large.

2.6.5 Analysis of DED maps by singular value decomposition

Singular value decomposition (SVD) is a mathematical tool used for deconvolution and noise reduction (Henry & Hofrichter, 1992). SVD has been successfully used in the analysis of spectroscopic data, molecular dynamics simulations, etc. Refer to review by Alter and colleagues (Alter et al., 2000) for more information. When applied to crystallographic data, SVD can be used to reduce noise in the data, to determine the time-independent structures of the intermediates, and to extract a compatible chemical, kinetic mechanism from the X-ray data (Schmidt et al., 2003).

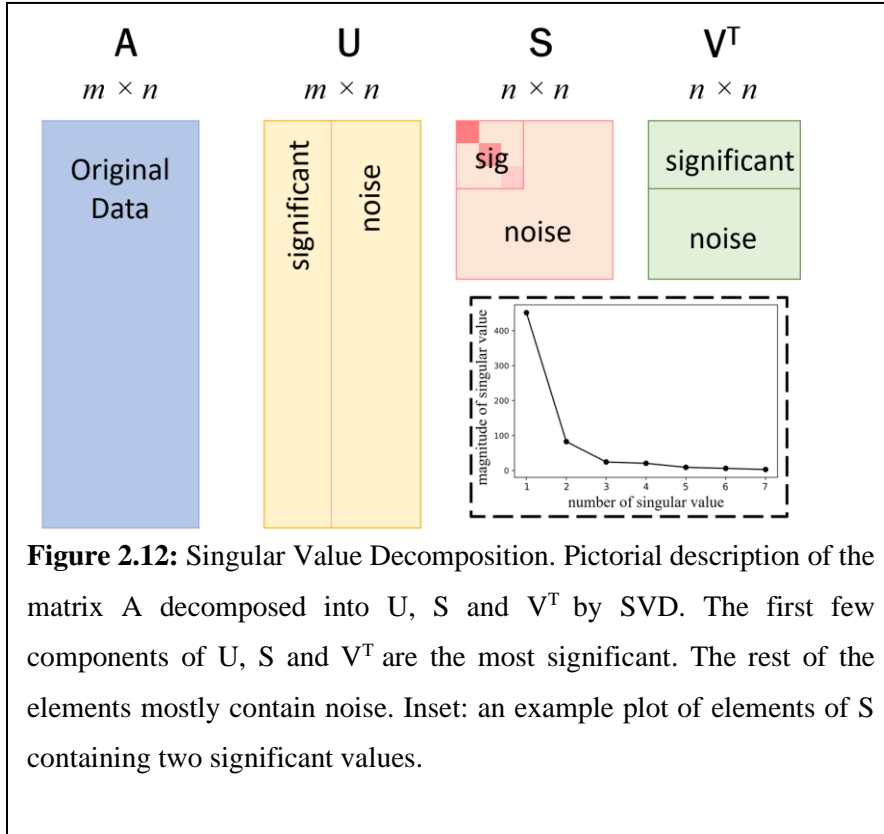


Figure 2.12: Singular Value Decomposition. Pictorial description of the matrix A decomposed into U , S and V^T by SVD. The first few components of U , S and V^T are the most significant. The rest of the elements mostly contain noise. Inset: an example plot of elements of S containing two significant values.

A DED map can be represented by a three-dimensional (3D) array that covers the entire unit cell of the crystal. The unit cell lengths a, b and c are divided into m_x, m_y and m_z number of grids respectively. Each 3D grid point (voxel) contains the value of electron density at that

given position. All the m voxels in the box can be converted into a one-dimensional (1D) column array, a vector in high (m) dimensional space. How the conversion is achieved does not matter as long as the same protocol is applied to all the n DED maps. The $m \times n$ data matrix A is constructed by arranging the n of the m -dimensional vectors in ascending order of time (Fig. 2.12). SVD then decomposes the data matrix A into matrices U , S and V according to equation.

$$\mathbf{A} = \mathbf{U} \cdot \mathbf{S} \cdot \mathbf{V}^T \quad 2.38$$

U is a $m \times n$ matrix each of whose n columns are called the left singular vectors (LSVs). They represent the basis vectors of the original data (in data matrix A). S is a $n \times n$ diagonal matrix whose diagonal elements are the singular values (SVs) of A . These non-negative values indicate how important or significant columns of U are. V^T , a transpose of matrix V , is a $n \times n$ matrix each

of whose n rows are called the right singular vectors (rSVs). These contain the associated temporal variation of the singular vectors in \mathbf{U} . Both \mathbf{U} and \mathbf{V} are unitary matrices i.e., $\mathbf{V}^T\mathbf{V} = \mathbf{U}^T\mathbf{U} = \mathbf{I}$.

\mathbf{S} contains n singular values in descending order. By selecting only k (\mathbf{S}' [$k \times k$]) significant values (where $k < n$), and the corresponding lSVs (\mathbf{U}' [$m \times k$]) and rSVs (\mathbf{V}'^T [$k \times n$]), the original data matrix \mathbf{A} can be approximated as \mathbf{A}' .

$$\mathbf{U}' \cdot \mathbf{S}' \cdot \mathbf{V}'^T = \mathbf{A}' \approx \mathbf{A} \quad 2.39$$

SVD can separate the strong signal contained in the first few significant lSVs from noise present in the remaining lSVs. By ignoring the insignificant singular vectors and values, a noise filtered data matrix \mathbf{A}' can be obtained.

The number of significant singular values can tell how many kinetic processes can be resolved (Fig. 2.12 inset). The SVD results can then be interpreted by globally fitting trial functions (for example exponential functions) to the rSVs. The rSVs contain information on the population dynamics of the species involved in the mechanism. For more information refer to Henry and Hofrichter (Henry & Hofrichter, 1992), and Schmidt et al (Schmidt et al., 2003).

2.7 Cryo-EM

The term ‘cryo-EM’ has been loosely used to refer to macromolecular structure determination. In practice, this refers to the single-particle analysis method. This method is based on recording a large number of TEM images of the macromolecule. Individual images are noisy and hard to interpret. Combining several images of same object produces an image with stronger contrast which are more easily interpretable. These images are combined to recover the 3D structure of the molecule. The structure can be reconstructed at sub nanometer to atomic

resolutions. The main advantage with this technique over crystallographic methods is that the proteins are in a non-crystalline state that can be considered closer to the native state than in crystals. There are no steric or lattice constraints that may limit the functional states they can assume.

2.7.1 Cryo-EM data collection

Cryo-EM data is collected in a high vacuum environment to eliminate scattering from air molecules. The sample must be prepared in such a way that they survive the harsh vacuum as well as the radiation damage caused by the ionizing electron beam. The most commonly used methods to prepare sample are (i) negative staining and (ii) vitrification.

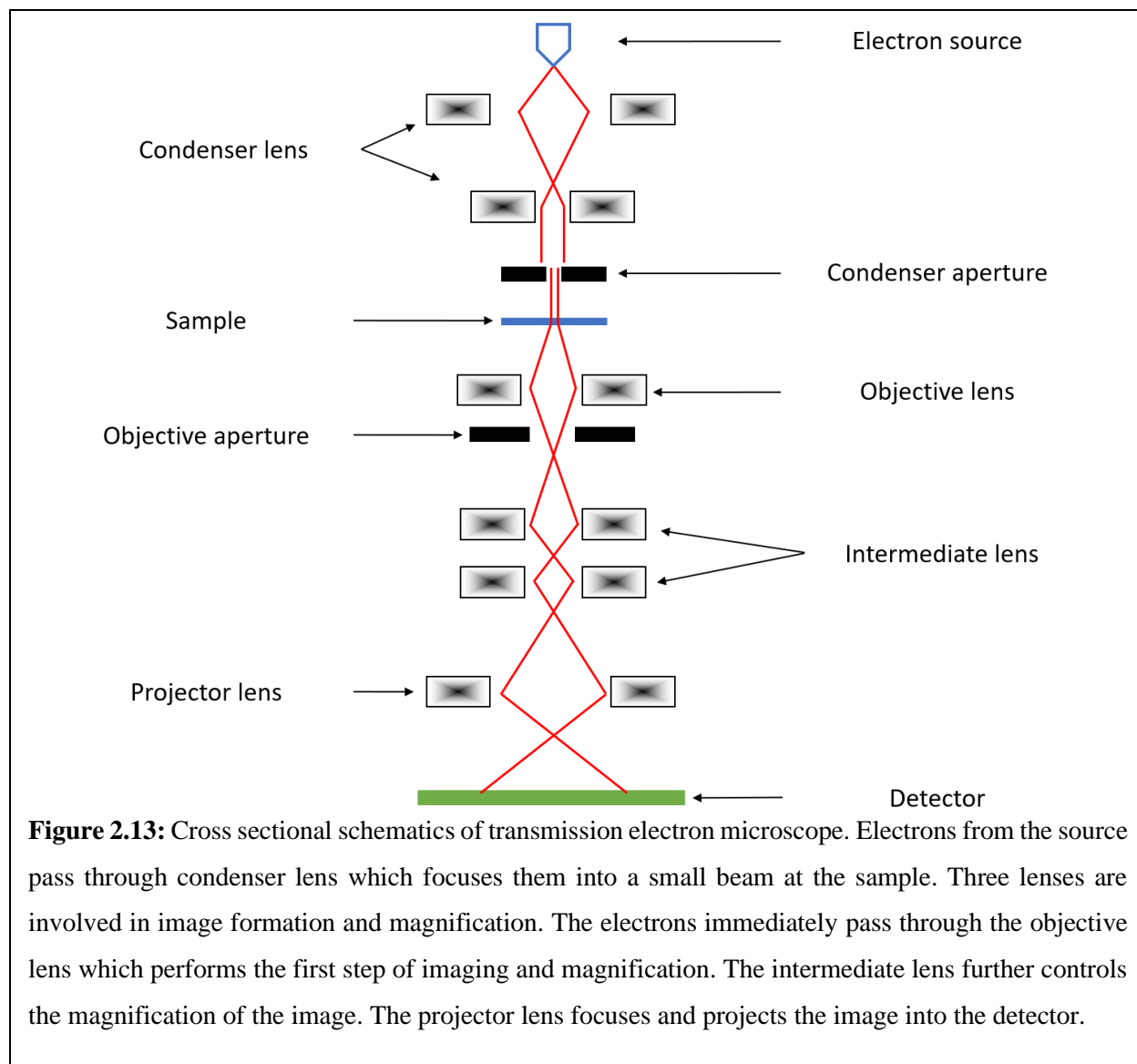
i) Negative staining is based on utilizing a heavy metal salt to improve contrast (Brenner & Horne, 1959). The heavy metal atoms are distributed around the specimen which protect the molecule from collapsing in vacuum. The heavy metals are also radiation-hard which reduces the effect of radiation damage. As a consequence, the structural information is limited to the shape of the molecule. Nevertheless, negative stained data provide valuable information on a sample, such as the size, shape and oligomeric state of the target protein or complex, and the presence of contaminants or aggregates (Cheng et al., 2015). It is also possible to observe compositional heterogeneity, as well as potential conformational variability. It is mostly used to evaluate (scan) the feasibility of a macromolecular preparation for high-resolution cryo-EM studies.

(ii) With the vitrification technique, the sample is cooled very fast which prevents the formation of damaging ice crystals (Dubochet & McDowell, 1981). This is done by depositing a thin buffer sheet containing biological macromolecules on a grid. The sample grid is plunged into a cryogen. Typically, liquid ethane cooled by liquid nitrogen is used. The sample freezes

immediately in its near native, hydrated state. Freezing protects the sample from both radiation damage and collapsing at high vacuum. Still, vitrified specimens have low inherent contrast, as the scattering of electrons from biological molecules is not much stronger than that of the surrounding buffer. Only the molecules that can scatter electrons sufficiently strongly can be distinguished from the background. This imposes a lower mass limit on molecules that can be studied by cryo-EM, which is on the order of ~50 kDa (Henderson, 1995).

The frozen EM-grids are loaded into a transmission electron microscope. The microscope is designed to operate and keep the samples at liquid nitrogen temperature during data collection. A schematic diagram of a TEM microscope is shown in Fig. 2.13. Electrons pass through a series of magnetic lenses. The first of these lenses encountered by the electrons is the condenser lens. The condenser lens system is situated just below the electron source and adjusts the electron focus and beam size. A condenser aperture may also be present that blocks the electrons with a large angular spread, which improves the beam coherence.

The energetic electrons strike the sample and scatter through different angles. The forward scattered electrons are focused by the objective lens which is placed right below the sample specimen (Fig. 2.13). This forms the initial image and defines its quality. The electromagnetic parameter of this lens is finetuned to focus the image on the detector. Similar to the condenser aperture, an objective aperture can be coupled with the objective lens to prevent excessive scattering of the electrons which in turn improves the contrast of the image. The electrons now pass through a system of intermediate lenses. The positioning and strength of these lenses control the magnification of the image. Before the detector, a projector lens is used which focuses and projects the electrons on the detector, which further increase the magnification of the image.



2.7.2 Cryo-EM data processing and analysis

At the core of single-particle cryo-EM data analysis lies the reconstruction of a 3D density map of the molecule under investigation from a set of images that represent 2D projections of the molecules in the sample grid at various orientations. Various software packages are available each of which implement different algorithms for cryo-EM data processing. The results presented in this dissertation were processed by *cryoSPARC* cryo-EM data processing software (Punjani et al.,

2017). Fig. 2.14 shows the various steps involved in the process. The critical steps are described below.

Motion correction. Using a higher electron dose increases the image contrast but also increases radiation damage. Instead of a single snapshot, a movie is recorded. A movie is a dose-fractionated stack of images collected at the same position of the grid in one exposure. During image acquisition, the sample motion occurs for various reasons which blurs the image. The sample as a whole may move (stage drift), or the sample may deform due to the energy deposited by the electron beam (anisotropic deformation). Correcting for this motion is the first step. The motion-corrected movie is called a micrograph.

CTF estimation: An accurate estimate of the CTF parameters (Eqn. 2.28) is important for both the initial evaluation of the micrograph quality and the subsequent structure determination. Some of the parameters of the CTF are obtained from the microscope settings while some are determined experimentally. For example, the wavelength and the spherical aberration are defined by the accelerating voltage and the lens design. The defocus and the astigmatism have to be estimated for each image individually. This is accomplished by adjusting the parameters so that the computed CTF approximates the amplitude oscillations observed in the power spectrum of the image. For more detail on CTF estimation and correction, see the review by Cheng and colleagues (Cheng et al., 2015).

Particle picking: In this step, the 2-D projections (particles) of the molecules are detected and extracted from the noisy micrographs. High-resolution reconstruction requires hundreds of thousands of particles. Picking them manually is a tedious process. Many automatic algorithms

are available based on edge detection techniques, machine learning and template matching (Scheres, 2015; Wagner et al., 2019; Zhu et al., 2017).

2D classification: The particles are divided into several classes each with similar orientations and averaged to increase the SNR. The averaged images are called *2D classes* or *class averages*. The non-informative and low-quality *class averages* can be discarded. The particles belonging to ‘good’ *class averages* are used for an *ab initio* construction of the model. In addition, the *class averages* provide valuable information on data quality including symmetry and particle homogeneity.

3D reconstruction: Using the selected particles it is possible to reconstruct one (homogenous) or more (heterogenous) 3D maps from a set of particles, without any initial model. *CryoSPARC* uses a Stochastic Gradient Descent (SGD) algorithm (Bottou, 2010) to generate an *ab initio* model. In short, initializations are generated by selecting a small random subset of images from the dataset (typically 10 images), assigning them randomly generated pose angles, and using them to reconstruct a 3-D volume. This volume is fed into SGD. SGD is able to converge to correct structures from arbitrary randomly generated initializations containing no prior structural knowledge or user expertise. More information on this implementation can be found in the supplementary material of the original *cryoSPARC* publication (Punjani et al., 2017).

Map refinement: After obtaining an initial map, the map needs to be improved (called refinement in cryoEM) to obtain the final map with better details. All cryo-EM data processing packages use a 3D projection matching procedure for map refinement (Cheng et al., 2015). It modifies the orientation parameters of projections to achieve a better match with reprojections computed with the current instance of the map (Penczek, 2010). During the refinement, the dataset is divided into two independent halves that are reconstructed separately. At the end of each reconstruction

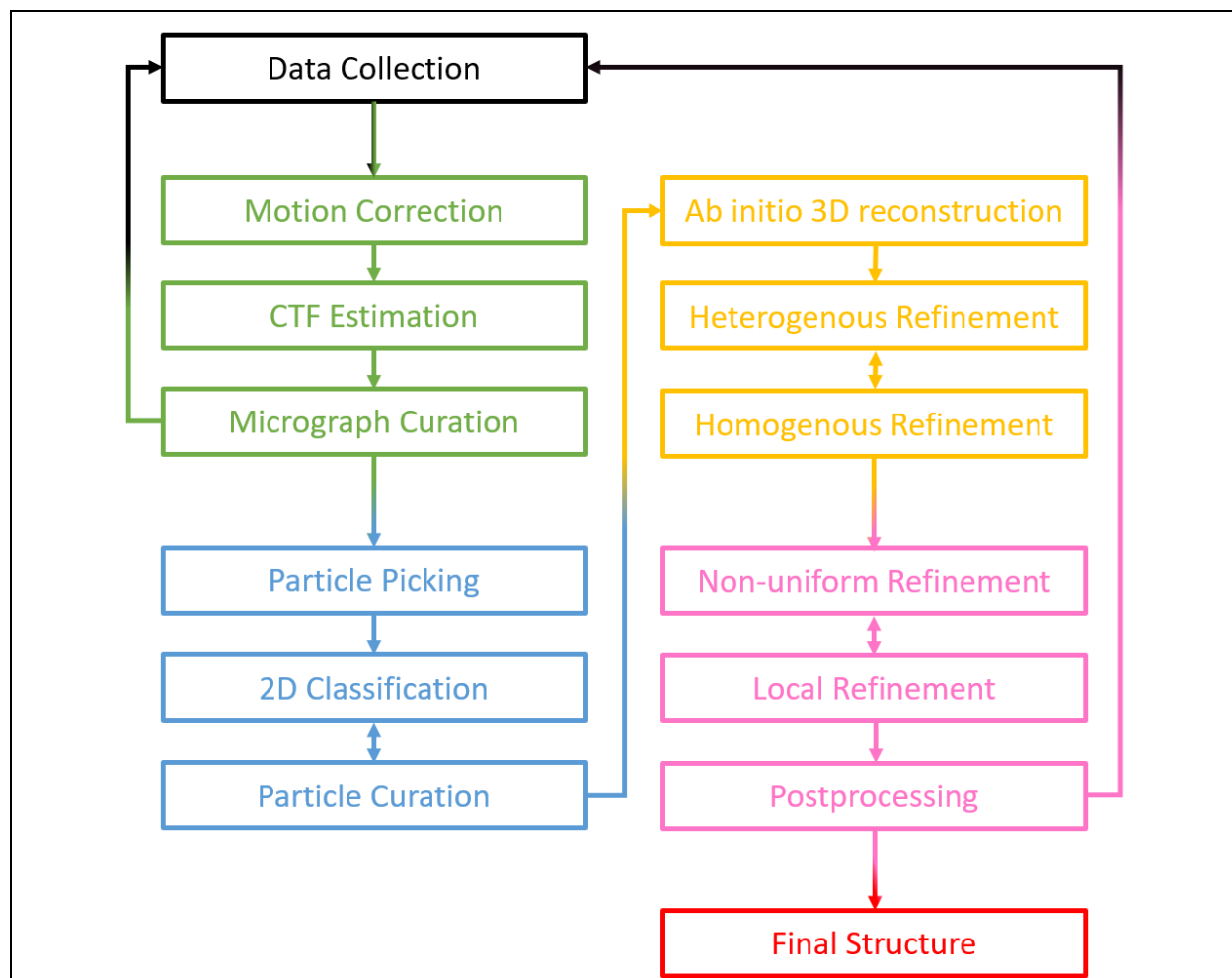


Figure 2.14: Typical work flow for cryo-EM data processing with *cryoSPARC* program. Once the cryo-EM data is collected in the form of movies, they need to be pre-processed as shown in the green panels. It involves motion correction, CTF estimation and the screening of micrographs. The curated micrographs are used for particle selection process shown in blue panels. Particles are picked from the micrographs and classified into several 2D classes. The best ones are selected and used for 3D reconstruction shown in yellow panels. An *ab initio* map or many such maps are constructed and refined. Further processing steps shown in pink are required if there are flexible and poorly refined regions in the 3D reconstructed map.

iteration, the correlation coefficients within resolution shells extracted from Fourier transforms of the two volumes are computed. This process is called Fourier shell correlation (FSC). The FSC curve (plotted as function of resolution) provides information on the level of the SNR as a function of the spatial frequency and the resolution of the map. The resolution is obtained by comparing

the measured FSC to a threshold value. Usually, a threshold of $FSC = 0.143$ is chosen based on relating EM results to those in X-ray crystallography (Rosenthal & Henderson, 2003). A heterogenous refinement can also be performed which simultaneously classifies particles and refines maps from n initial maps. Small differences between maps which may not be obvious at low resolutions may become identifiable.

The map generated by cryo-EM processing is a real space 3D electron potential map. Unlike in crystallography, there is no *phase problem*. An atomic model can directly be placed in the map and refined.

2.8 Application of the methods discussed above to various protein samples

The methods described in this chapter have been applied to study proteins posed in section 1.5. The three proteins are presented individually in the next three chapters. Each protein is introduced and specific methods (if applicable) are listed. Results are presented and discussed for each specimen.

3. Beta (β) Lactamase

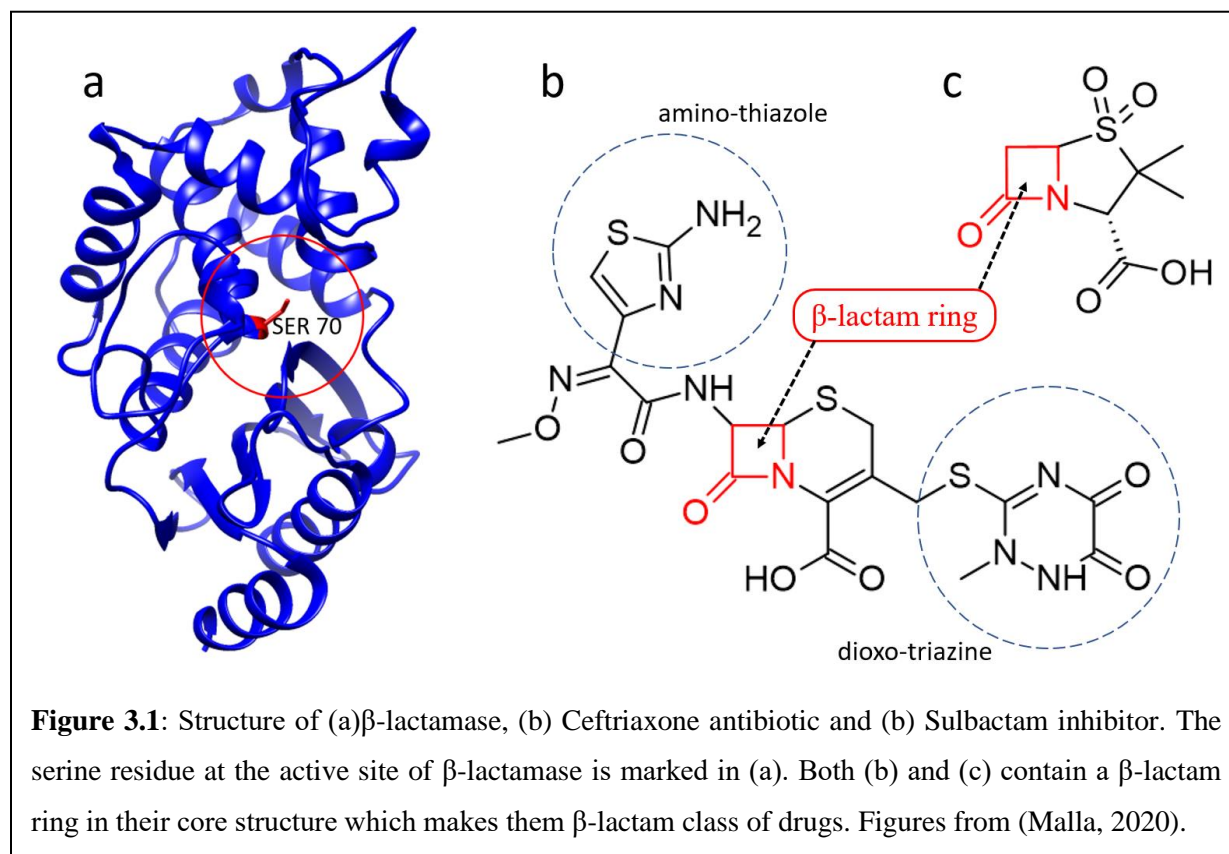
At the time of this writing, the manuscript reporting the work done that is presented in this dissertation is accepted at *Nature Communications* journal under the title ‘Heterogeneity in *M. tuberculosis* β -Lactamase Inhibition by Sulbactam’(Malla et al., 2023). Most of the figures displayed here are reproduced from the same manuscript. In this project, I have been involved in protein purification and crystallization, data collection, data analysis and writing of the final manuscript.

3.1 Introduction

β -lactamases (Fig. 3.1 a) are enzymes produced by bacteria that provide resistance to β -lactam antibiotics. β -lactam antibiotics are frequently used for the treatment of bacterial infections as they are effective against both gram positive and negative bacteria (Lewis, 2013). This class of antibiotics includes penicillin derivatives (penems), cephalosporin derivatives (cephem), monobactams, carbapenems and carbacephems (Ellen Jo Baron James H. Jorgensen & Murray, 2007). Penicillin-binding proteins present in bacterial cell walls catalyze the linkage of N-acetylmuramic acid to N-acetyl-D-glucosamine to form the cell wall (Nelson & Cox, 2017). β -lactam antibiotics inhibit the penicillin-binding protein. Once blocked by these compounds, the enzyme is not able to maintain the integrity of the cell wall and the bacteria perish. Unfortunately, resistance against these antibiotics was observed shortly after their widespread use (Fair & Tor, 2014; Walsh, 2000).

The β -lactamase that we investigated is isolated from *Mycobacterium tuberculosis* (Mtb)- the causative agent of tuberculosis disease. Mtb β -lactamase (BlaC) is a broad-spectrum Ambler class A (Ambler, 1980) β -lactamase capable of hydrolyzing all classes of β -lactam antibiotics. Every

year tuberculosis claims around 1.5 million lives worldwide (World Health Organization, 2021). Research efforts focused on deciphering the molecular mechanism of antibiotic resistance within microbial pathogens such as *Mtb* can aid in novel-drug design, resistant to β -lactamase action, and therefore, contribute to managing this evolving crisis.



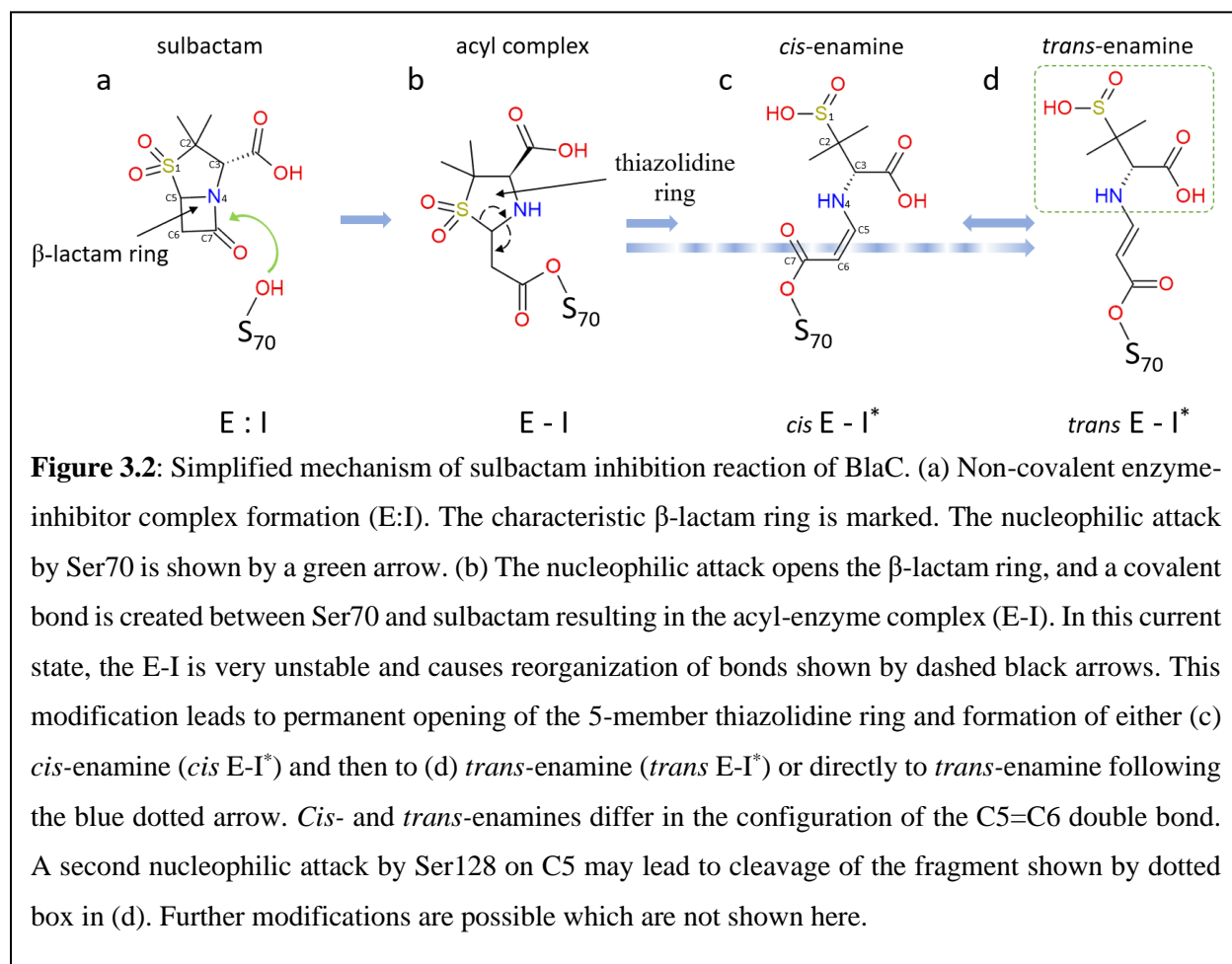
β -lactam antibiotics are characterized by a four-atom ring called the β -lactam in their molecular structure (Fig. 3.1 b). β -lactamases attack this ring and break it open through hydrolysis. The modified product is released, and the free enzyme can engage in subsequent cycles of antibiotic modification. β -lactamase inhibitors represent potential new drugs in the fight against antibiotic resistance. β -lactam inhibitors are similar in structure to the β -lactam antibiotics (Fig. 3.1 c). They

irreversibly bind to β -lactamases and eliminate their activity. As a result, the β -lactam antibiotics are protected from enzymatic degradation, and retain their efficacy.

Although several static X-ray structures of BlaC with various substrates have been determined (Hugonnet & Blanchard, 2007; Naas et al., 2017; Padayatti et al., 2005; Tassoni et al., 2019; Tremblay et al., 2008, 2010; Wang et al., 2006), the reaction intermediates of BlaC reaction involving different antibiotic substrates remain mostly unknown. The macrophage compartment where the *Mtb.* resides is rather acidic at pH \sim 4.5. At this pH BlaC crystallizes as a dimer of dimer with four subunits A - D in the asymmetric unit (Fig. 3.3 a) (Kupitz et al., 2017; Xie et al., 2012). Using MISC with these crystals, our lab has already characterized intermediates of BlaC reacting with the third-generation cephalosporin-based antibiotic, ceftriaxone (CEF) (Fig. 3.1 a) from 5 ms to 2s (Olmos et al., 2018; Pandey et al., 2021). The initial substrate binding phase that leads to the formation of the enzyme-substrate complex, as well as the structure of a covalent enzyme-substrate adduct (the so-called acyl-complex) was determined.

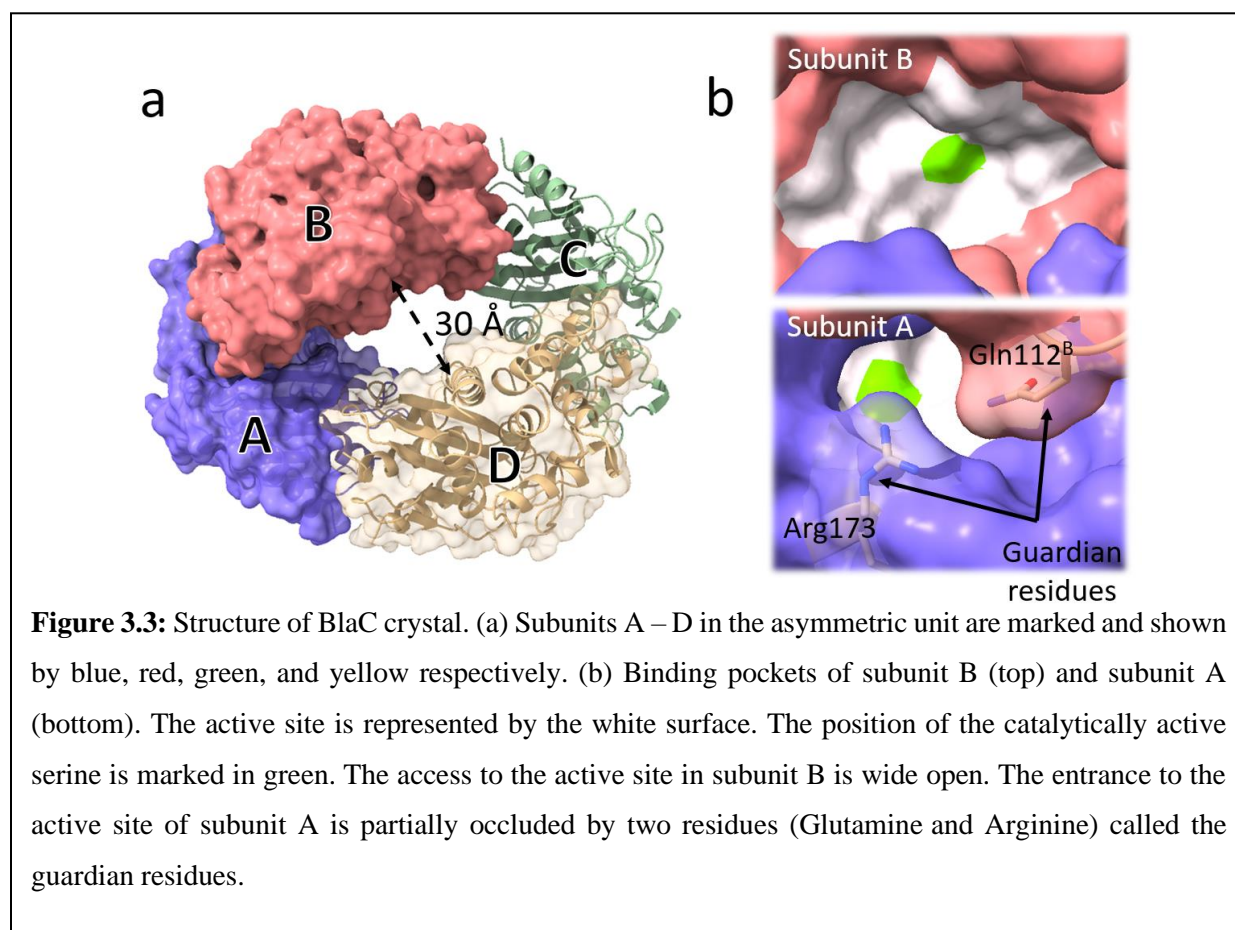
Similar time-resolved studies on BlaC reaction with inhibitors are necessary. Due to its excellent solubility, the sulbactam (SUB) (Fig. 3.1 c) inhibitor is a superb ligand candidate for a MISC experiments involving BlaC. Raman microscopy and mass spectrometry suggest a simplified mechanism for SUB binding to BlaC (Bush et al., 1993; Helfand et al., 2003), shown in Fig. 3.2. The β -lactam ring is attacked by the Ser-70 nucleophile. A short-lived, covalently bound acyl-enzyme intermediate is formed. The intermediate is unstable and causes reorganization of the bonds as shown in (Fig. 3.2 b). This modification leads to the permanent opening of the 5-member thiazolidine ring. The modified SUB can form either cis-enamine (Fig. 3.2 c) and then to trans-enamine (Fig. 3.2 d) or directly to trans-enamine. On longer timescales, another nucleophilic attack

by Ser-128 may lead to the cleavage of the fragment shown by dotted box in (Fig. 3.2 d). The structure of some intermediates shown in Fig. 3.2 are relevant to the observed results presented in this dissertation within the measured timescale. Further modification and reaction pathways are possible which are discussed elsewhere (Drawz & Bonomo, 2010).



Recently, Pandey and colleagues captured an intermediate (presumably E:I) of the BlaC-SUB reaction at a single time point (66 ms) in an earlier MISC experiment (Pandey et al., 2021). Although subunits B and D displayed already a covalently bound adduct, an intact, non-covalently bound SUB was observed in subunits A and C. Subunits A/C are rather inactive, since they did not participate at all in the reaction with the β -lactam antibiotics CEF in earlier experiments (Kupitz

et al., 2017; Olmos et al., 2018). Given the inactivity of subunits A/C, it was not clear whether the reaction with SUB takes more time to complete or proceed at all. Therefore, a time-series of MISC datasets is necessary, to further investigate both the binding of SUB inhibitor to and its subsequent reaction with the BlaC in regard to individual subunits of this protein. This dissertation reports on the TRX experiment performed on BlaC reaction with an inhibitor, sulbactam (SUB).



3.2 Methods

3.2.1 Protein purification and crystallization

BlaC was expressed in *E. coli* and purified as previously described (Olmos et al., 2018). *E. coli* culture were grown in terrific broth at 37° C to a OD₆₀₀ value of 0.8. The culture was induced

by 1 mM isopropyl- β -D-thiogalactopyranoside (IPTG) after lowering the temperature to 20° C. After 3 hours, the culture was induced a second time with 1 mM IPTG, and shaken overnight at 20° C. The mature cells were harvested by centrifugation. Cells were resuspended in lysis buffer (20mM Tris Base, 150 mM NaCl, pH 8.). After lysis of the bacterial cells, debris was centrifuged at 50,000 g for 1 hour. The lysate was then pumped through a column containing 15 mL of Nickel resin. The resin was washed with a buffer consisting of 20 mM Tris Base, 300 mM NaCl, 20 mM Imidazole, pH 8 (about 20 column volumes each). The final product was eluted by 300 mM imidazole and dialyzed immediately in 20 mM Tris base, 200 mM NaCl, pH 8. The protein was further purified through size exclusion chromatography using Superdex 200 resin.

Microcrystals of BlaC were grown in batch mode for MISC investigation. Purified BlaC protein (concentrated to 150 mg/ml) was added dropwise to 2.4 M ammonium phosphate (AP) at pH 4.1 while stirring until a ratio of 1:9 (protein: precipitant) was reached. The stirring was stopped after ~12 hours. Protein microcrystals were left to mature for 2 days at room temperature. As the crystals settle, the supernatant was removed to reach the desired concentration. The final concentration of crystals was 5×10^9 crystals/ml. To investigate SUB binding to BlaC on a longer time scale, macroscopic crystals were grown in sitting drops (10 μ l BlaC at 45mg/ml⁻¹ mixed in a 1:1 ratio with 2.1 M AP at pH 4.1). Crystals were soaked for 3 hours in a cryobuffer consisting of 2 M AP, 20% glycerol and 100 mM SUB. The crystals were flash frozen in liquid nitrogen for data collection.

3.2.2 Data collection

Data were collected at the Macromolecular Femtosecond Crystallography (MFX) instrument (Boutet et al., 2016) at the LCLS. The XFEL was operating at 120 Hz with a pulse

energy of ~ 9.8 keV ($\lambda = 1.26$ Å) and a pulse duration of 20-40 fs. The XFEL beam was focused to a spot size (FWHM) of 3 μm . Special injectors were used which allow simultaneous mixing and serial injection of sample into the X-ray interception region (Calvey et al., 2016, 2019). The crystal slurry was mixed with SUB solution and injected into a helium filled chamber at ambient temperature. For mixing, a solution of 150 mM SUB in 50mM AP at pH 4.5 was prepared. A reference (unmixed) dataset was obtained by mixing the BlaC microcrystals with water. The geometry of the injectors and the sample delivery parameters are shown in Tab. 3.1.

Table 3.1: Injector geometry and sample flow rates

	Water	Sulbactam					
Δt_{MISC} (ms)	0	3	6	15	30	240	700
Ligand concentration (mM)	n.a.	150					
Ligand buffer	water	50 mM Ammonium Phosphate (pH 4.5)					
Injector ID	3	1	1	2	2	3	4
Crystal flow rate ($\mu\text{l}/\text{min}$)	10	7.7	7.6	7.7	11.1	10.1	11
Ligand flow rate ($\mu\text{l}/\text{min}$)	70	142.3	67.4	143.1	63.1	70	57
Constriction [†] inner diameter (μm)	100	50	50	50	50	100	100
Constriction length (mm)	82.7	10.3	10.3	40.7	40.7	82.7	35
Timing uncertainty (ms)	n.a.	± 1.0	± 2.0	± 1.1	± 3.5	± 18.8	± 29.5
[†] Crystals and ligand flow concentrically before being combined into a single outlet of reduced diameter called the mixing constriction.							

Diffraction patterns (DPs) were collected with the epix10K2M detector (Brandt Van Driel et al., 2020) at 120 Hz. The experiment was monitored in real time with the *OnDA* (online data analysis) *Monitor* (OM) (Mariani et al., 2016), which also provided feedback on hit rate and spatial resolution. The raw data were processed by *Cheetah* (Barty et al., 2014) to determine images with Bragg reflections. The selected patterns were further processed by the *CrystFEL* suite of programs

(White, 2019; White et al., 2012). The macroscopic crystals were investigated at beamline ID-19 of APS. Data were collected by the proprietary *sbccollect* program (Rosenbaum et al., 2006) and processed by *HKL3000* (Minor et al., 2006). The data collection statistics for various time points are given in Tab. 3.2.

Table 3.2: Data collection statistics for BlaC

	Water	3ms	6ms	15ms
Space Group	P2 ₁			
Temperature	293 K			
a,b,c (Å), β(°)	79.6, 98.1, 110.9, 108.5	80.5, 98.8, 111.5, 108.5	80.4, 98.8, 112.1, 108.7	80.3, 98.6, 112.1, 108.8
Resolution range (Å)	22.14-2.2 (2.3 - 2.2) [†]	22.01-2.6 (2.75-2.6)	20.53-2.75 (2.85-2.75)	20.86-2.65 (2.75-2.65)
Hits	88,978	61,508	26,309	51,166
Indexed patterns	73,965	36,400	17,596	31,958
Observed Reflections	37, 857, 581	14, 718, 802	6, 258, 604	11, 092, 596
Unique reflections	83, 447	42, 822	43, 284	40, 586
Multiplicity	453 (335)	343 (164)	144 (69)	273 (130)
Completeness	100 (100)	100 (100)	100 (100)	100 (100)
R _{split/merge} (%)	23.3 (528)	23.4 (427)	24.3 (354)	23.6 (316)
CC* (%)	99.6 (69.8)	99.3 (55.9)	99.0 (51.6)	98.9 (58.7)
	30ms	240ms	700ms	3 h soak
Space Group	P2 ₁			
Temperature	293 K		100 K	
a,b,c (Å), β(°)	80.2, 98.5, 112.3, 108.9	79.8, 97.9, 113.2, 109.3	80.0, 98.3, 112.1, 108.8	79.4, 96.7, 111.1, 108.5

Resolution range (Å)	20.4-2.95 (3.06-2.95)	22.42-2.35 (2.43-2.34)	20.94-3.2 (3.38-3.2)	22.3-2.7 (2.8-2.7)
Hits	27,143	75,038	2,854	n.a
Indexed patterns	11,123	59,928	2,740	n.a
Observed Reflections	3, 888, 789	29, 990, 504	1, 582, 566	n.a
Unique reflections	32, 517	68, 441	27, 514	38, 773
Multiplicity	119 (67)	446 (306)	57 (35)	2.7 (1.3)
Completeness	100 (100)	100 (100)	99.9 (99.9)	78.8 (26)
R _{split/merge} (%)	30.4 (176)	28.8 (689)	44.6 (208)	18.2 (803)
CC* (%)	98.2 (52.9)	99.3 (64.2)	95.9 (51.3)	99.6 (64.2)
† Values in parentheses represent the highest resolution bin				

3.2.3 Difference maps and structure determination

Because of the change in unit cell parameters, omit difference electron density (DED_{omit}) maps were calculated throughout (as described in section 2.6.2). Polder difference (DED_{polder}) maps (Lieschner et al., 2017) were calculated to display weak ligand densities in some time points to assist in the placement of the ligand. DED_{polder} map is generated by excluding bulk solvent modeling around the selected region. Weak densities which may otherwise be obscured by the bulk solvent become apparent. DED_{polder} maps were calculated particularly for the 30ms and the 700ms timepoint, due to the relatively low number of indexed DPs (Tab. 3.1), and for the cryosoaked data.

Both the unbound sulbactam and the covalently bound *trans*-enamine (TEN) were manually modeled into the DED maps using *Coot* (Emsley et al., 2010). The *CCP4* program *AceDRG* (Long et al., 2017) was used to generate coordinates and restraint for the covalently bound TEN. Refinement was performed with *Phenix* followed by manual inspection and re-modeling with *Coot*.

Ligand occupancies were determined by ‘group occupancy refinement’ in *Phenix*. A value of 100% indicates that the active site is saturated with ligand. The refinement statistics are listed in Tab. 3.3.

Table 3.3: Refinement statistics for BlaC

	Water	3ms	6ms	15ms
Resolution range (Å)	22.14-2.2	22.01-2.6	20.53-2.75	20.86-2.65
Reflections used	68, 064	40, 968	41, 929	38, 742
R _{cryst} /R _{free}	0.22/0.25	0.22/0.24	0.22/0.24	0.23/0.26
Occupancy (in %)	n.a	n.a.	n.a.	TEN ^{B,D} : 96, 90
r.m.s.d [‡] bond length (Å)	0.004	0.002	0.003	0.003
r.m.s.d bond angles (°)	0.641	0.545	0.601	0.642
No. of H ₂ O	447	140	203	183
	30ms	240ms	700ms	3 h soak
Resolution range (Å)	20.4-2.95	22.42-2.35	20.94-3.2	22.3-2.7
Reflections used	33, 082	53, 680	27, 127	25,400
R _{cryst} /R _{free}	0.22/0.26	0.23/0.25	0.27/0.29	0.22/0.27
Occupancy (in %)	SUB ^{A,C} : 52, 63 TEN ^{B,D} : 85, 77	TEN ^{A,B,C,D} : 100	TEN ^{A,B,C,D} : 100	TEN ^{A,B,C,D} :98, 96, 98, 88
r.m.s.d [‡] bond length (Å)	0.003	0.003	0.002	0.003
r.m.s.d bond angles (°)	0.768	0.65	0.428	0.584
No. of H ₂ O	44	311	16	90
^{A,B,C,D} The superscript letters represent corresponding subunits.				
[‡] root mean square deviation				

3.2.4 Adapting singular value decomposition for non-isomorphous datasets

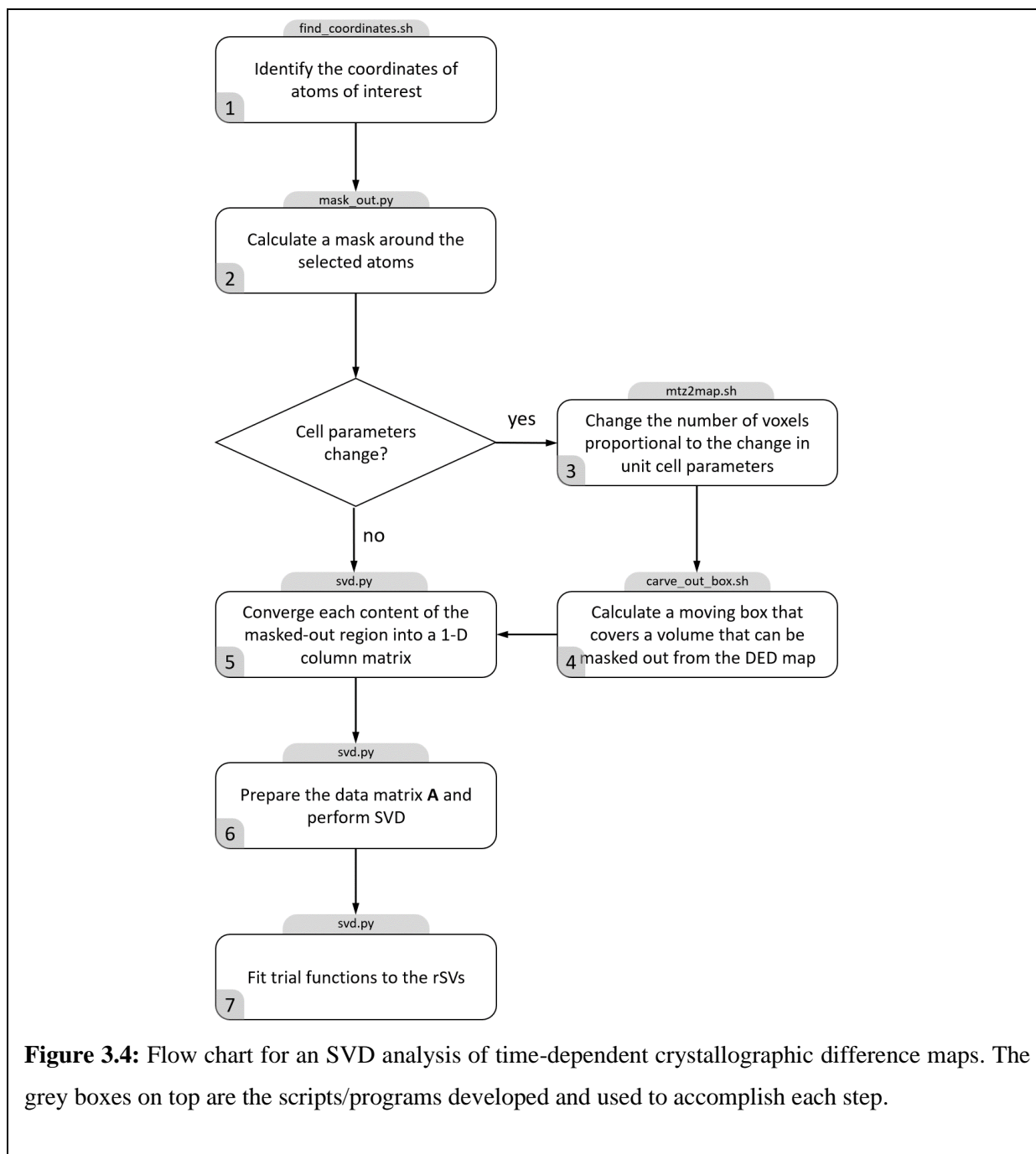
The earlier programs for performing singular value decomposition, SVD4TX (Schmidt et al., 2003) and a newer version (Zhao & Schmidt, 2009) could not be applied to X-ray data when

large unit cell changes occur during the reaction since isomorphous difference maps cannot be calculated. In addition, these implementations relied on a fixed region of interest which is not given when the unit cell changes. As seen on Tab. 3.3, the unit cell parameters change by up to 3 Å between different time points. A combination of custom bash scripts and python programs were written in order to accommodate changing unit cells (Malla, 2023). Additionally, most of the map contains only spurious noise except in regions of interests (ROIs) such as the active sites where larger structural changes are expected due to the binding or dissociation of a ligand. The noise within the majority of the difference map would interfere with the SVD analysis. To avoid this, an ROI can be isolated, and an SVD performed only on the DED within. When multiple active sites are present, each active site can be investigated separately. Fig. 3.4 shows a flow chart of the steps required to prepare data matrix **A** that account for changing unit cells and defining a region of interest. The steps are described in detail below.

Step 1: The coordinates of the atoms of the amino acid residues and the substrate of interest are specified in a particular subunit. This defines the ROI.

Step 2: A mask is calculated that covers the selected atoms plus a margin of choice (Fig. 3.5 b). The density values outside of the mask are set to 0, while the ones inside are left unchanged. This results in a masked map with the dimensions of the original map with density values present only around the emerging DED in the active site (Fig. 3.5 c). This mask evolved later (after step 4) by allowing only grid points that contain DED features greater or smaller than a certain sigma value (for example, plus or minus 3σ) found at least in one time point.

When the unit cell parameters do not change during the reaction, the difference maps at all time points will have the same number of voxels, and the voxel size is also constant. However, once the



unit cell dimensions change, either the voxel size will change if the number of voxels is kept constant or the number of voxels will change if the voxel size is kept constant. If the voxel size changes, the DED value assigned to each voxel position will also change, which will skew the SVD analysis. If the voxel numbers change, the SVD algorithm will fail because it requires that

all the maps are represented by arrays of identical sizes. Accordingly, both conditions, (i) a constant voxel size and (ii) a constant number of grid points in the masked volume, must be fulfilled when the unit cell changes.

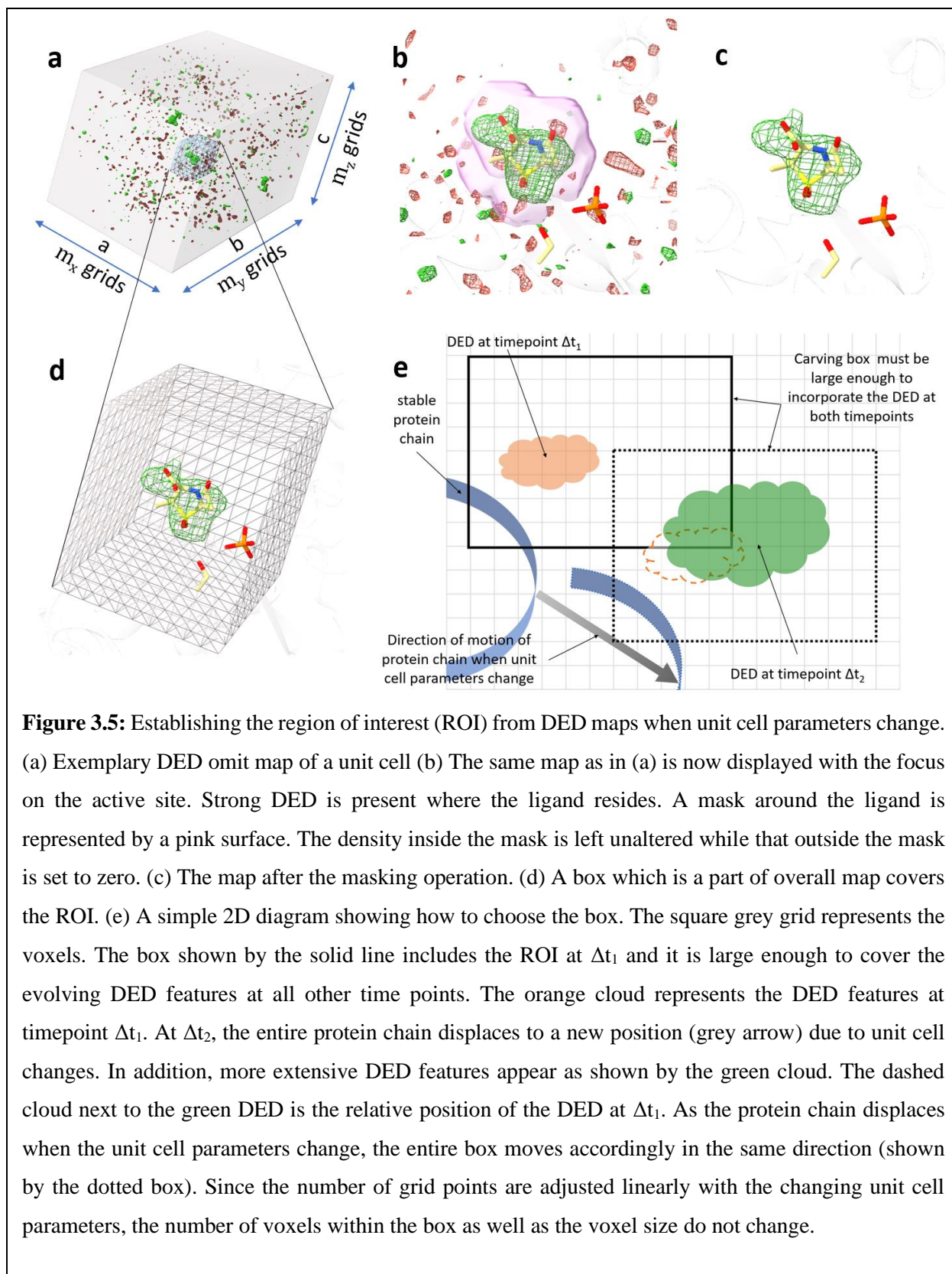
Step 3: To fulfill (i), the total number of grid points in the DED map is changed proportionally to the unit cell change. When the volume of the ROI is not changed, condition (ii) is automatically fulfilled, and a suitable data matrix **A** can be constructed. However, when the unit cell parameters change, the ROI also changes position. This must be addressed in addition.

Step 4: A box is chosen that will cover the density that was just masked out (Fig. 3.5 d). The box will include the ROI, which is saved as a new map. The size of the box must be large enough such that the ROIs can be covered at all time points. The box must be calculated with reference to a stable structure (usually the protein main chain). As the protein chain displaces as a result of the change in the unit cell, the box will also move accordingly to cover the correct ROI (Fig. 3.5 e). As mentioned, the DED within the moving box can be used to evolve the mask that defines the final ROI, as indicated in step 2.

Step 5: All m voxels in the evolved mask are converted to a one-dimensional (1D) column array, a vector in high (m) dimensional space. How the conversion is achieved does not matter as long as the same convention is applied to all n maps. N of the m -dimensional vectors are arranged in ascending order of time to construct the data matrix **A**.

Step 6: SVD is performed on matrix **A** according to Eqn. 1.

Step 7: Trial functions are globally fit to the significant rSVs to determine relaxation times and the minimum number of intermediates involved in the reaction (Ihee et al., 2005).



The right singular vectors (rSVs) obtained from the SVD analysis plotted as a function of collected timepoints represent the temporal variation of the reaction (Schmidt et al., 2003). For a simple chemical kinetic mechanism with only first-order reactions, relaxations are characterized by simple exponentials (Steinfeld et al., 1998). For higher order reactions, the rSVs have to be fitted by suitable functions which must explain the changes of the electron density values in a chemically sensible way (Moffat, 2001; Ren et al., 2001b; Schmidt et al., 2003).

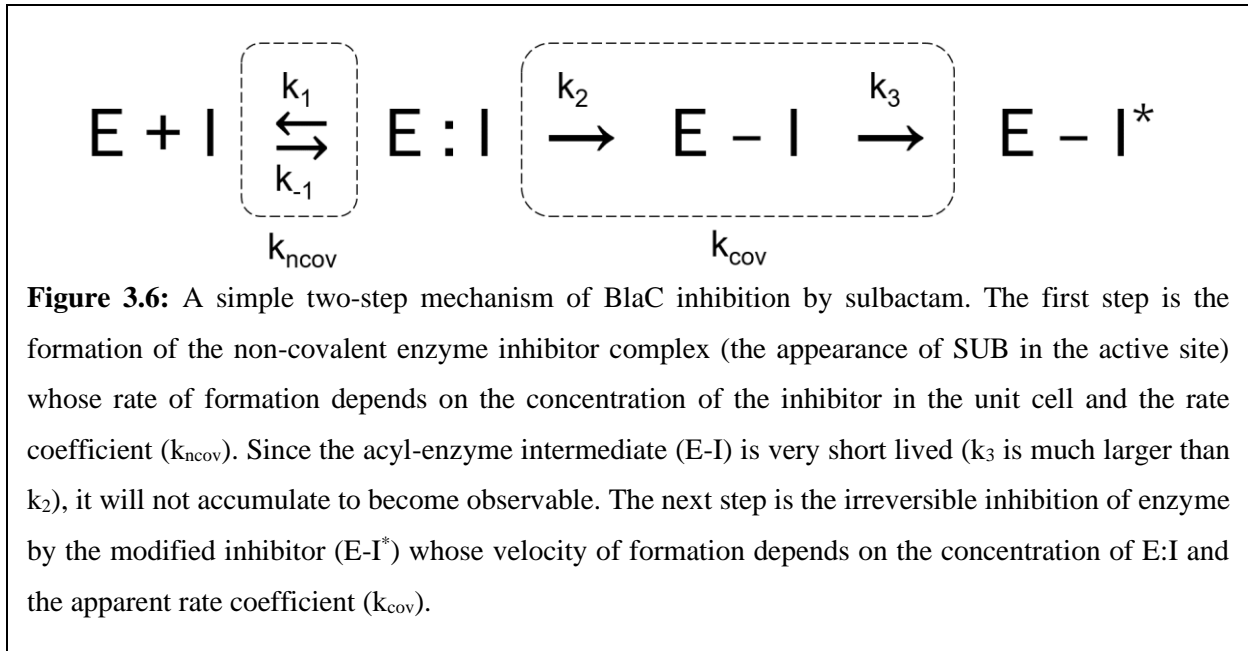
3.2.5 Characterization of inhibitor diffusion and concentrations of intermediates

The diffusion of SUB molecules into the BlaC crystals and subsequently into the active sites triggers the reaction. Concentrations of SUB in the central flow were estimated according to Calvey et al. (Calvey et al., 2019). At the longest $\Delta t_{\text{MISC}} = 700$ ms, the SUB concentration was 100 mM, which was used as the maximum ligand concentration for all calculations. The resulting evolution of concentration of SUB at the active sites was modeled by Eqn. 3.1.

$$I(t) = \frac{I_{max}}{1 + e^{-\mu(t-t_0)}} \quad 3.1$$

$I(t)$ is the concentration of SUB at the active sites averaged over all unit cells in the crystal as a function of time and I_{max} is the maximum (100 mM) SUB concentration (Tab. 3.1). Eqn. 3.1 is a logistic function where μ is the growth rate and t_0 is the midpoint value of the growth.

Once the SUB molecule reaches the active site of BlaC, the first step is the formation of a non-covalent enzyme inhibitor complex (E:I) (Fig. 3.6). The process depends on the free BlaC concentration inside the crystal, and the rate coefficient for non-covalent complex formation (k_{ncov}). This step is usually reversible defined by both the forward rate coefficient (k_1) and the backward rate coefficient (k_{-1}). However, the mounting concentrations of inhibitor inside the crystals forces



more molecules towards the active site. At least initially, the binding rate depends on k_1 alone. The non-covalent E:I complex is the reactant for the next phase of the reaction where the β -lactam ring opens. The resulting covalently bound acyl-enzyme complex (E-I) is so short lived that it never accumulates in the timescale of the measurement. The SUB undergoes rapid modification, and a product is formed where the enzyme is covalently bound to the irreversibly modified inhibitor (E-I^{*}). k_{cov} is the apparent rate coefficient which describes the velocity of E-I^{*} formation directly from the E:I complex. Ligand concentrations were determined by numerically integrating the following rate equations that describe the mechanism in Fig. 3.6.

$$\begin{aligned}
 d[E:I] &= [E_{free}](t_i) \cdot [I](t_i) \cdot k_{ncov} \cdot dt \\
 [E_{free}](t_{i+1}) &= [E_{free}](t_i) - d[E:I] \\
 d[E-I^*] &= [E:I](t_i) \cdot k_{cov} \cdot dt \\
 [E-I^*](t_{i+1}) &= [E-I^*](t_i) + d[E-I^*] \\
 [E:I](t_{i+1}) &= [E:I](t_i) + d[E:I] - d[E-I^*] \\
 t_{i+1} &= t_i + dt
 \end{aligned}$$

3.2

$d[E:I]$ is the change in concentration of the non-covalent BlaC-SUB complex at any given time (t_i) and depends on the free enzyme concentration, $[E_{free}]$, the second order rate coefficient of non-covalent binding (k_{ncov}), and the inhibitor concentration, $[I]$. $[I]$ is calculated from Eqn. 3.1. As the concentration of $[E:I]$ increases, $[E_{free}]$ decreases. $d[E-I^*]$ is the increase of the covalently bound TEN. It depends on the available concentration of the non-covalent BlaC-SUB complex $[E:I]$, and the rate coefficient k_{cov} . $[E:I]$ decreases by the same rate $[E-I^*]$ increases.

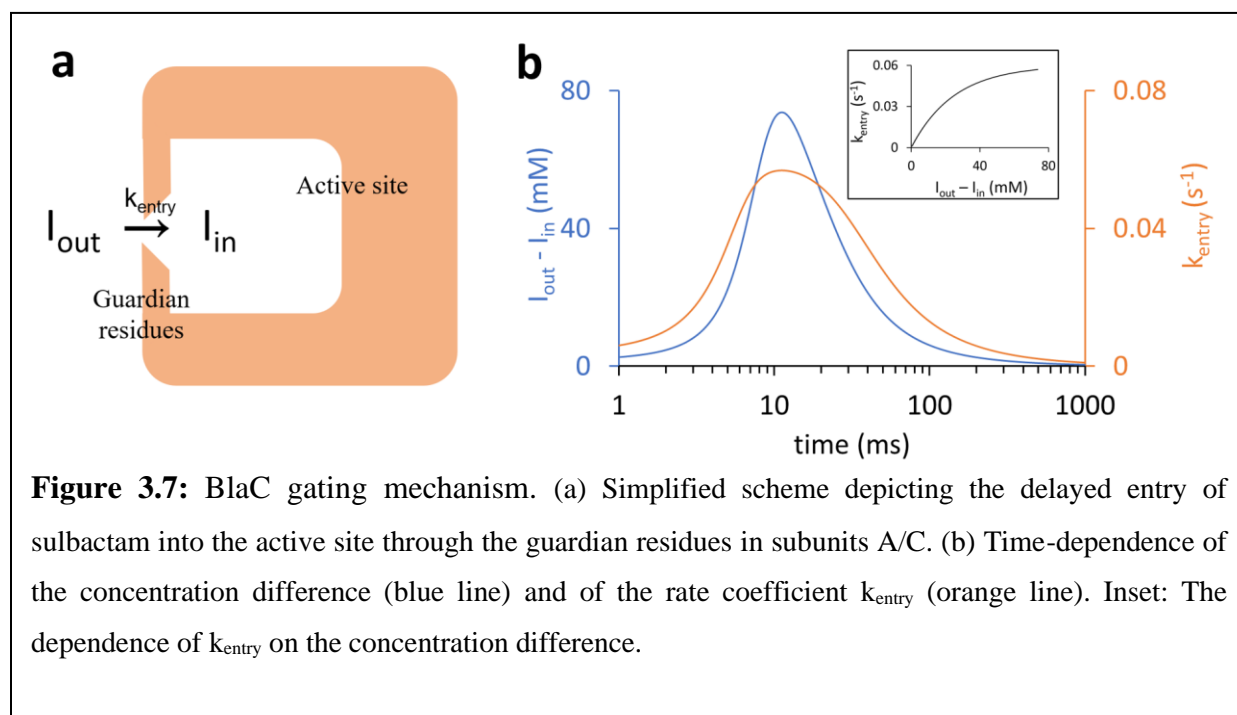


Figure 3.7: BlaC gating mechanism. (a) Simplified scheme depicting the delayed entry of sulbactam into the active site through the guardian residues in subunits A/C. (b) Time-dependence of the concentration difference (blue line) and of the rate coefficient k_{entry} (orange line). Inset: The dependence of k_{entry} on the concentration difference.

The increase of the SUB concentration in the active site of subunits A/C (I_{in}) is delayed relative to that of the SUB concentration in the unit cell (I_{out}) (Fig. 3.7 a). To account for this delay, the rate coefficient that determines the entry into the active site (k_{entry}) is assumed to be dependent on the concentration difference $\Delta I(t) = I_{out}(t) - I_{in}(t)$ between outside and inside the active site and a characteristic concentration difference ΔI_c (Fig. 3.7 b). It is modeled by an exponential function as shown.

$$k_{entry} = k_{max,entry} \left(1 - e^{-\frac{\Delta I(t)}{\Delta I_c}}\right) \quad 3.3$$

The relevant SUB concentrations within the active site (I_{in}) are generated by solving the following rate equation:

$$\begin{aligned} dI_{in} &= k_{entry} \cdot I_{out} \cdot dt \\ I_{in}(t_{i+1}) &= I_{in}(t_i) + dI_{in} \end{aligned} \quad 3.4$$

Eqn. 3.4 is used in lieu of Eqn. 3.3 to calculate the relevant inhibitor concentration. $I_{in}(t)$ is fed as $[I]$ to Eqn. 3.1 to calculate the concentrations of the non-covalently and covalently bound species. At early MISC delays k_{entry} is small. The channel opens, and k_{entry} is large only when sufficient SUB has accumulated in the unit cell (Fig. 3.7 b).

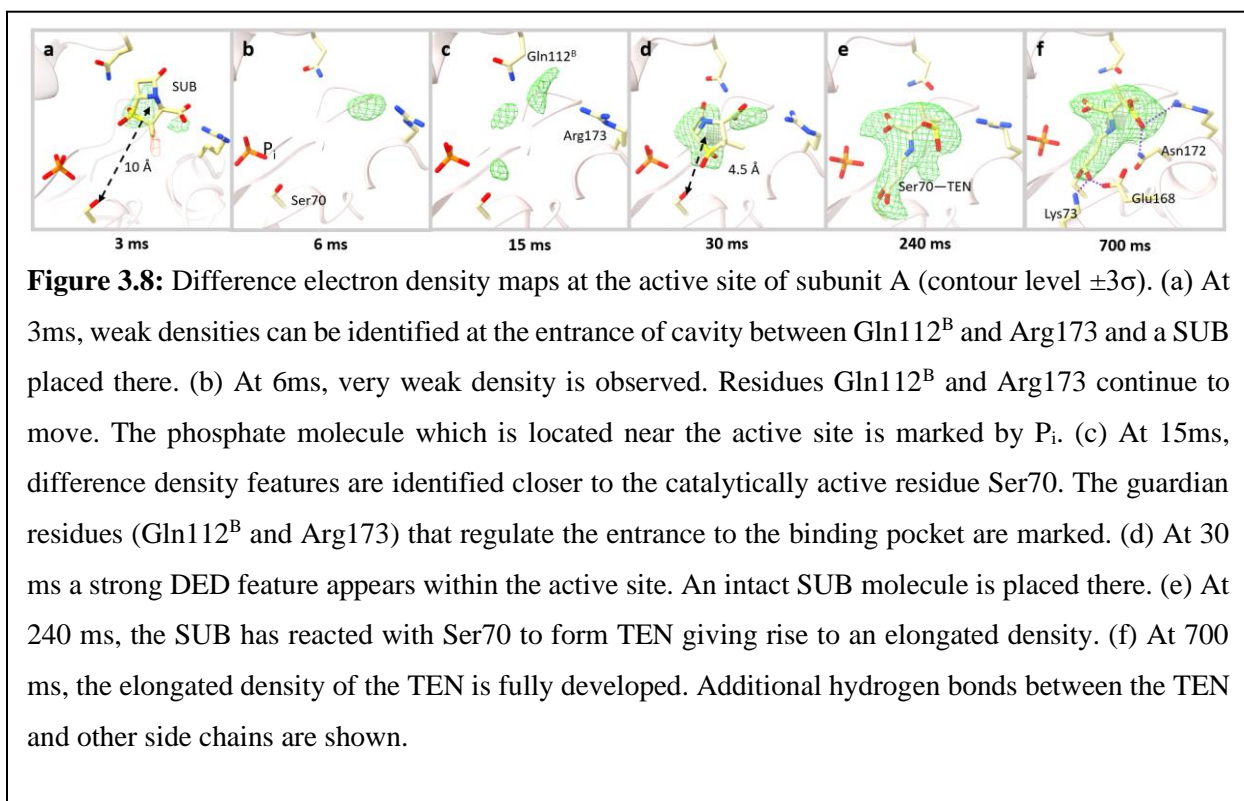
3.3 Results

3.3.1 Binding of sulbactam to BlaC

The subunits A and B display very different structural dynamics with SUB. The binding of inhibitor to subunit C closely resembles that to subunit A, and the kinetics in subunit D is essentially identical to that in subunit B.

The catalytic cleft of subunit A is partially occluded by the neighboring subunit B (Fig. 3.3 b). Particularly the residues Gln109^B and Gln108^B (the superscript B denotes residues from the neighboring subunit B) prevent substrate diffusion from the center of the tetramer, and Gln112^B and Arg173 block access to the active site from the exterior. At 3, 6 and 15ms the difference electron density (DED) features near the active site of subunit A are weak (Fig. 3.8 a-c). But

substantial displacements of the residues like Gln112^B and Arg173 (called here the guardian residues, Fig. 3.3 b) move outward of the active site before relaxing back to original positions (Tab. 3.4). Next to these residues at 3ms, almost 10 Å away from Ser70, there are positive densities that are spatially more spread out than that of water. A SUB molecule is placed in the electron density for visualization (Fig. 3.8 a). The translational and rotational disorder of the free SUB renders the refinement of a single conformation difficult. At 6 and 15ms, density appear closer towards Ser70 (Fig. 3.8 b-c). These could indicate an initial trace of SUB molecules migrating to the active site after being held up by the guardian residues. Up to 15 ms, these densities are too weak for a SUB molecule to be refined with confidence.



At 30 ms, stronger DED features (max $\sigma = 5.5$) appear around 4.5 Å from the catalytically active Ser70 (Fig. 3.8 d). An intact sulbactam can be modelled which reproduces and corroborates the

findings at 66 ms obtained from an earlier experiment (Pandey et al., 2021). The β -lactam ring is oriented away from the Ser70. Between 66 ms and 240 ms, the SUB must have rotated so that the β -lactam ring is positioned towards the Ser70 at which point the nucleophilic attack occurs (Fig. 3.1 a). At 240 ms, the elongated DED feature that originates from the Ser70 directly supports the presence of a covalently bound *trans*-enamine (TEN) (Fig. 3.8 e). The BlaC-TEN adduct structurally relaxes until 700 ms, the final time point in the time series (Fig. 3.8 f). The change in distances between different atoms in the active site during reaction are shown in Tab. 3.4.

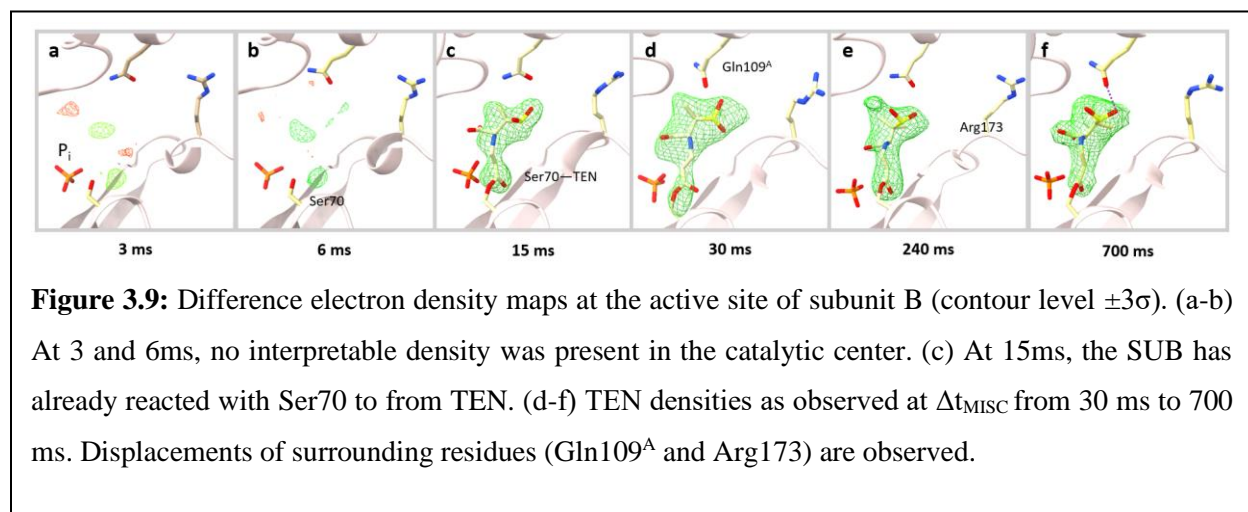
Table 3.4. Important distances (in Å) in the active centers of subunit A and B.

	water	3ms	6ms	15ms	30ms	240ms	700ms
(a) Distance between side chain of some active residues in subunit A							
Ser70 OG to Arg173 CZ	10.9	11.6 (2.7) [†]	12.1 (3.1)	10.7 (1.2)	11.0 (1.6)	10.4 (1.4)	10.2 (1.3)
Ser70 OG to Gln112 ^B CD	10.6	12.0 (2.2)	10.9 (0.4)	10.9 (1.3)	10.6 (0.4)	9.9 (0.5)	9.8 (0.2)
Ser70 OG to Gln109 ^B CD	9.0	10.2	10.0	10.3	10.2	8.6	8.7
(b) Distance between side chains of some active residues in subunit B							
Ser70 OG to Arg173 CZ	13.9	13.2 (2.1)	13.9 (1.7)	14.4 (1.6)	14.8 (0.9)	14.9 (1.5)	14.4 (1.2)
(c) Distances from BlaC side chains to selected SUB and TEN atoms in subunit A							
Thr239 O to SUB O12	-	-	-	-	2.7	-	-
Gln112 ^B NE2 to SUB O8	-	-	-	-	2.7	-	-
Lys73 NZ to TEN O8	-	-	-	-	-	2.5	3.1
Glu168 OE2 to TEN O8	-	-	-	-	-	2.6	2.5
Asn172 ND2 to TEN O12	-	-	-	-	-	2.5	2.9
(d) Distances from BlaC side chains to selected TEN atoms in subunit B							
Thr239 O to TEN O8	-	-	-	2.9	3	3.1	3.2
Gln109 ^A NE2 to TEN O12	-	-	-	3.9	3.4	3.2	4.1

[†]Values in parentheses represent the change in the position [in Å] of the terminal side chain atom from its original position at 0 ms.

^{A,B} subunits that host the amino acid.

In subunit B, there is no concrete evidence of SUB that accumulates in the active site at 3 and 6 ms (Fig. 3.9 a-b). Even the features that appeared near Arg173 in subunits A/C are not present. However, at 15 ms, the presence of strong DED that extends from the Ser70 supports a covalently bound TEN (Fig. 3.9 c). The occupancy refined to 85% in subunit B and 86% in D. This suggests the reaction is close to completion. At later time points, no large changes in the structure of the BlaC-TEN complex are apparent. (Fig. 3.9 d-f).

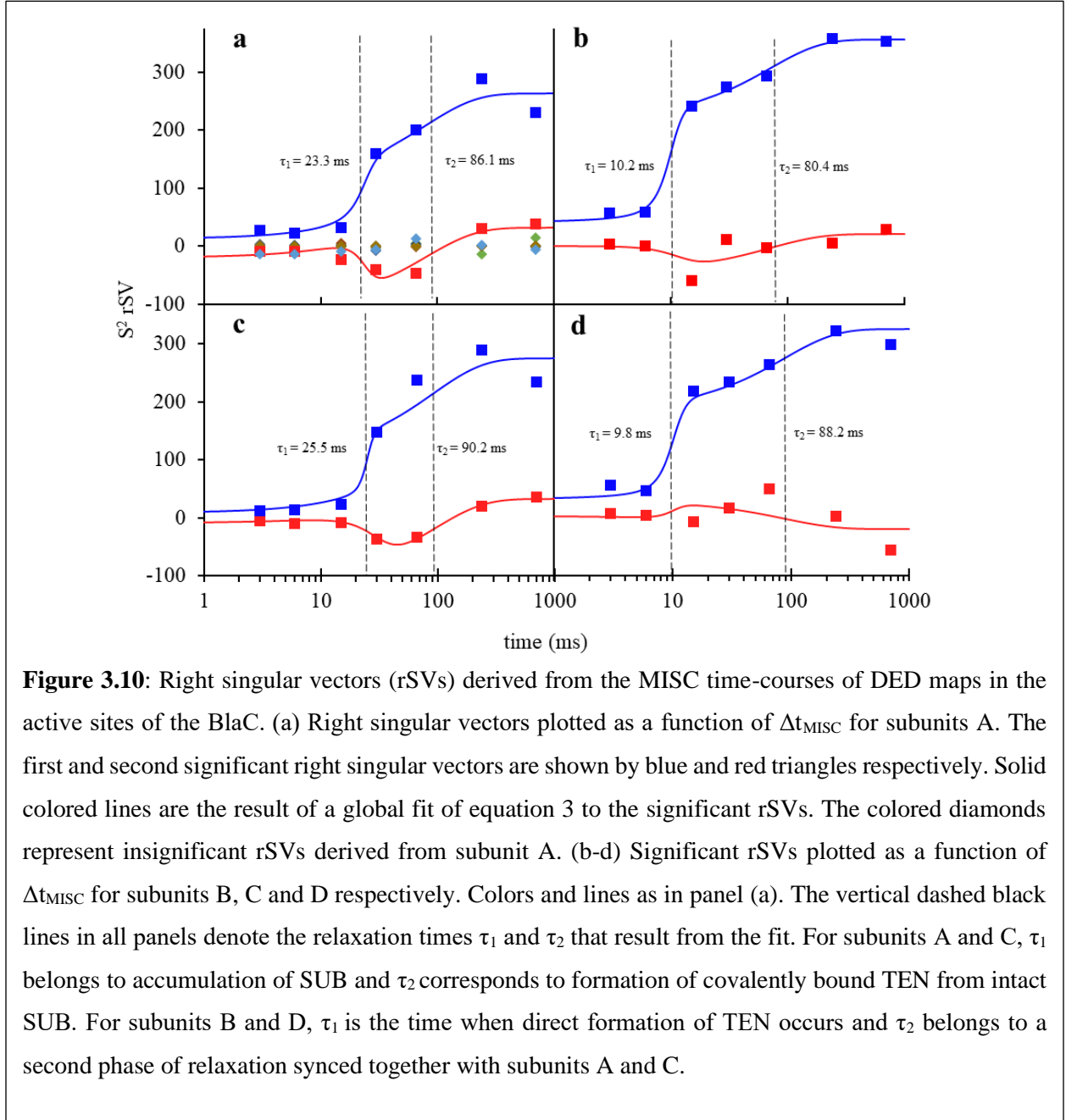


3.3.1 Temporal variation of difference electron density

The SVD analysis of the difference maps yields two significant rSVs are present. They allow for the determination of relaxation times τ_1 and τ_2 by fitting Eqn. 3.5, which, apart from a constant term, consists of a logistics function and a saturation term. Further, the fit was weighted by the square of the corresponding singular values S_i .

$$S_i^2 rSV_i(t) = A_{0,i} + \frac{A_{1,i}}{1 + e^{-\lambda(t-\tau_1)}} + A_{2,i} (1 - e^{-\frac{t}{\tau_2}}) \quad 3.5$$

While the amplitudes $A_{i,s}$ are varied independently for each significant rSV_i ($i = 1 \dots n$), the parameter λ and the relaxation times, τ_1 and τ_2 are shared globally. Detailed values of the parameters of Eqn. 3.5 are shown in the Tab. 3.5. The first two rSVs are shown by blue and squares



in Fig. 3.10. The fitted curves are shown by their respective colored solid line. The rest of the rSVs, shown by colored diamonds in Fig. 3.10 a, are distributed closely around zero and do not contribute to the subsequent analysis.

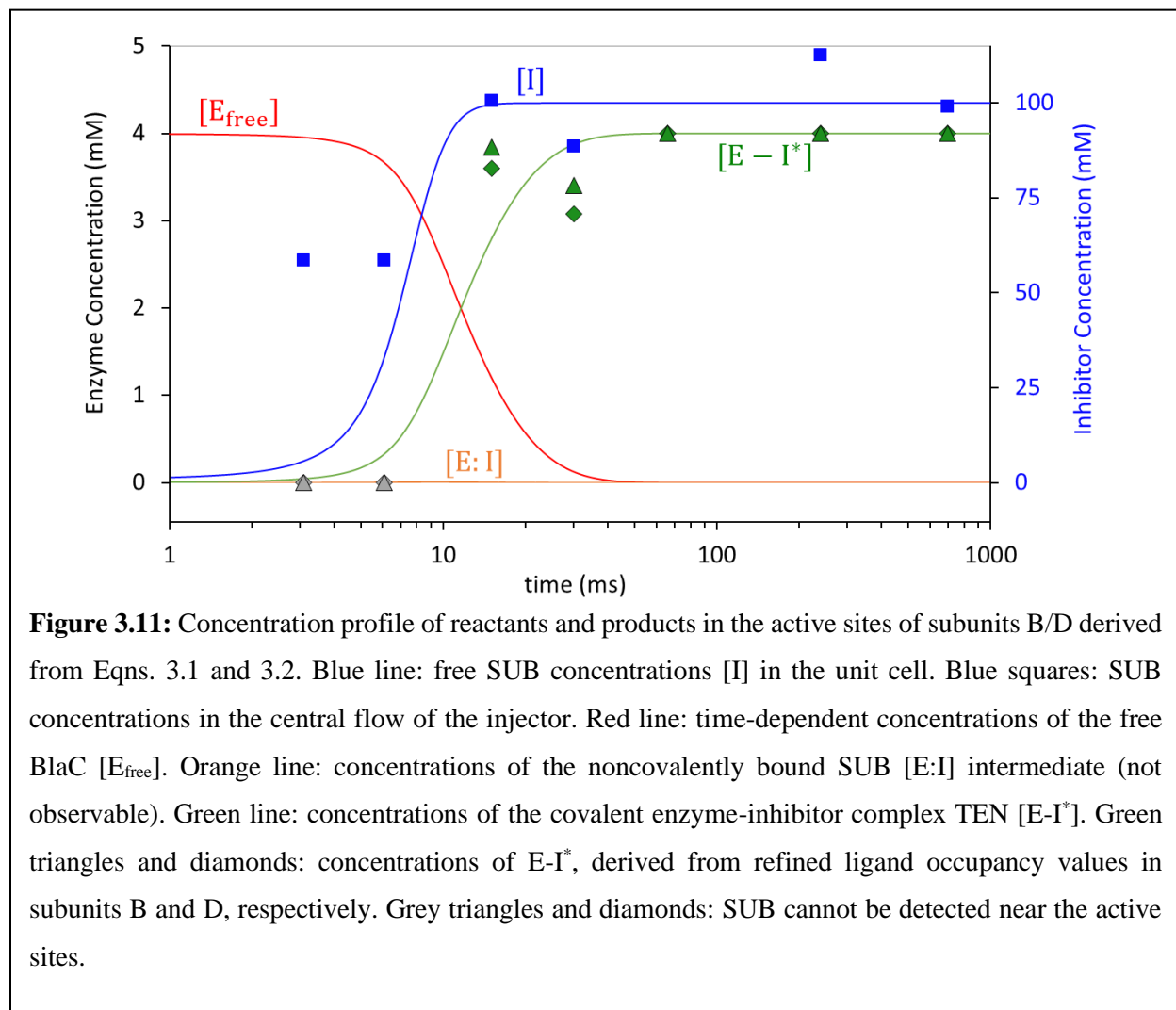
Table 3.5: Relaxation times and amplitudes derived by fitting Eqn. 2 to the significant rSVs.

	Subunit A	Subunit B	Subunit C	Subunit D
λ (ms ⁻¹)	0.25	0.51	0.33	0.69
τ_1 (ms)	23.26	10.17	25.53	9.81
τ_2 (ms)	86.03	80.41	90.01	88.15
rSV₁				
A _{0,1}	11.72	38.32	8.89	32.77
A _{1,1}	118.95	195.44	113.3	155.37
A _{2,1}	134.48	122.15	152.08	137.01
rSV₂				
A _{0,2}	-17.96	-0.25	-12.95	3.23
A _{1,2}	-90.67	-41.79	-74.92	26.54
A _{2,2}	142.88	64.27	117.31	-48.72
λ , τ_1 and τ_2 are global fit parameters for all significant rSVs; the amplitudes A's are determined independently for each rSV.				

The process with relaxation time τ_1 results from the first appearance of DED in the active sites. In subunits A/C, this process reflects the appearance of the non-covalently bound SUB which occurs at around 25 ms (Fig. 3.10 a,c and Tab. 3.5). In subunits B and D, this is associated with the direct formation of a covalently bound TEN which takes place around 10 ms. In subunits A and C, process τ_2 corresponds to the transformation of intact SUB to covalently modified TEN which happens approximately 75 ms and 90 ms respectively after mixing (Fig. 3.10 b,d and Tab. 3.5). However, in subunits B and D, there is no further modification of the ligand once the TEN is

formed (Fig. 3.9). Yet, a second relaxation is observed in subunits B and D coincides with the SUB to TEN formation in subunits A and C.

3.3.3 Characterization of inhibitor diffusion and concentrations of intermediates



The kinetics of SUB binding to subunits B/D is evaluated first, since it allows for an estimate of the ligand concentration in the unit cell that is required to analyze the observations for subunits A/C. The total concentration of BlaC monomers in the crystals (E_{free}) is ~ 16 mM. If only subunit B is considered, the effective $[E_{\text{free}}]$ is 4 mM. The diffusion time of SUB is ~ 7 ms (Fig.

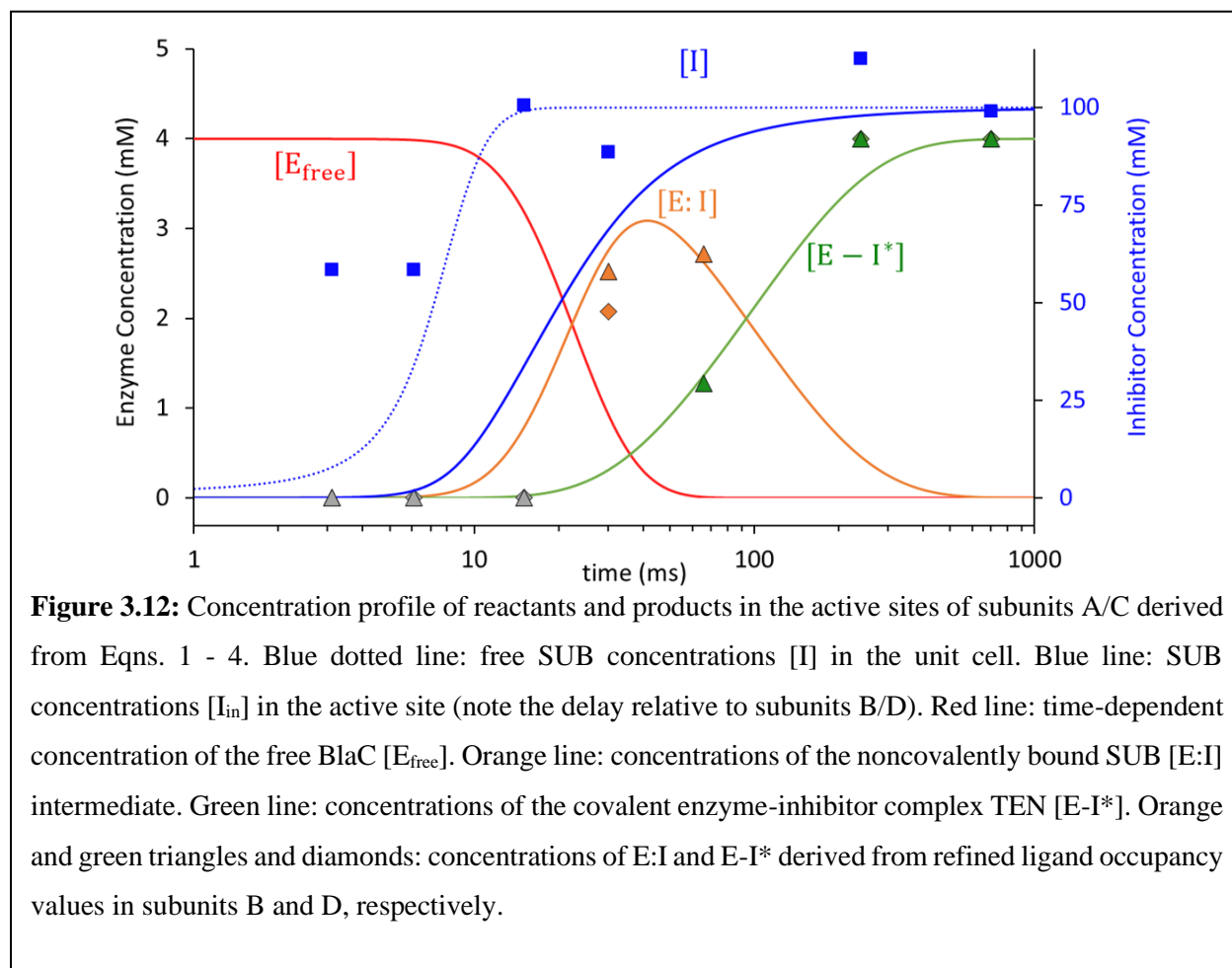
3.11, Tab. 3.6). The diffusion inside crystals is estimated indirectly through the rate equations (Eqns. 3.1 and 3.2) which ultimately must reproduce the observed (refined) ligand occupancies (Pandey et al., 2021). The unknown parameters in these equations must be varied until the concentration of species [E:I] and [E-I*] best match their respective occupancy values (Fig. 3.11). Additionally, the relaxation times derived from the concentration profile would also have to agree with those obtained from SVD analysis of the observed DED maps. The concentrations of the free SUB within the crystals follow approximately the values estimated in the central flow of the injector (Tab. 3.1, compare Fig. 3.11 blue solid line and blue squares).

Table 3.6: Characterization of SUB diffusion and reaction rate coefficients

Parameters to estimate the diffusion of SUB into the unit cells (Eqn. 3).				
μ	0.59 ms ⁻¹			
t_0	7 ms			
Rate coefficients and approximate characteristic times as estimated from the half maximum of the occupancy curves shown in Figs. 5 a and b.				
	Subunits A and C		Subunits B and D	
Rate Coefficients ^a	$k_{\max, \text{entry}} = 0.06 \text{ s}^{-1}; \Delta I_c = 25 \text{ mM}$ $k_{\text{ncov}} = 1.5 \text{ mM}^{-1} \text{ s}^{-1}$ $k_{\text{cov}} = 10 \text{ s}^{-1}$		$k_{\text{ncov}} = 1.5 \text{ mM}^{-1} \text{ s}^{-1}$ (estimated) $k_{\text{cov}} > 8000 \text{ s}^{-1}$	
I_{out}	7 ms	Fig. 5 b blue dotted line	7 ms	Fig. 5 a blue line
I_{in}	20.1 ms	Fig. 5 b blue line	not observed	
E:I formation	21.2 ms	Fig. 5 b orange line	not observed	
E-I* formation	93.4 ms	Fig. 5 b green line	11.5 ms	Fig. 5 a green line
^a from Eqns. 4, 5 and 6.				

The non-covalently bound intermediate that is identified in subunit A/C (Fig. 3.8 d) is not observed in subunits B/D. The covalent binding of SUB can apparently be explained by a one-step

mechanism. However, the two-step mechanism described in Fig. 3.6 is also consistent with the observations. Here, the non-covalent binding of substrate to the enzyme is much slower than the formation of TEN (Tab. 3.6). Accordingly, on the timescale of the observation, a non-covalently bound intermediate cannot be observed. By applying the two-step mechanism, a k_{ncov} value of $\sim 1.5 \text{ mM}^{-1} \text{ s}^{-1}$ and a k_{cov} value of $\sim 8000 \text{ s}^{-1}$ are estimated. The k_{cov} value of 8000 s^{-1} is the minimum value required so that the non-covalently bound E:I complex does not accumulate. A value less than this would give rise to the presence of E:I which is not observed in the DED maps. The characteristic time for the covalent E-I* complex formation is $\tau_{\text{cov}} = 11.5 \text{ ms}$ (Fig. 3.11 green line, Tab. 3.6).



In subunits A/C, the apparent diffusion time of SUB necessary to reproduce the occupancies of the non-covalently bound intermediate is 20 ms (Fig. 3.12, Tab. 3.6). This is much longer than that observed in subunits B/D (7 ms). This lag can only be explained by a restricted (gated) access to the active site. The guardian residues open the active site after about 6 ms which corresponds to about 35 mM outside ligand concentration (Fig. 3.11). Entry to the active site is assumed to be controlled by an additional rate coefficient, k_{entry} (Fig. 3.7 b). k_{entry} is modelled by an exponential function as given in Eqn. 3.3. I_{out} is the SUB concentration in the unit cell, which is known from the substrate binding kinetics to subunits B/D. After a delay of 20 ms, SUB enters the active sites of subunits A/C (Tab. 3.6, Fig. 3.7 b) and I_{in} rapidly increases. 50% occupancy of the non-covalent E:I intermediate is reached at ~21 ms (Fig. 3.12). The accumulation of the non-covalently bound SUB triggers the next step of the reaction where a covalently bound product forms. The concentration of the covalently bound TEN ($[E-I^*]$) starts dominating $[E:I]$ at around 90 ms. By 240 ms, more than 90 % of the active sites are occupied by TEN (Fig. 3.12).

3.4 Discussion

3.4.1 Comparison of kinetics in subunits B/D versus A/C

While all the subunits take part in the reaction despite the heterogeneity, they do so at different rates. In subunits A/C, BlaC is inhibited by SUB via a two-step mechanism. A non-covalent bound species forms (in ~ 25 ms) before the reaction to yield TEN occurs at around 90 ms (Fig. 3.12). An intermediate accumulates, since the SUB is not properly oriented (Fig. 3.8 d) and the reaction can proceed only after an additional time delay. In contrast, in subunits B/D, we notice a one-step mechanism of covalent inhibition. Because the reaction to TEN is much faster (< 1.5 ms) than the diffusion of substrate into the active site (~13 ms) (Tab. 3.6), only the eventual formation of TEN is seen. Any SUB molecule that arrives at the active site instantaneously

converted to TEN on the timescale of observation. The intact SUB intermediate cannot accumulate. Accordingly, the reaction proceeds in a diffusion-controlled manner. In subunits B and D, the k_{ncov} is the rate determining process in the two-step mechanism although the non-covalent complex never accumulates. In a one-step kinetic mechanism, the pseudo one-step rate coefficient would have to be the same as the k_{ncov} , which was confirmed with a separate calculation (not shown). However, the two-step mechanism is presented here for subunit B and D as it explains the enzymology in all the active sites in a consistent manner.

As seen on Fig. 3.3 b, the binding pocket of subunit B is open which allows for the large chemical and structural changes that occur when SUB reacts to TEN. In the active site of subunit A though, any SUB displacements will be limited by interactions with the surrounding residues. This process involves SUB orientating itself into the correct position, the catalytic opening of the β -lactam ring, and the unfurling of the thiazolidine ring, all happening in succession inside the narrow reaction center cavity. This severely lowers the rate of TEN formation.

Overall, the two reaction phases apparent in the SVD analysis have different interpretations for subunits A and C compared to B and D, respectively. For subunits A/C, the first phase corresponds to the non-covalent BlaC-SUB complex formation, and the second to the covalent modification of SUB to form TEN (Figs. 3.10, 3.12). In B and D, the second, slow relaxation phase is also observed (Fig. 3.10 b,d) although the chemical species, TEN, is already established very early on and does not change its configuration further after 30 ms (Figs. 3.6, 3.9). It appears that the second phase is a result of the continuing reaction in subunits A and C and, related to this, ongoing relaxations of the entire protein structure connected to subsequent TEN structural relaxations in subunits B and D. Since the second phase relaxation rates (Tab. 3.5) are similar in all subunits, it seems as if all

subunits relax in synchronized manner which is an indication for a cooperative behavior of all four subunits. This observation which would have been obscured by the visual analysis of the DED maps alone. It is only possible with the SVD analysis which can track DED values in all voxels of the ROI across the entire reaction with great precision.

3.4.2 Rapid diffusion and binding of sulbactam in BlaC microcrystals

The volume of SUB enclosed by van der Waal's surface (181.7 \AA^3) is 2.5 times smaller than that of CEF (444.9 \AA^3). Due to the smaller size, SUB is expected diffuse faster into the crystals than CEF. For CEF, 50% occupancy of the enzyme substrate complex has been observed at $\Delta t_{\text{MISC}} = 5\text{ms}$ in subunits B and D (Pandey et al., 2021). For the smaller SUB, the evidence of the enzyme inhibitor complex is expected to appear already in the DED maps at earliest time points (3 ms and 6 ms). However, the earliest event that could be identified in the DED maps is the appearance of the TEN at $\Delta t_{\text{MISC}} = 15\text{ms}$ in subunits B and D. The concentrations of SUB at the active site of subunits B and D (Fig. 3.11), which allow direct, unrestricted access, can be taken as an estimate of the SUB concentration inside the BlaC crystals. The lag between the estimated SUB concentration in the inner flow of the injector constriction and the concentrations in the crystals at early time points (Fig. 3.11, compare blue squares with the blue line) is expected, since diffusion in BlaC crystals is slowed down in crystals (Pandey et al., 2021) compared to water. The diffusion time (7ms) of the SUB is almost the same as that for the antibiotic substrate CEF ($\sim 5\text{ms}$) (Pandey et al., 2021). Still, contrary to expectations based on the size of the SUB, no electron density has been present at the earliest time points. This can be explained by the smaller second order binding coefficient, k_{ncov} , which is $1.5 \text{ mM}^{-1} \text{ s}^{-1}$ compared to $3.2 \text{ mM}^{-1} \text{ s}^{-1}$ for CEF.

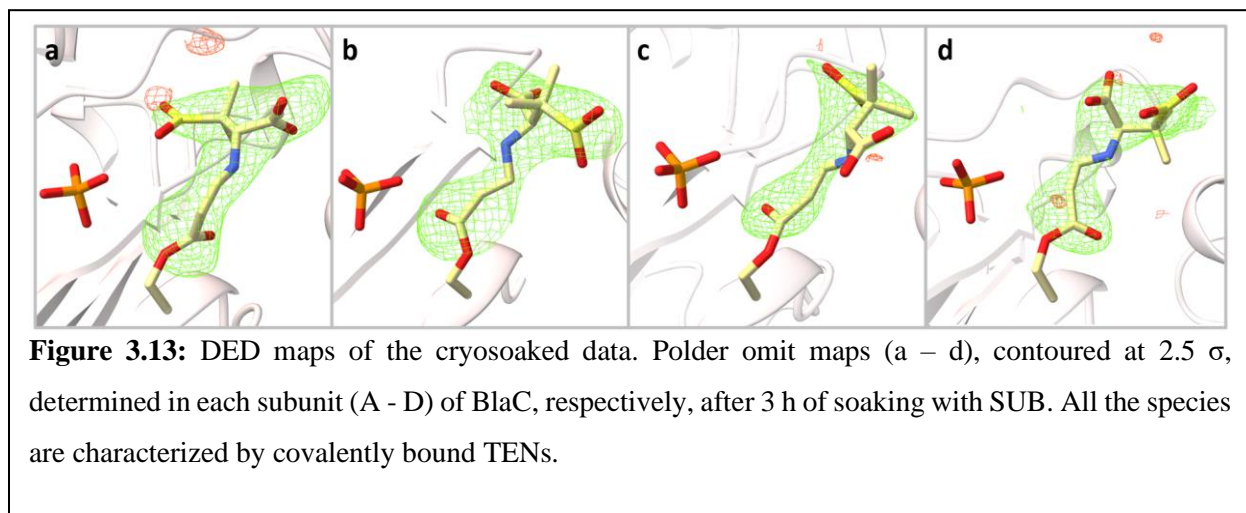
The characteristic time for sulbactam forming a covalent bond with Ser70 in subunits B and D is around 10 ms (Fig. 3.10). This time is quite fast in comparison to earlier works suggesting that the reaction might take minutes to complete (Tassoni et al., 2019; Totir et al., 2007). This fast reaction provides an advantage when β -lactam substrates and the SUB inhibitor are competing for the same active site. For example, the non-covalent enzyme-substrate complex with CEF persists for up to 500 ms (Olmos et al., 2018). During this time, the CEF can leave the enzyme and be replaced first competitively and then irreversibly by a quickly reacting SUB molecule. Since the inhibitor competes with co-administered antibiotics for the active site of BlaC, one can imagine that the covalent bond formation with an inhibitor must occur as fast as possible to effectively eliminate β -lactamase activity in the presence of substrate. This is in addition corroborated by Jones and coworkers who reported that SUB has a ten times higher affinity and binding constant for plasmid mediated class A β -lactamases compared to cefoperazone (Jones et al., 1985), which is a third-generation cephalosporin-based antibiotic similar to CEF.

3.4.4 The fate of the *trans*-enamine

Trans-enamines were observed in all four subunits when BlaC was soaked with SUB for 3 hours (Fig. 3.13). It has been proposed that on longer timescales (> 30 min), a second nucleophilic attack by a nearby serine (Ser130) can occur in other, structurally closely related Ambler Class A β -lactamases (Drawz & Bonomo, 2010). This serine (Ser128 in BlaC) may react with the C5 position of the *trans*-enamine (Fig. 3.1 d). This is followed by the loss of the opened thiazolidine ring fragment. A covalent bond may be formed between C5 and Ser128 of BlaC leading to the prolonged inhibition of the enzyme (Drawz & Bonomo, 2010; Totir et al., 2007). Fig. 3.14 a shows the proposed structure of the cross-linked species. It has been suggested that only the transient inhibition by *trans*-enamine is responsible for the medical relevance of SUB as any reaction that

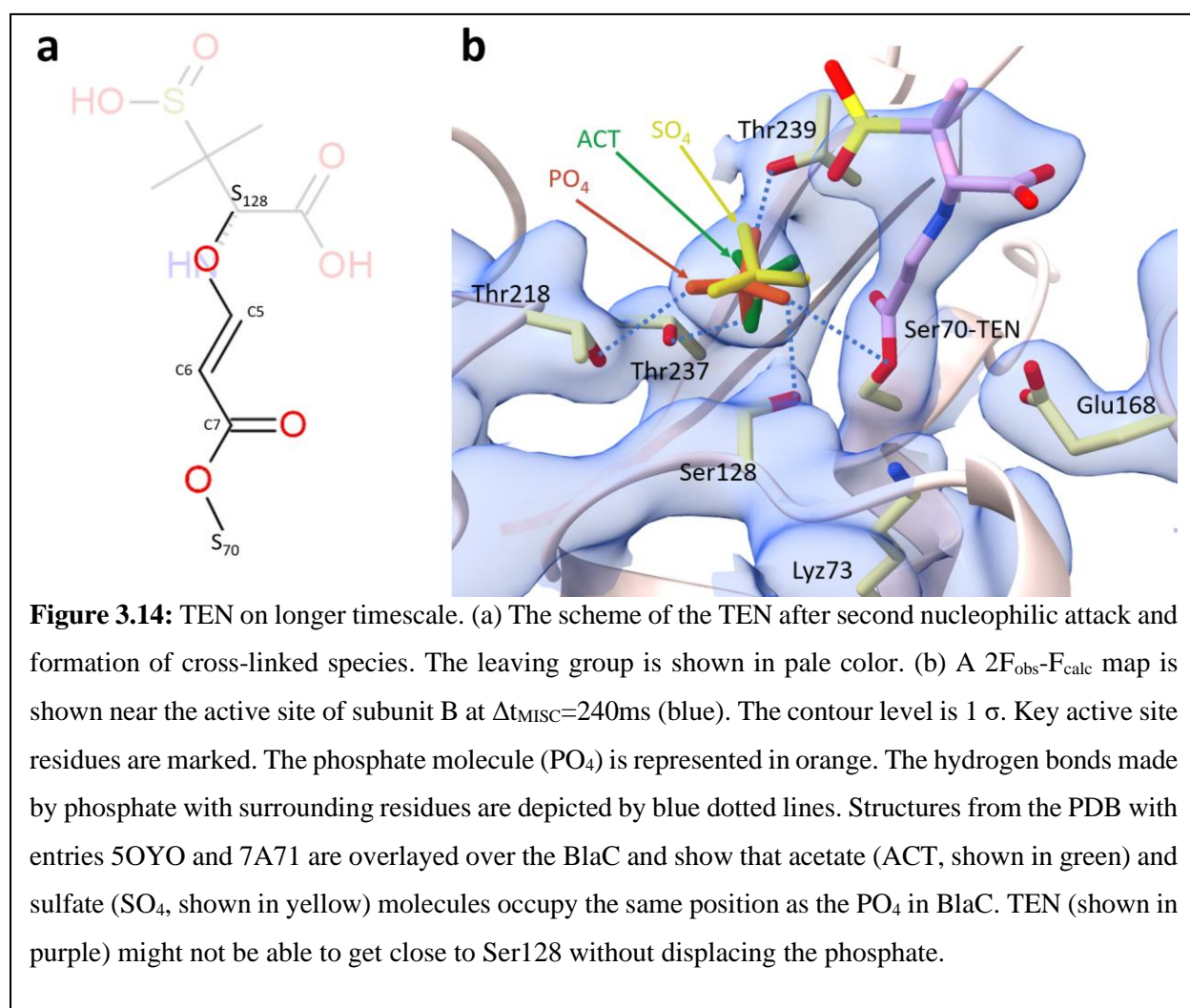
lasts longer than one hour is irrelevant due to the bacterial lifecycle of ~30 minutes (Totir et al., 2007). However, the life cycle of *Mtb* is around ~20 hours (Murray et al., 2020). The permanent inhibition achieved only after the second nucleophilic attack might be the ultimate factor for clinical usefulness of SUB in fighting antibiotic resistance in slow growing bacteria like *Mtb*. Inspection of the cryo-structure after soaking with SUB (Fig. 3.11) might give an answer.

The B-factors of the fragment beyond N4 that would be cleaved off (displayed in pale colors in Fig. 3.14 a) are consistently higher by 20 Å² than that of the part which would form the cross-linked species. In our opinion it is more likely that this is caused by the dynamic disorder of the long TEN tail and not by the presence of mixture of intact and fragmented TEN. Summarizing, on the timescale of 3 h there is no clear evidence of TEN fragmentation. TEN remains the physiologically important factor for BlaC inhibition on this time scale.



A phosphate group binds to a specific site immediately adjacent to the active serins 70 and 128 (Fig. 3.14 b) with multiple hydrogen bonds to surrounding residues. This location appears to be conserved among all published BlaC structures where others have also reported sulfate and acetate molecules in the same position (Fig. 10 b) (Elings et al., 2017; Feiler et al., 2013; Tassoni et al.,

2019; Yang et al., 2000). Naturally occurring compounds with phosphate like group, for instance adenosine phosphates, may also interact with BlaC. Another study reported an increase in β -lactamase production in some bacteria grown in a phosphate enriched medium (Ileri et al., 2007) while another has concluded that phosphate can promote the hydrolysis of the clavulanate inhibitor by BlaC (Elings et al., 2017). The physiological relevance of phosphate binding cannot be completely ignored.



It is not clear whether the phosphate prohibits the TEN from getting closer to Ser128, and how much time, if any, is required for a prospective reaction to proceed. More structures are required

after soaking with high SUB concentrations for longer periods of time, perhaps days, to separate potential admixtures of intact and fragmented TEN made possible using SVD based methods (Schmidt et al., 2003). Since the phosphate is replaceable, as was observed during the binding of the large CEF molecule (Olmos et al., 2018; Pandey et al., 2021), the TEN might indeed react further. Larger inhibitors like tazobactam and clavulanic acid might also be able to displace the phosphate molecule directly already during the initial binding phase, and thereby naturally allowing the second nucleophilic attack by the close-by serine to occur.

3.5 Outlook

MISC is a straightforward way to structurally study enzyme catalysis and inhibition. Reactions are visualized in real time as movies of the enzyme in action. Our results give insight how the shape of the active site determines rate coefficients and reaction mechanisms of a biomedically relevant, enzymatically catalyzed reaction. There are other classes of β -lactamases that are more concerning than BlaC such as the metallo β -lactamases (MBL). They are capable of hydrolyzing almost all clinically available β -lactam antibiotics and inhibitors (Boyd et al., 2020; Palzkill, 2013). Similar work to the one presented here and earlier (Olmos et al., 2018; Pandey et al., 2021) should be performed on MBLs to gain more structural insight into their catalytic mechanisms. Time-resolved pump-probe crystallographic experiments using a caged Zn molecule (Joachimiak et al., 2022) already show how the antibiotic moxalactam is inactivated by a MBL on a timescale longer than 20 ms. To characterize the all-important substrate binding phase on single ms, and even sub-ms time scales, it would be desirable to follow this or a similar reaction as well as the binding of a MBL inhibitor with MISC.

4. Phytochrome

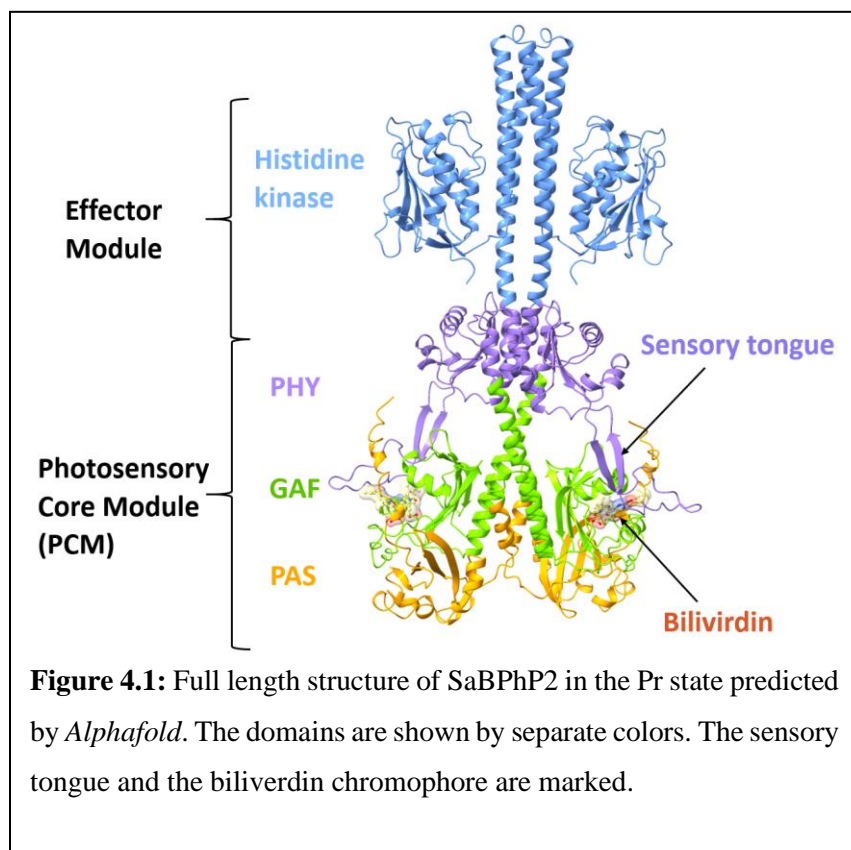
Both crystallography and cryo-EM experiments have been performed during this project. At the time of this writing, the manuscript reporting the crystallographic work done on this protein is under preparation for submission to *Proceedings of the National Academy of Science (PNAS)* journal. In this project, I have been involved in protein purification and crystallization, data collection, and data analysis. The cryo-EM investigation is an ongoing project. Preliminary results are presented in this dissertation.

4.1 Introduction

Phytochromes are red light photoreceptors found in plants, fungi, and bacteria (Nagatani, 2010). They regulate essential physiological process in plants like seed germination, shadow avoidance, synthesis of chlorophyll, etc (Burgie et al., 2014; Smith, 2000). While there have been extensive studies about the structure and function of plant phytochromes, their role in non-photosynthetic bacteria remains largely unknown (Woitowich et al., 2018). It is believed that bacteriophytochromes (BphPs) are used by bacteria to sense the environment they are in and elicit proper cellular response. They may gather information about the type and concentration of bilins, assess redox status, and gauge the availability and wavelength of light (Auldrige & Forest, 2011). The phytochrome studied in this project is derived from myxobacterium *Stigmatella aurantiaca*. Myxobacteria are distinguished among prokaryotes by a multicellular stage in their life cycle known as fruiting bodies. In *S. aurantiaca* the formation of fruiting bodies is controlled by the light. Interestingly, *S. aurantiaca* contains two phytochromes of which phytochrome 2 (SaBphP2 for *S. aurantiaca* bacteriophytochrome protein 2) is investigated here.

Phytochromes are one of the largest light-regulated enzymes. They are composed of multiple modules and sub domains. A typical bacteriophytochrome consists of a photosensory core module (PCM) and an effector module with enzymatic activity (Fig. 4.1). The PCM further consists of three domains: PAS (Per-Arndt-Sim, orange section), GAF (cGMP phosphodiesterase/adenylyl cyclase/FhIA, green section), and PHY (phytochrome-specific GAF-related, magenta section) as shown in Fig. 4.1. The effector module is covalently bound to the PHY domain and differs among species (Kojadinovic et al., 2008; Otero et al., 2016). In SaBphP2, the effector module consists of a histidine kinase (HK) whose activity is light regulated.

The structure of the full length SaBphP2 has remained unknown so far. Recently the *AlphaFold* software became available which uses artificial intelligence (AI) and machine learning (ML) to predict structures of protein directly from sequence data (Jumper et al., 2021). Fig. 4.1 shows the prediction



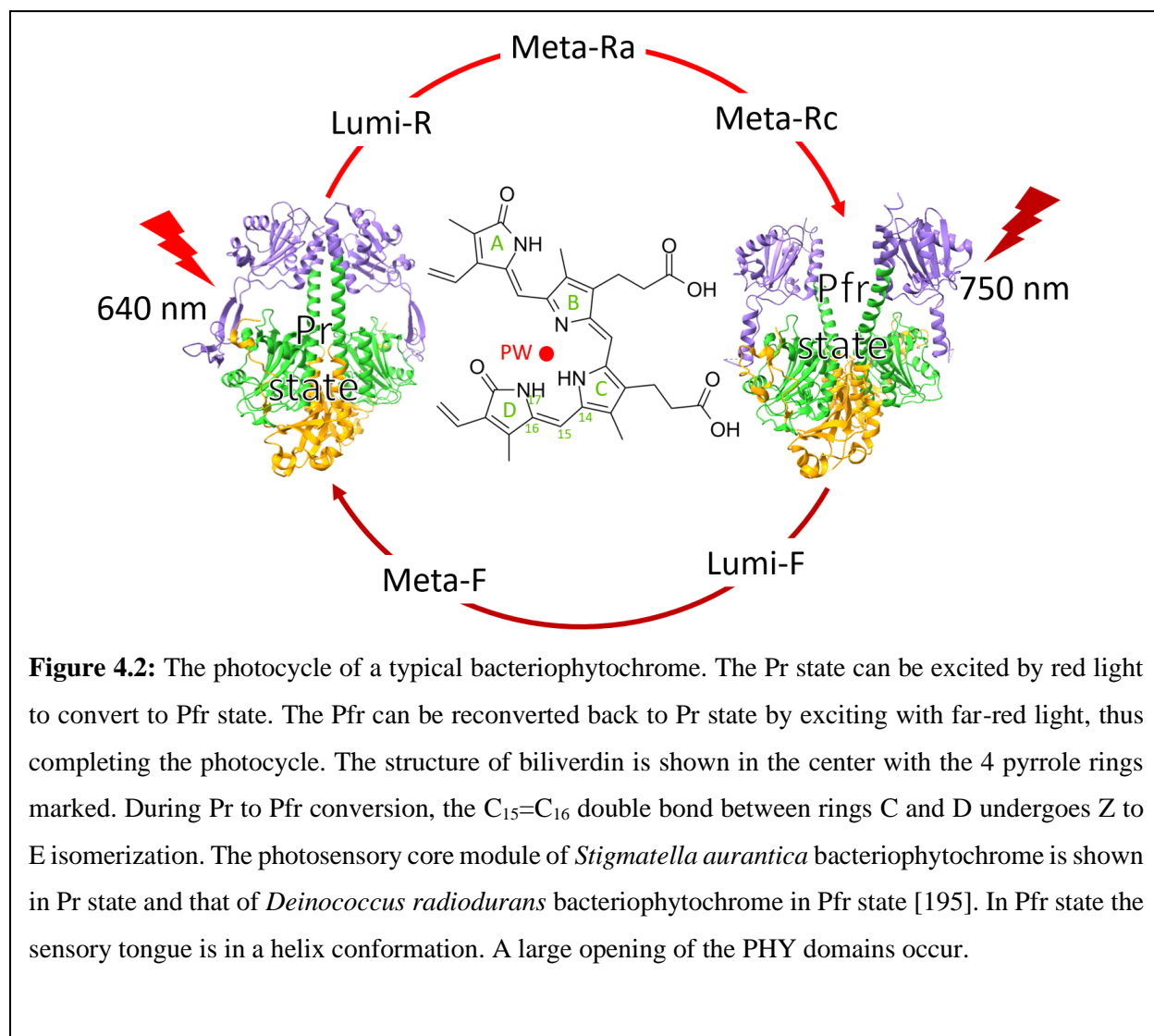
of the full length SaBphP2 made by *AlphaFold*. The PHY domain has a tongue-like extension which contacts the GAF domain to seal the chromophore pocket. The central chromophore is biliverdin (BV) in the case of bacterial phytochromes. BV is a heme-derived, open-chain

tetrapyrrole (pyrrole rings A–D in Fig. 4.2). The sensory tongue probes the configuration of the BV and transmits the signal to the HK (shown by blue) through the PHY domain.

Phytochromes interconvert between a dark red-light absorbing state, Pr and a photoactivated far red-light absorbing state, Pfr through several intermediates (Auldridge & Forest, 2011). At Pr state, upon illumination with red light ($\lambda = 640$ nm), the BV undergoes Z to E isomerization about the C₁₅=C₁₆ double bond between the pyrrole rings C and D (Fig. 4.2). Ring D rotates by 180° which is the Lumi-R state) driving the phytochrome into the first half of the photocycle (Fig 4.2). During this time, a conserved water molecule called the pyrrole water (PW) is also photo-ejected which rebinds back to BV in Pfr state (Carrillo et al., 2021; Claesson et al., 2020). Following successive deprotonation and reprotonation events in the Meta states, the phytochrome reaches the Pfr state (Auldridge & Forest, 2011). The consensus is that the structures of the Pr and Pfr states differ significantly. In Pr state, the tongue assumes a β -strand conformation, whereas, in the Pfr state, it assumes α -helix conformation (Burgie et al., 2016; Takala et al., 2014). It coincides with the large scale opening of the PHY domain. The Pfr state can be driven back to Pr state by illumination of far-red light ($\lambda = 740$ nm) completing the photocycle.

The crystallographic full-length structure of SaBPhP2 is unknown. HK is connected to PHY domain by a single coiled linker (Fig. 4.1) which makes the whole domain rather flexible. Flexible proteins are harder to crystallize. However, the truncated proteins which consist of only PCM or even shorter construct with only the PAS and the GAF domains crystallize and diffract to high resolutions (Claesson et al., 2020; Sanchez et al., 2019). Accordingly, we use the truncated protein for crystallographic studies. Previously, TR-SFX experiment was performed on the SaBphP2 PCM at beamline 2 (BL2) at Spring-8 Ångstrom Compact X-ray Laser (SACLA). The microcrystals

were excited by 5 ns short light pulses and probed by X-ray pulses at ambient pressure. These experiments showed a complete ring-D isomerization and the associated structural changes in transient intermediates observed at 5 ns and 33 ms after excitation (Carrillo et al., 2021).



To explore earlier events, excitations by shorter laser pulses are required. The TR-SFX were performed at LCLS using ultrashort (100 fs) laser light pulses for photoexcitation. This dissertation shows the results of the early stages of the Pr to Pfr transition at picosecond time scales. The TRX studies on PCM provide plethora information on the mechanism of photo-excitation and the

structural changes that follows. The propagation of signal from chromophore towards the HK domain on the top can be traced (Carrillo et al., 2021). A complete understanding of the phytochrome mechanism, however, requires the structure of full length phytochrome. Proteins that are difficult to crystallize can be investigated with cryo-EM. Here, preliminary results from attempts to determine a structure of the full length, intact SaBphP2 by cryo-EM are also presented.

4.2 Methods

4.2.1 Protein purification and crystallization

Both, the full length, intact SaBphP2 and a shorter fragment that covers the SaBphP2-PCM were expressed in *E. coli*. The expression protocol is identical for both products. Cells were grown at 37° C to a OD₆₀₀ value of 0.6 followed by induction with 1 mM IPTG and addition of 0.5 mM δ -aminolaevulinic acid (DAC) overnight. Cells were recovered in 150 mM NaCl, 20 mM Tris-HCl, pH 8.0 and 15% v/v glycerol with protease inhibitor. Lysis was performed with pulse sonication on ice bath. The insoluble cell debris was removed by highspeed centrifugation, and the supernatant was incubated with 200 μ M BV in Dimethyl sulfoxide (DMSO) in the ratio 1:100 for 30 min at 4°C. The solution was applied to Talon Co⁺² metal ion affinity chromatography column. The column was washed with high salt buffer (20 mM Tris-HCl, 1 M NaCl, pH 8.0) followed by low salt buffer (20 mM Tris-HCl, 1 M NaCl, pH 8.0) with 20 column volumes each. The protein was eluted by 300 mM imidazole, 20 mM NaCl, 20 mM Tris-HCl, pH 8.0. After elution the protein was immediately transferred into stabilizing buffer containing 20 mM NaCl, 20 mM Tris-HCl, pH 8.0.

SaBphP2 PCM single crystals were obtained by the hanging drop vapor diffusion method in dark conditions at 16 °C with a protein concentration of 30 mg/ml. The mother liquor consists of 0.17

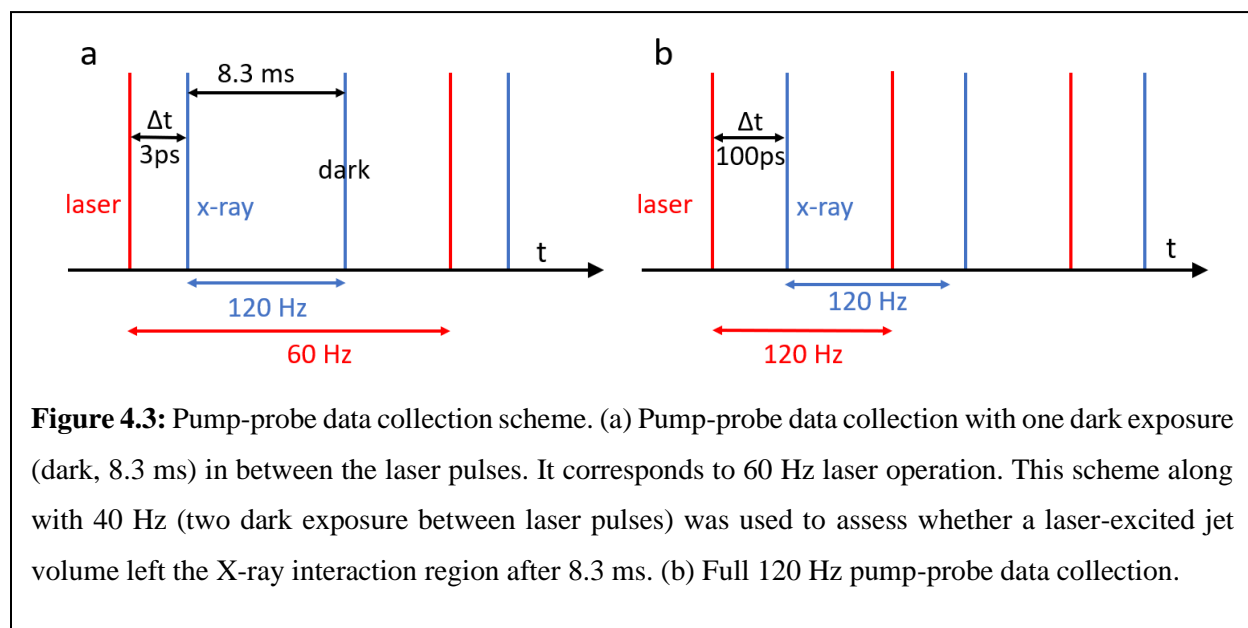
M ammonium acetate, 0.085 M sodium citrate tribasic dihydrate, 25.5% w/v Polyethylene glycol (PEG) 4000 at pH 5.6 mixed with 20% w/v benzamidine hydrochloride in the ratio 85:15. Microcrystals were grown by mixing 3-part protein (concentrated to 60 mg/ml) to 2-part mother liquor described above and seeding with crushed macroscopic crystals. All the crystallization steps were carried out in dark or under green safety light.

4.2.2 TR-SFX data collection

X-ray data were collected from SaBPhP2 PCM microcrystals at the coherent X-ray imaging (CXI) instrument (Liang et al., 2015) and the macromolecular femtosecond X-ray crystallography (MFX) instrument (Boutet et al., 2016) at LCLS. At CXI, the experiment is performed at vacuum environment while at MFX, the experiment is performed in helium at ambient pressure. The lipidic cubic phase (LCP) injector developed by Weierstall and colleagues (Weierstall et al., 2014) was used for sample delivery. The LCP injector requires that the microcrystals are embedded in viscous media. For that, 50 μ l of dense crystal slurry was folded into 450 μ l of nuclear grade grease. The mixture is carefully transferred to the reservoir of the LCP injector so as not to introduce any air gaps. The injector extrudes the viscous mixture through a 75 μ m nozzle orifice to the X-ray interaction region 60 μ m downstream of the nozzle exit. Helium gas is flown concentrically around the nozzle to keep the extrusion as straight as possible. The reaction in the microcrystals was initiated with 100 fs optical laser pulses of wavelength 640 nm. The full width at half maximum (FWHM) of the laser light intensity distribution at the sample was 80 μ m at CXI and 64 μ m at MFX.

The reference data (without light excitation) was collected with sample flow rate of 1 μ l/min. For pump-probe data the jet flow rate was increased to 3 μ l/min to transport the region of the jet that

was already excited away from the X-ray interaction region for the next probe pulse. The laser excitation rate was set at 3 different values (40 Hz, 60 Hz and 120 Hz). In 40 Hz collection scheme, there are two extra dark exposures before another pump-probe sequence begins. Similarly, one dark exposure in 60 Hz mode and no dark exposures in 120 Hz. This allows to assess by a direct measurement whether an once laser excited jet volume has left the X-ray interaction region, or whether contaminations prevail that are either mix-ins or are excited a 2nd time by the next laser pulse. A 3ps pump-probe dataset was collected at MFX with 60 Hz laser repetition rate (Fig. 4.3 a) and a 100 ps dataset at CXI with full 120 Hz laser repetition rate (Fig. 4.3 b).



The DPs were recorded with the Jungfrau detector at CXI and with the ePix10k 2M at MFX. The experiment was monitored in real time with *OM* (Mariani et al., 2016). Hit-finding was performed with *Cheetah* (Barty et al., 2014). Indexing and integration was achieved by *CrystFEL* (White et al., 2012). The data collection statistics are given in Tab. 4.1.

Table 4.1: SFX data collection statistics for phytochrome

Pump-probe time delay	dark	3 ps	dark	100 ps
Instrument	MFX		CXI	
Temperature [K]	293			
Detector	epix10K 2M		Jungfrau	
Jet Flow Rate [$\mu\text{l}/\text{min}$]	1	3	1	3
Nozzle diameter	75 μm	75 μm	75 μm	75 μm
Pump laser wavelength	-	700 nm	-	640 nm
Laser spot size (FWHM)	-	64	-	80
Laser Fluence [mJ/mm^2]	-	10	-	10
Laser repetition	-	60 Hz	-	120 Hz
Crystal Size	20 – 30 μm			
Hits	389,512	336,702	181,191	179,480
Indexed	132,305	154,268	80,501	63,642
Observed reflections	66,172	50,738	89,736	66,578
Unique reflections	8,822	7,248	12,819	10,567
Resolution \AA	2.15	2.2	1.95	2.1
R-split	12.1 (95)	8.28 (211.4)	7.7 (209.3)	9.5(208)
$\text{CC}_{1/2}$	98.7 (37)	99.2(16)	99.7 (12)	99.5(21)

4.2.3 TR-SFX difference maps and structure determination

Difference maps were calculated as reported in detail in section 2.6. To obtain a structural model, an EED_{map} for each time point was calculated (section 2.6.4). N_c is on the order of 20, which indicates a population transfer of $\sim 10\%$. Models were placed into the EED maps in *cool* and the positions of the chromophore and nearby residues were real-space refined against the EED map. Ligand restraints for BV were weakened to allow for a non-conventional, strained geometry of the highly excited chromophore at early times. After the real-space refinement, the validity of the solution was tested by comparing the observed DED_{obs} with calculated DED_{calc} on BV ring-D using the Pearson correlation factor (Carrillo et al., 2021). The DED_{calc} were obtained from

difference structure factors calculated by subtracting the reference ($F_{\text{calc(ref)}}$) from structure factors of the refined models at pump-probe delay ($F_{\text{calc}}(\Delta t)$).

4.2.4 Cryo-EM data collection

Cryo-EM experiments on full length phytochrome data were performed by our collaborators at the Simons Electron Microscopy Center (SEMC) of the New York Structural Biology Center (NYSBC) consortium. For more information on the services and different equipment available at SEMC visit <https://nysbc.org/semc-dept/semc-department>. For the experiment, the purified protein is frozen at -80°C and shipped to SEMC on dry ice. Before the cryo-EM experiments were conducted, the sample was warmed up to room temperature and manipulated under ambient light. The feasibility of the protein sample for the cryo-EM study was confirmed with negative staining as described in section 2.8.1. To prepare cryo-EM grids for imaging, 3 μl of 4 mg/ml protein was applied to glow-discharged holey carbon EM grids (Quantifoil 300 copper mesh, R1.2/1.3) in an EM-GP2 plunge freezer (Leica). Sample-coated grids were blotted for 3 to 5 seconds before plunge-freezing into liquid ethane and stored in liquid nitrogen for data collection. Movies were collected with an EF-Krios microscope (Thermo Scientific) and detected on a GatanK3 imaging system (Gatan, Inc.) with an effective pixel size of 0.8443 \AA . The GatanK3 is an extremely sensitive direct detection camera that can count single electrons in real-time. The microscope was operated at an acceleration voltage of 300 kV and nominal magnification of 105,000x. Movies were collected at a dose rate of 41.89 $\text{e}^{-}/\text{\AA}^2/\text{s}$ with a total exposure of 1.6 s, for an accumulated dose of 67.02 $\text{e}^{-}/\text{\AA}^2$. Intermediate frames were recorded every 0.04s for a total of 40 frames per movie. A total of 17889 movies were collected with a defocus range of 0.8 – 2.5 μm . The movies were transferred to UWM for in-house processing.

Table 4.2: Cryo-EM data collection and refinement statistics

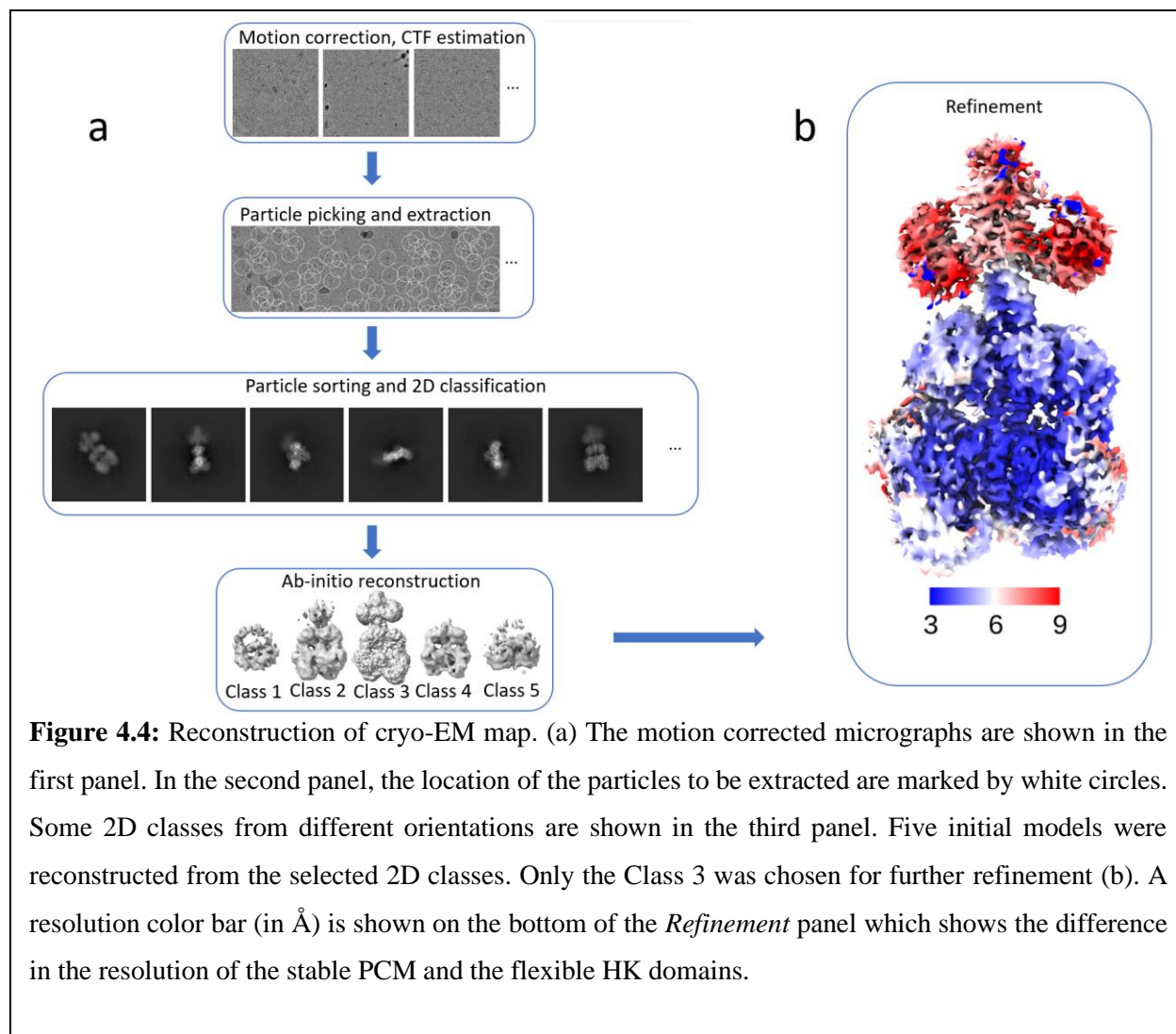
Collection statistics	
Magnification	105,000
Voltage (kV)	300
Electron exposure (e-/Å ²)	67.02
Defocus range (µm)	0.8-2.5
Pixel size (Å)	0.8443
Symmetry imposed	none
Initial particle images (no.)	1,520,224
Final particle images (no.)	865,248
Map resolution (Å)	3.75
FSC threshold	0.143
Refinement statistics	
Refinement resolution (Å)	3.8
Map sharpening <i>B</i> factor (Å ²)	153.9
Model Composition	
Protein residues	1492
Ligands	2
B factors (Å ²)	
Protein	270.99
Ligand	188.42
RMS deviations	
Bond lengths (Å)	0.004
Bond angles (°)	0.872
Validation	
MolProbity score	2.39
Clash score	18.21
Ramachandran plot	
Favored (%)	82.53
Allowed (%)	14.86

4.2.5 Cryo-EM map reconstruction and structure determination

Cryo-EM data were processed using *cryoSPARC* (v4.2.1) with default parameters unless noted. A simple workflow is shown in Fig. 4.4. The 17,889 raw movies were pre-processed with *Patch motion correction* and *Patch CTF estimation* jobs. The resulting micrographs were subjected to exposure curation from which 13,321 exposures were selected. The rest with poor CTF fits and large full-frame motions were eliminated. The full-length *Alphafold* model was used as a template to pick particles. This yielded approximately 270 particles per micrograph. Following an inspection of the particle picks, a total of 1,520,224 particles (box size 400 x 400 pixels) were extracted and averaged using *2D classification* utility. High resolution classes were selected and subjected to further rounds of *2D classification*. Several rounds of particle curation resulted in a dataset with 865,248 particles.

These particles were used by an *ab-initio reconstruction* job in *cryoSPARC* to generate five 3D maps without any reference. The five *ab-initio* classes were refined and the particles were classified amongst them with *heterogenous refinement*. The individual maps were refined to high-resolution and validated using the gold standard FSC with *nonuniform refinement*. A final map with best FSC resolution of 3.75 Å was obtained with 215,374 particles.

To generate an atomic model, the *Alphafold* predicted model was docked into the cryo-EM map. The model did not fit the map quite well. The model was modified manually to fit into the map with *ChimeraX* and *coot*. Once an approximate model fitting into the map was obtained, *phenix* was used to real-space refine the model against the map. The refinement statistics are shown in Tab. 4.2.

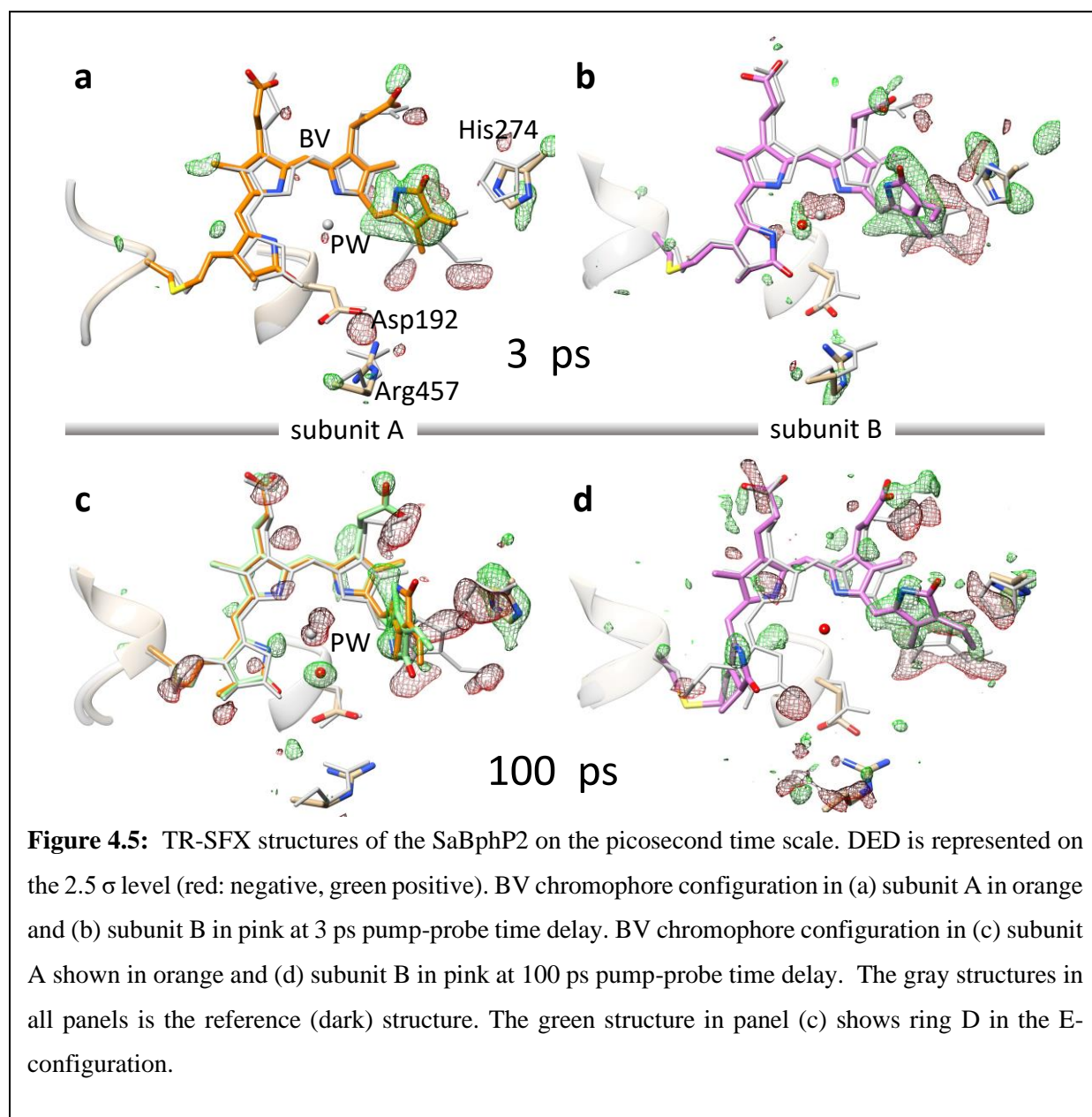


4.3 Results

4.3.1 Pump-probe TR-SFX at MFX and CXI

A 3 ps pump-probe data was collected at MFX using the data collection scheme shown in Fig. 4.3 a. The DED map at 3 ps is shown in Fig. 4.5 a,b. Unambiguous signals are present on and near the BV chromophore. Elsewhere on the map, the signal is essentially absent. It cannot be distinguished from noise. The difference signal at 3 ps is weaker than that reported previously for ns laser excitation. This is likely due to the fs laser excitation, since only one excitation is possible.

The effect of fs laser is seen on the BV chromophore and the neighboring amino acids such as which have all displaced upon photoexcitation. The position of the BV and the residues were



determined with the EED maps as explained in section 2.6.4. The extrapolation factor was on the order of 20 which is equivalent to 10% population transfer caused by the fs laser excitation. The D rings in both subunits are still in their Z configuration (Fig. 4.5 a,b). Some negative DED is present on the Cys13 to which the chromophore is covalently bound. A breakage of the sulfur bond

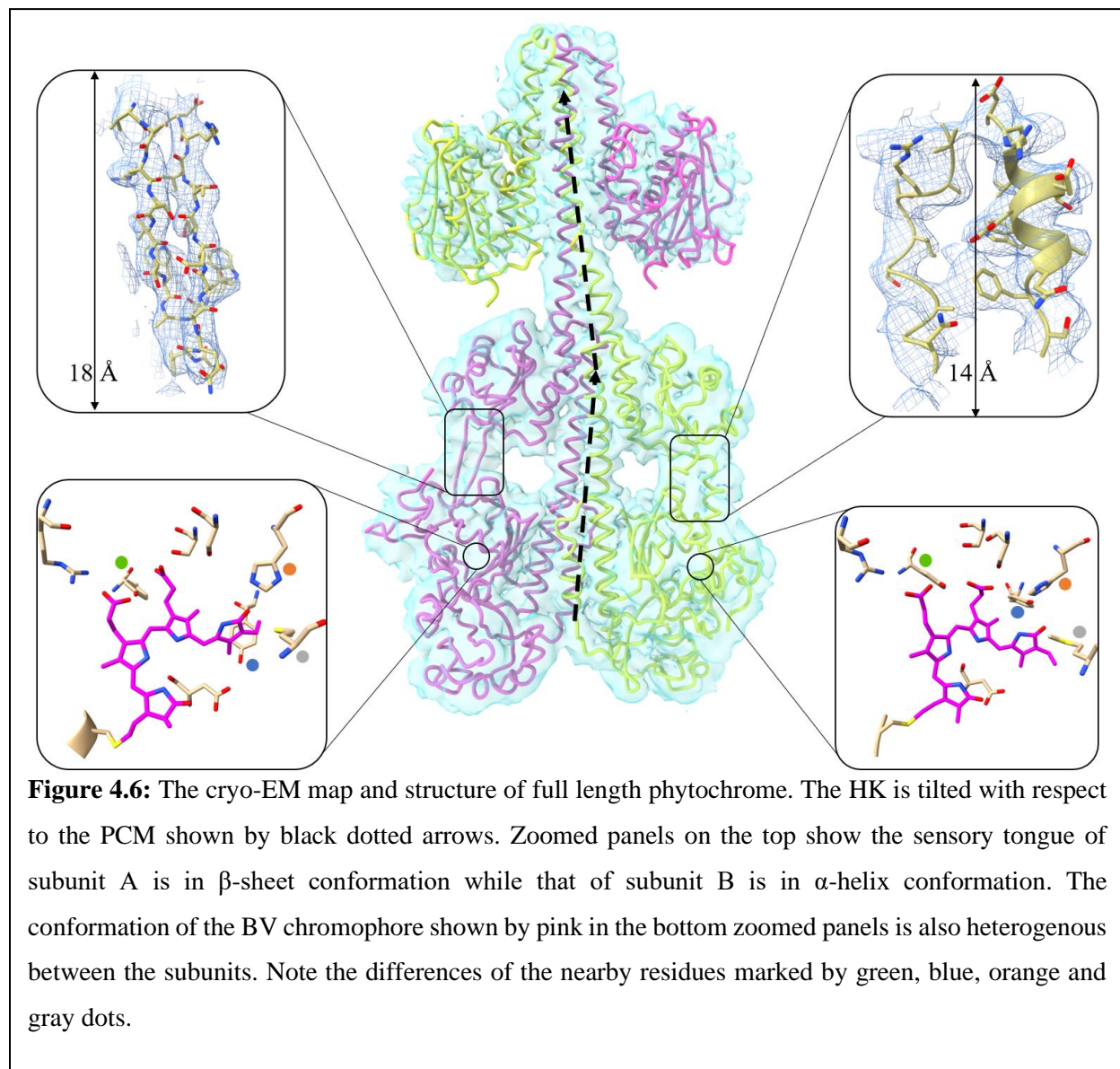
is improbable. However, the slight change in the orientation of ring A could also induce the similar DED signal. Any change in the isomerization and the displacement of the BV is directly sensed by the Cys13 residue. The signal is then transferred into the main protein structure as shown previously on similar timescales in the chromophore binding domain (CBD) crystals of *Deinococcus radioduran* (DrBphP) (Claesson et al., 2020).

A dataset with a pump-probe time delay of 100 ps was collected with 120 Hz at CXI using the data collection scheme shown in Fig. 4.3 b. Similar to 3 ps, strong difference electron density is located on the BV ring D (Fig. 4.5 c,d). In subunit B, the ring D is in the Z-configuration (as seen on 3 ps). However, the situation in subunit A is not that clear. Here, ring D can be oriented in both the Z and E orientations so that there is virtually no difference in the correlation factors between calculated and observed difference electron density values. Accordingly, we interpret the ring-D configuration in subunit A as a mixture of Z and E with a slight preference for the E-configuration.

4.4.2 Cryo-EM structure of full length phytochrome

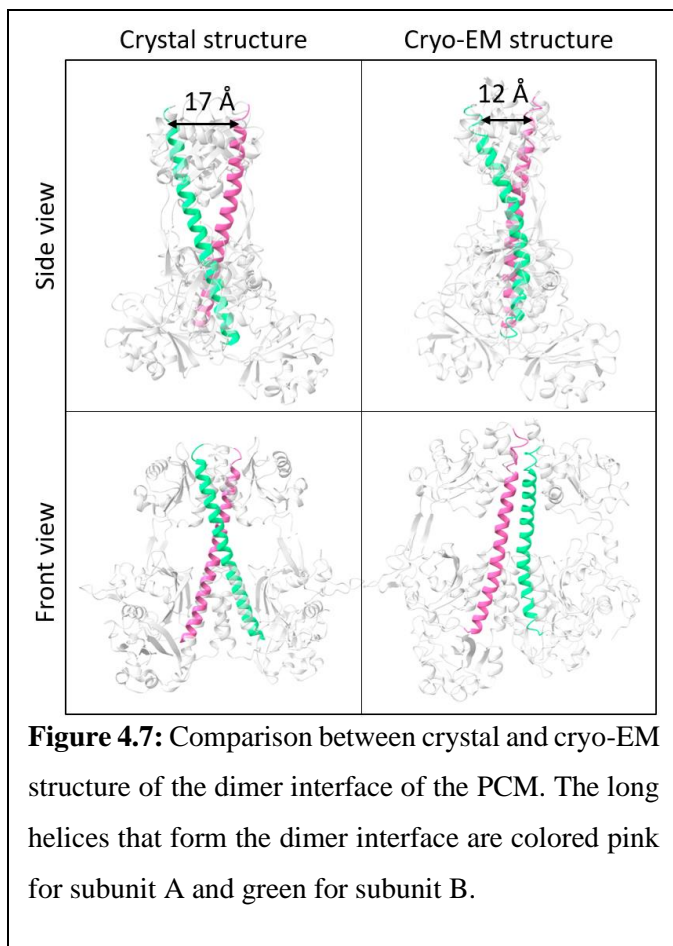
A map with overall resolution of 3.75 Å was obtained from the cryo-EM data of the full length SaBphP2. Local difference in resolution is observed for the stable PCM and the relatively flexible HK domain (Fig. 4.4). In the PCM, the resolution extends past 3 Å and the side chains are clearly distinguishable. Starting with the *AlphaFold* structure, the model was manually built and refined in this region. The resolution of the HK domain is rather weak at ~ 9 Å and an atomic model can not be built with confidence. Nevertheless, the map reproduces the butterfly shaped structure of the HK that is consistent with the previously determined crystal structure of HK alone (Marina et al., 2005). The overall structure is shown in Fig. 4.6. There are four major observations. First, the HK head is tilted towards one subunit. Second, there is heterogeneity in the conformation

of the sensory tongues in the two subunits. Third, the BV chromophores are also in different configuration between the two subunits. Fourth, the dimer interface of the PCM differs from the Pr structure determined by crystallography.



The tilt of the HK domain towards subunit A is accompanied by the tilt in the PCM towards subunit B (Fig. 4.6 black dashed line). This tilt is not a reconstruction artefact. The slanted configuration is also present in the 2D classes. The map shown in Fig. 4.6 is refined from the initial volume class

3 of the ab-initio reconstruction job. Even in other volume classes where the HK domain is not resolved (Fig. 4.4), the tilt in the PCM is observed hinting to the conformational homogeneity of the molecules. The sensory tongues and the BV chromophores for the two subunits are in different configurations. The top zoomed panels in Fig. 4.6 show the configuration of sensory tongues in subunits A and B respectively. In subunit A, it displays a parallel sheet configuration and in subunit B, it shows a helical

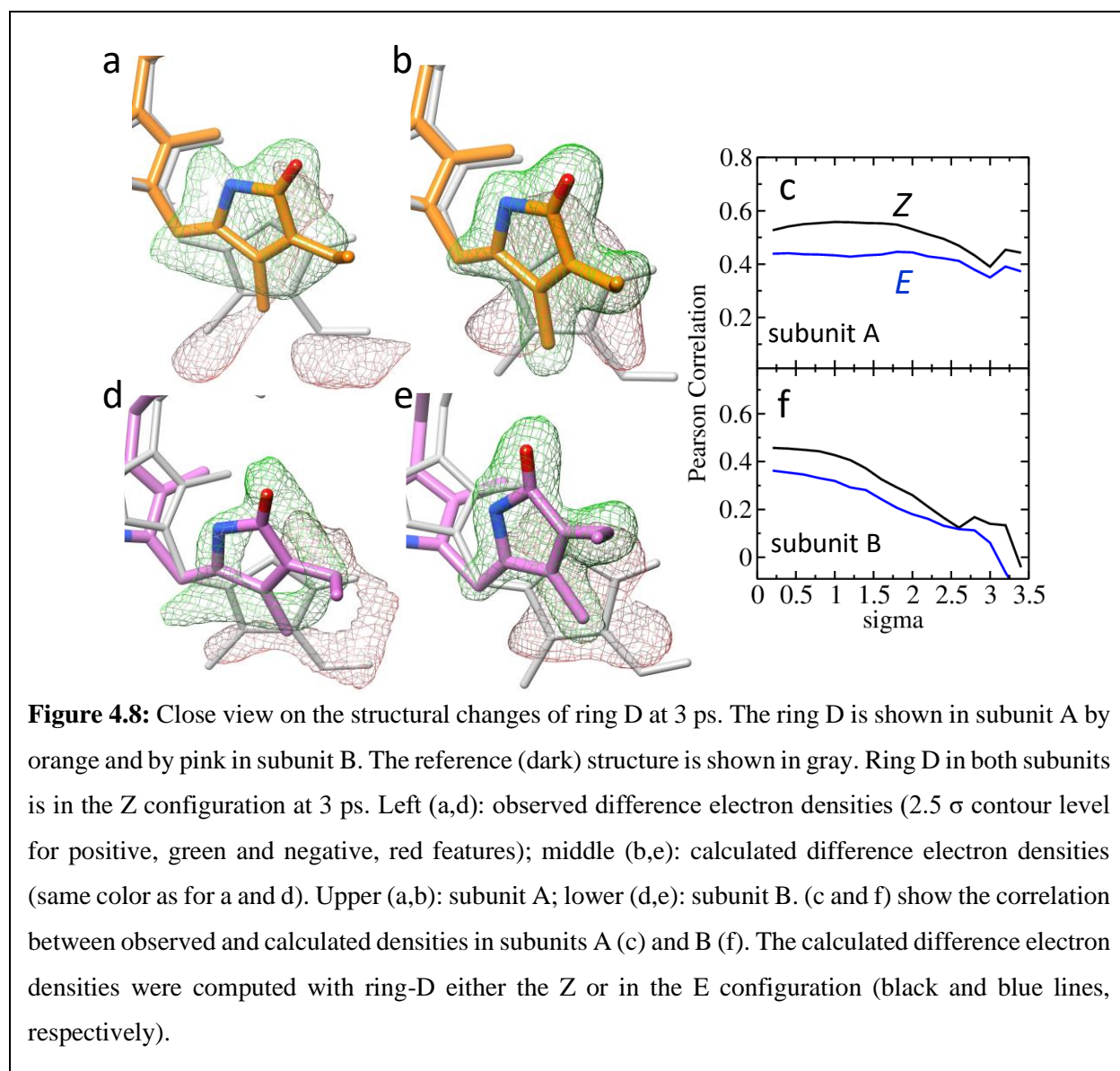


structure. The inspection of the BV chromophore (bottom zoomed panels in Fig. 4.6) shows similar differences. The ring D displays a Z configuration in subunit A vs a E configuration in subunit B. The position of amino acid residues around the chromophore are also different for each subunit. Particularly the residues, Tyr201, Tyr161, Met252 and His275 (marked in Fig. 4.6 by green, blue, orange and gray dots respectively) differ significantly between the subunits. Finally, the dimer interface is more parallel compared to PCM dark Pr structure (Fig. 4.7). The dimer interface is composed of two long α -helices from both subunits. In the crystal structure, the helices are crisscrossed when viewed both from the front and the side. In the cryo-EM structure, the dimer interface is more parallel when observed from the front but it still displays some crossing conformation on the side view. Consequently, the residues on the top of the dimer interface are

only ~ 12 Å apart in the cryo-EM structure while they are ~ 17 Å apart in the crystal Pr structure (Fig. 4.7).

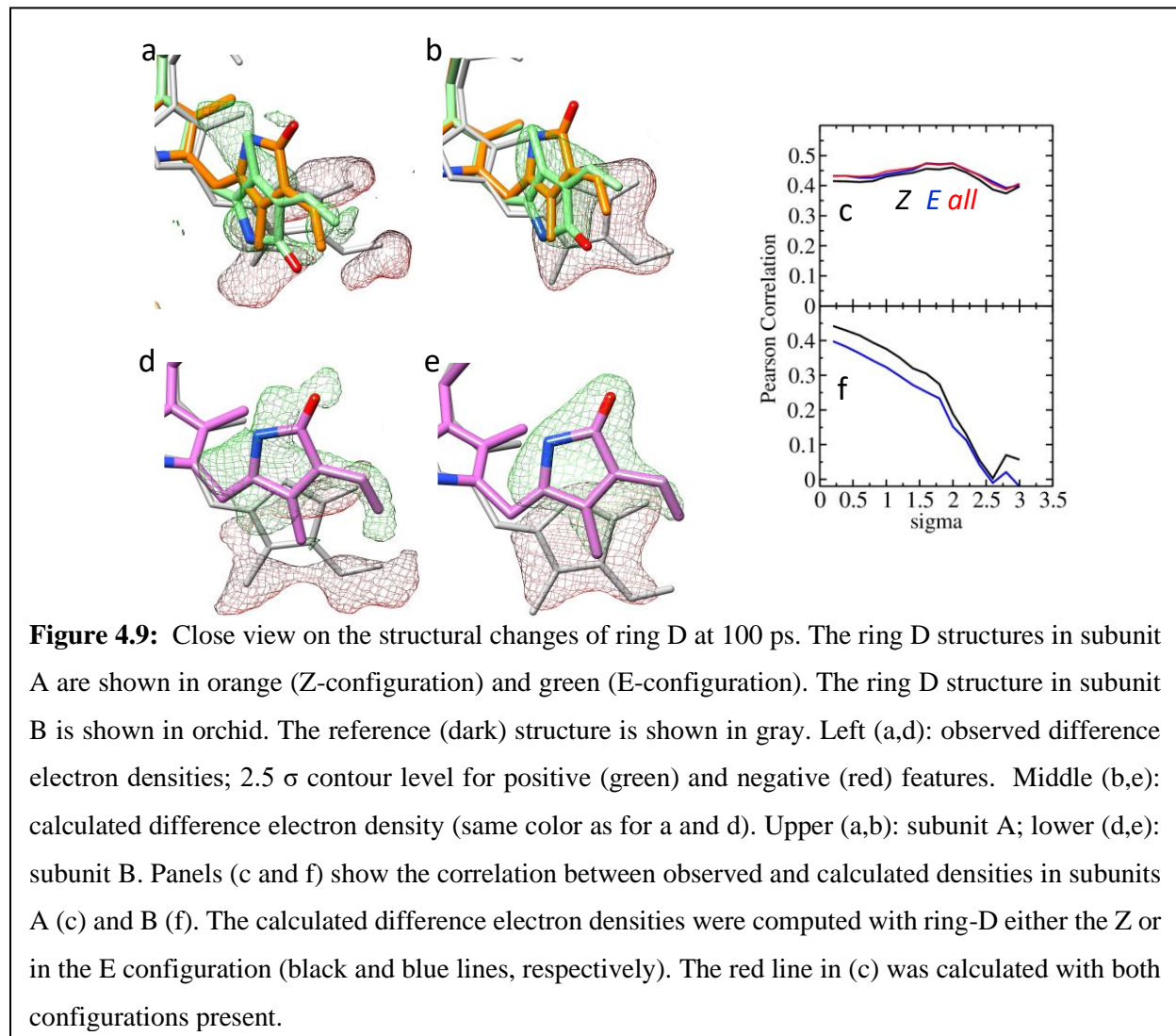
4.4 Discussion

4.4.1 Reaction initiation in SaBphP2 phytochrome



The difference maps at 3 ps and 100 ps time-delays show early events in the activation of the SaBphP2. Strong difference electron density features are present on the carbonyl, methyl and

vinyl groups of ring D already at 3 ps (Fig. 4.5). These can give a hint on how BV ring D isomerization may occur. The ring D rotations were assessed by measuring the change of the torsional angle φ^T defined by atoms C₁₄-C₁₅=C₁₆-N₁₇ (Fig. 4.8,4.9). The rotation about the C13-C14 single bond lifts the ring D out of the chromophore plane resulting in the strong DED. The rotation up to 56° about the torsional angle is substantial. This then orients the ring D away from



the ring C, which facilitates rotation of ring D by allowing the ring D nitrogen to slip through below the methyl group in ring C. Following the rotation, the ring D, now in the E configuration, relaxes into the chromophore plane. The resultant conformation is observed at later time point as

well.

The difference density for the PW is weak, and absent in subunit A at both 3 ps and 100 ps time delay. This is in contrast to results on the smaller DrBphP CBD where the PW has been at 1 ps (Claesson et al., 2020). However, the chromophore binding pocket in CBD crystals It appears that the pyrrole water in the SaBphP2 PCM, and potentially in all PCMs, has a less pronounced role in the early events. The water stays bound to BV at these earlier time points, and the observed displacements are a result of the BV displacement.

4.4.2 Full length phytochrome in Pr/Pfr heterodimeric form

All the four important observations made in the cryo-EM structure of the full length SaBphP2 can be explained by a hybrid Pr/Pfr structure. The protein purification was performed under the green safety light and the absorption spectra was measured to confirm the protein is in Pr state. However, during the cryo-EM grid preparation, the protein was exposed to ambient light for up to 30 minutes. During this time, the phytochrome can be excited with the 640 nm wavelength present in the ambient light. It might have led to the subunit B to convert to Pfr state. As seen on time-resolved studies on the SaBphP2 PCM crystal structures, the extent of reaction initiation can be different on two subunits although the phytochrome is a homo dimer. This non uniform excitation leads to the heterodimeric structure.

The conformation of the BV and the nearby residues in subunit A are consistent with the Pr structures of the PCM. The orientation of the BV and the conformations of the residues in the chromophore binding pocket in subunit B are in accordance with the published structure of DrBphP PCM in the Pfr state. Similarly, the configurations of the sensory tongues in subunits A and B also support a (Pr/Pfr) hybrid structure where the Pr state assumes a β -strand and the Pfr

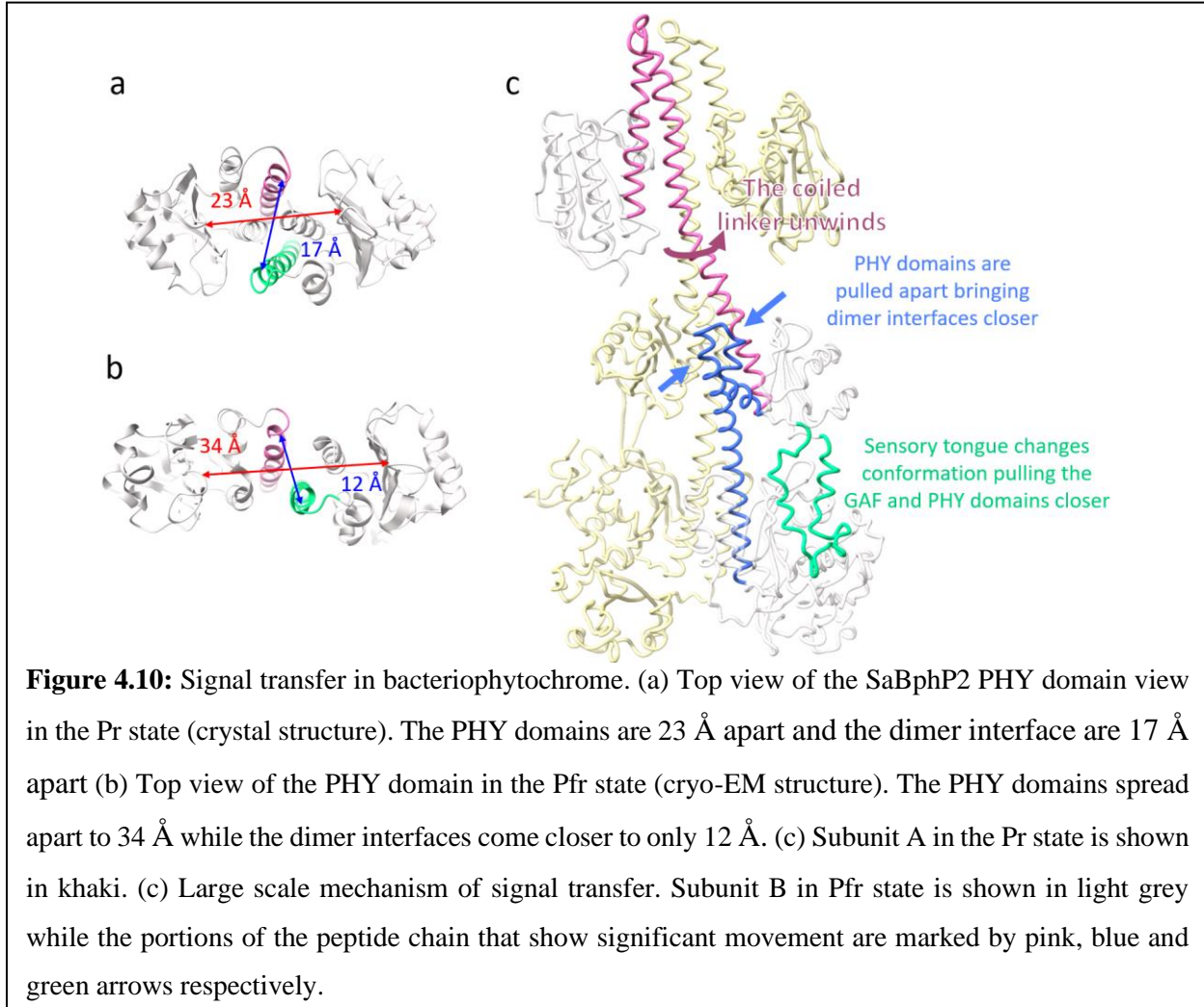
state assumes an α -helix form, respectively. The tilt in the HK domain could also be explained by the hybrid structure in which a strained subunit in the Pfr state exerts mechanical force. The HK is pushed upward from one side that will result in the observed tilt. As the sensory tongue changes its conformation from β -sheet to α -helix the distance between the top of the GAF domain and the bottom of the PHY domain where the sensory tongue resides decreases from 18 Å to 14 Å (Fig. 4.6). This contraction pulls the PHY domains apart from 23 Å to 34 Å. At the same time the dimer interface helices come closer.

It is important to consider that the phytochrome can also exist as a heterodimer *in vivo*. It has been suggested that the heterodimeric Pr/Pfr phytochromes may be present in many flowering plants (Sharrock & Clack, 2004). In addition, the hetero dimerization in some plant phytochromes has been associated with much faster dark reversion rate compared to homo dimers in Pfr state (Klose et al., 2015). Most crystal structures of bacteriophytochromes are homodimers. The homogenous proteins were crystallized which may have resulted in apparent homogeneity in the dimers. Since there is a legitimate reason of contamination with the ambient light, it is hard to discriminate if the hybrid form is due to rogue excitation or due to the native heterodimeric state. More controlled experiments are necessary to determine the cause of the hybridization.

4.4.3 Allosteric signal transfer in phytochrome

Unlike the published Pfr structure as shown in Fig. 4.2, we do not observe the large scale opening of the PHY domain. Analysis of the full-length structure hints that openings as large as those observed in truncated constructs are highly unconvincing. The presence of the HK domain on top would render those displacements very prohibitive. Movements of the PHY domain in tens of Å have been identified by solution scattering methods (Takala et al., 2014). As observed here,

the PHY domains move from 23 Å apart to 34 Å apart (Fig. 4.10 a,b) which corroborates the



solution based results. The opening of the PHY domains shown by the static Pfr structure of truncated phytochrome (Takala et al., 2014) is different from what we observe here. Those static structures may be affected by the truncation of the phytochrome which allows large scale splitting which might even be enforced by the packing in crystals. The cryo-EM structure presented here is free of such prejudice. Our data firmly suggest that the large-scale movement of the PHY domain suggested by solution-based method follows the motion presented here than that was previously described (Takala et al., 2014). Our structure is more in line with the crystal structure of the bathy phytochrome of *P. aeruginosa* (Yang, Kuk et al. 2008) which in the Pfr state does not show

large PHY domain separation and features a parallel dimer interface. The coiled linker (shown by pink in Fig. 4.10 c) that connects the HK to the PHY domain intersects such that the subunit A of the HK is atop the subunit B of PCM and vice versa. The point where the linkers intersect each other is higher as measured from the bottom of the linker in this hybrid structure compared to the *AlphaFold* Pr structure. It seems the effect of the PCM dimer interface coming closer is the unwinding of the twist in the linker which shifts the position of the intersecting point from the bottom of the linker that lies within the PHY domain (compare Fig. 4.1 vs 4.10) to higher in the HK dimer interface. This twist might be the final actual signal that the HK senses.

The following scenario emerges. The energy stored in strained BV chromophore upon photo-excitation is transferred to the protein surrounding the chromophore. This leads to a conformational change in the sensory tongue. The shortening of the sensory tongue upon sheet to helix transformation pulls the PHY domains apart and the dimer interface becomes more parallel. The movement of the PHY domain unwinds the coiled linker dimer interface (Fig. 4.10). The signal then reaches to the HK. With static structure of Pr/Pfr alone it is hard to discriminate if the sensory tongue changes configuration first to pull the PHY domains together or if the PHY domains coming together presses the sensory tongue to change conformation. To shine more light on that mechanism, time-resolved cryo-EM studies are necessary.

Remark: we recently determined the cryo-EM structures of the full-length SaBphP2 and the SaBphP2 PCM in the Pr forms rather than in the hybrid form. This was achieved by irradiating with 750 nm far-red light. The cryo-EM Pr structures corroborate the SaBphP2 PCM crystal structure in the Pr form. In particular the crossed dimer interface is reproduced. Results are not shown here because data analysis is still ongoing.

4.5 Outlook

The short-lived structural intermediates of SaBphP2 PCM presented here show early events of the isomerization which are characterized by a very early full isomerization and subtle conformational changes of the biliverdin chromophore and its nearest environment. However, the movements are heterogeneous between the different subunits. Some of the BV conformations can be unproductive as the quantum yield for the Pr to Pfr transition is quite low (approximately 10%–15%) (Carrillo et al., 2021). Large-scale structural changes that are expected have not observed even on millisecond times scales. Probably, the crystal packing limits such displacements. Cryo-EM offers a solution as it bypasses the need for crystallization. The full-length structure determined here offers an alternative explanation to large displacements detected by crystallography which is a stark contrast to what the static structures have shown. Time-resolved cryo-EM is the next step in understanding the mechanism of large flexible proteins and complexes like phytochromes. However, the time resolution is currently limited to ms time scale (Dandey et al., 2020; Unwin & Fujiyoshi, 2012).

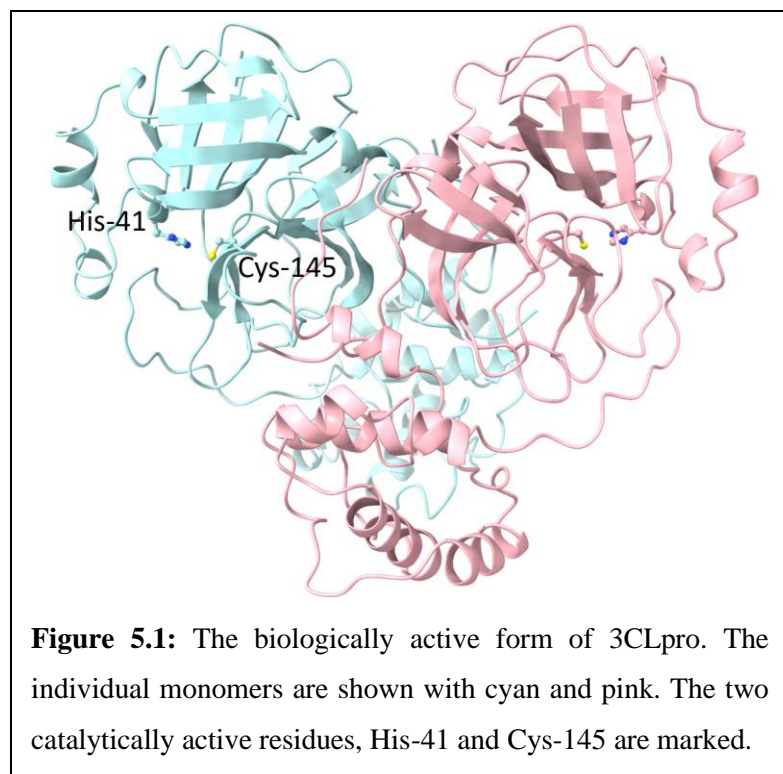
An argument may be made that as time-resolved cryo-EM methods will develop and the usefulness of TRX will diminish. Although that is not completely improbable, it will take many years if not decades for the TR cryo-EM to surpass TRX. Until then, the most effective course should be to use cryo-EM in tandem with TR-SFX. Ultrafast structural changes can be investigated by TR-SFX which can unravel in-depth chemical and physical mechanisms. Any large-scale structural changes that follow can be pursued with TR cryo-EM. Since cryo-EM is more accessible than TR-SFX at the moment, more and more structures can be solved with high precision due to the fast development of cryo-EM.

5. SARS CoV-2 Main Protease (3CLpro or Mpro)

The work on this project was performed during the pandemic. The results of the experiments were immediately published on the *bioRxiv* preprint server for rapid dissemination of knowledge of covid-19 related research. This chapter reproduces parts of the two publications available on *bioRxiv* (Malla et al., 2020, 2021). A manuscript is under preparation for a peer reviewed journal.

5.1 Introduction

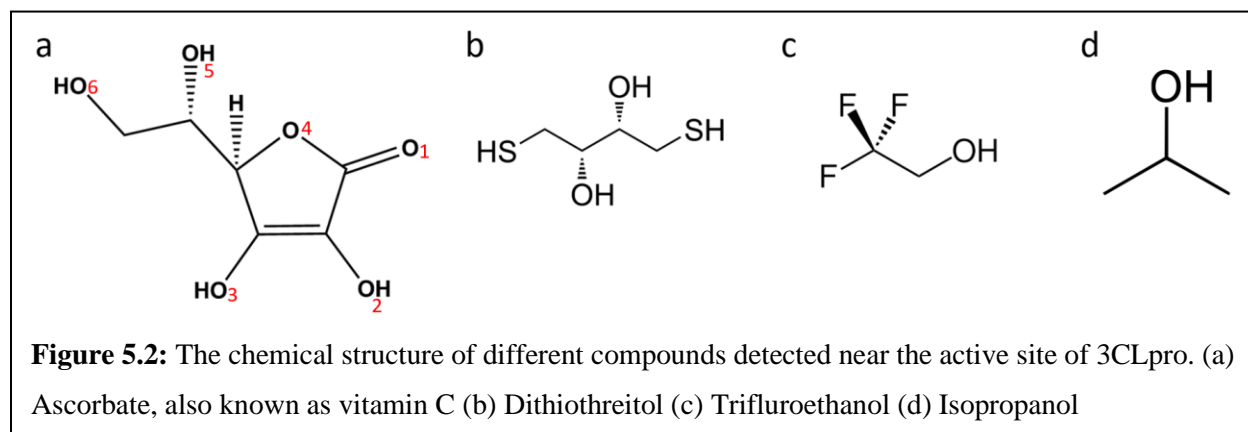
The coronavirus disease 2019 (COVID-19) pandemic is caused by the novel severe acute respiratory syndrome (SARS) coronavirus 2 (CoV-2). Due to the highly contagious nature of SARS-CoV-2, the pandemic caused almost 7 million deaths worldwide, making it one of the deadliest infectious diseases in history (*WHO Coronavirus (COVID-19) Dashboard With Vaccination Data*, 2023). Several vaccines are available (Barouch, 2022), that have contributed



immensely to stop the spread of the virus. Few antiviral medicines are also approved for the treatment of mild to moderate COVID-19 in people who are more likely to get very sick. During the time pandemic was prevalent, the vaccine and treatment costs has been free. However recently, the WHO declared an end to COVID-19 pandemic. The government

will soon stop supplying the COVID treatments for free. Still, there are thousands of people who get infected daily and are at risk of severe illness (<https://www.worldometers.info/coronavirus/>). Each medication of *Paxlovid* treatment costs \$530 (Lupkin, 2022) which is discounted price for buying 20 million dosages in bulk by the U.S. government. Similarly, the cost of Pfizer's vaccine is expected to quadruple in price, from the discounted rate the government pays of \$30 to \$120 (Allen, 2022). This calls for a need for an effective and inexpensive medicine for the treatment and prevention of COVID-19.

The replication of the SARS CoV-2 is dependent on the activity of two cysteine proteases, a papain like protease (PLpro), and the 3C like protease (3CLpro) (Cui et al., 2018). The 3CLpro is investigated in this dissertation. In its functional form the 3CLpro (also known as the main protease-Mpro) is a homo dimer with Cys/His dyad in the catalytic site (Fig. 5.1). The 3CLpro tailor cuts various essential virus proteins out of a long poly peptide translated from virus RNA. These proteins are responsible for the replication and transcription of the viral genome, and thus the contagiousness (Jamison et al., 2022). The 3CLpro is therefore a prime drug target, and any compound that that inhibits it is a potential drug.



We report various structures of 3CLpro determined from different crystal forms at cryogenic as well as room temperature. The structures reveal significant flexibility in the enzyme, particularly around the active site. In addition, several soaking experiments were performed to investigate the binding of readily available compounds (Fig. 5.2) to the 3CLpro.

5.2 Methods

5.2.1 Protein purification and crystallization

The 3CLpro was synthesized and optimized for expression in *E. coli* by *GenScript Biotech Corp.* who also provided the expression system. Cells were grown at 37° C to a OD₆₀₀ value of 0.6 followed by induction with 1 mM IPTG. After 3 hours, the culture was induced a second time by 1 mM IPTG. Cells were harvested in lysis buffer (20 mM Tris-Base, 150 mM NaCl, pH 7.8). After lysis of the bacterial cells, debris was centrifuged at 50,000 g for 1 hour. The lysate was let stand at room temperature for 3 hours. This is to let 3CL pro to self-cleave into a functional form from a long polypeptide. The lysate was pumped through Talon Co⁺² metal ion affinity chromatography column. The column was washed with using a cycle of high salt buffer (20 mM Tris-Base, 1 M NaCl, pH 7.8) followed by low salt buffer (20 mM Tris-Base, 50 mM NaCl, pH 7.8) with 20 column volumes each. The protein was eluted by 300 mM imidazole. Immediately, the buffer containing the protein was exchanged by 20 mM Tris-Base, 150 mM NaCl, pH 7.8. Reducing agents were needed to protect the cysteines in the 3CLpro from forming disulfide bonds that would otherwise lead to protein aggregation. Either dithiothreitol (DTT) or sodium ascorbate (ASC, commonly known as vitamin C) were added.

Three different types of crystals were produced. The main precipitating agent is PEG3350 for all preparations. The difference is in the type and concentration of the reducing agents used (DTT or

ASC) and the additives. Nevertheless, they are described as condition 1,2 and 3 respectively. Condition 1 uses DTT as reducing agent while conditions 2 and 3 use ASC.

Condition 1: Crystals were produced by mixing 4 mg/ml protein (in 0.1 mM DTT) in batch mode with same amount of mother liquor consisting of 25 % w/v PEG 3350, 100 mM Bis-Tris, pH 6.5. For soaking experiment, the crystals were soaked in mother liquor containing ebselen in powder form for two days. Because ebselen is not soluble in water, enough ebselen that would otherwise produce a 50 mM solution was added. Microcrystals with this condition were grown by mixing 20~25 mg/ml protein (in 0.5 mM DTT) in batch with the same amount of mother liquor described above. These microcrystals were also soaked in mother liquor containing 50 mM ebselen in powder form for two days.

Condition 2: crystals were grown in hanging drop method by mixing 2 ul of 20 mg/ml protein (in 5 mM ASC) with an equal amount of reservoir containing 15% PEG 3350, and 4% trifluoroethanol (TFE) as additive. The crystals were soaked in mother liquor containing additional 120 mM ASC for 3 minutes before freezing.

Condition 3: Crystals were grown the same way as in condition 2 but with 10 mM ASC (instead of 5 mM) and 3% isopropanol (IPA) as additive. These crystals were also soaked in additional ASC of 300 mM for up to 30 minutes before freezing.

5.2.2 Data collection

Cryo experiments were performed at the beamline ID-19 of APS. The crystals were mounted in MiTeGen (MiTeGen, Ithaca) micro-loops (30 - 50 μm) and directly frozen in pucks suspended in liquid nitrogen. The dewar with the pucks was shipped to APS. Automated (robotic)

data collection was employed using the proprietary *sbccollect* program (Rosenbaum et al., 2006), and processed by *HKL-3000* (Minor et al., 2006).

The SFX room temperature data was collected with condition 1 microcrystals at the MFX instrument (Boutet et al., 2016) at the LCLS. The 40fs long X-ray (9.53 keV) pulses were operating at 120 Hz. The crystal slurry was delivered into the X-ray beam using the concentric Microfluidic Electrokinetic Sample Handling (coMESH) injector (Sierra et al., 2015). The DPs were collected on ePix10K 2M detector set to auto gain switching mode. *Cheetah* (Barty et al., 2014) and *CrystFEL* (White et al., 2012) were employed to process the data.

Table 5.1 Data collection and refinement statistics

	Condition 1 cryo	Condition 1 room Temp	Condition 2	Condition 3
Additive [mM]	DTT: 0.1	DTT: 0.5	ASC: 10 TFE	ASC: 10 ISO
Temperature [K]	100	295	100	100
X-ray source	APS	LCLS	APS	APS
beamline/instrument	19-ID-D	MFX	19-ID-D	19-ID-D
Resolution [Å]	2.3	2.3	2.2	1.7
Space group	C2	C2	P2 ₁ 2 ₁ 2 ₁	P2 ₁ 2 ₁ 2
a,b,c (Å), β(°)	113.4 53.4 44.7 β=102.8	117.6 55.4 45.6 β=100.5	65.4, 67.5, 157.5	44.5, 63.2, 106.5
Observed Reflections	35168	2646608	142755	183117
Unique Reflections	11881	13010	33249	32557
Redundancy	3.1	203.4	4.3	5.6
Completeness [%]	89.3	100	92.5	96.3
CC _{1/2} (at d _{min})	0.99 (0.48)	0.97 (0.17)	0.99 (0.32)	0.99 (0.40)
Rmerge or R-split [%]	5.4	16.8	10.1	12.8
R _{cryst} /R _{free}	18.6/28.0	20.8/26.8	20.6/26.3	20.6/24.7

#of subunits per asymmetric unit	1	1	2	1
Ligand	1 DTT	1 DTT	A: 2 TFE B: 1 ASC, 1 TFE	2 IPA
ligand occupancy	DTT: 0.5	DTT:0.65	ASC: 0.62 (B) TFE (A/B): 0.72/0.73	IPA: 1.0/0.88
# of water molecules	124	12	188	181
RMSD bond/angles	0.008/0.986	0.009/1.183	0.008/1.031	0.008/1.102
coordinate error [Å]	0.34	0.48	0.34	0.19

5.2.3 Structure determination

Crystals grown from condition 1 were investigated first. A search model with PDB ascension code 6WQF was used for a molecular replacement. The initial model was refined with phenix. The microcrystals produced with same condition collected at room temperature yielded the same space group and unit cell parameters as those collected at low temperature. The room temperature structure is deposited in PDB with ascension code 7JVZ. This refined structure was used as molecular replacement model to determine the phases for other datasets. DED_{omit} and DED_{polder} maps (Liebschner et al., 2017) were calculated for datasets soaked with ligands. A group occupancy refinement was performed to determine the occupancy values of the ligands in the active site.

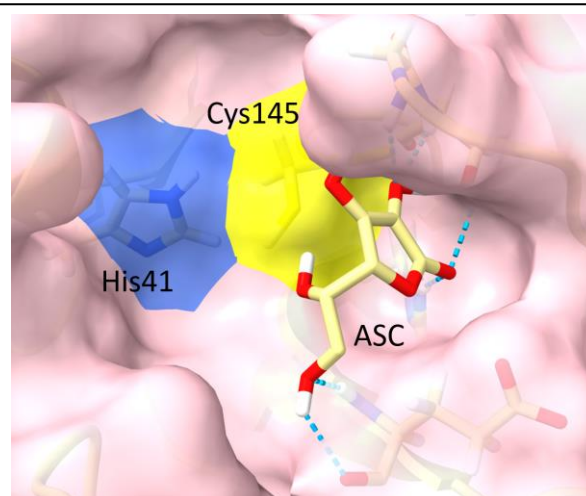
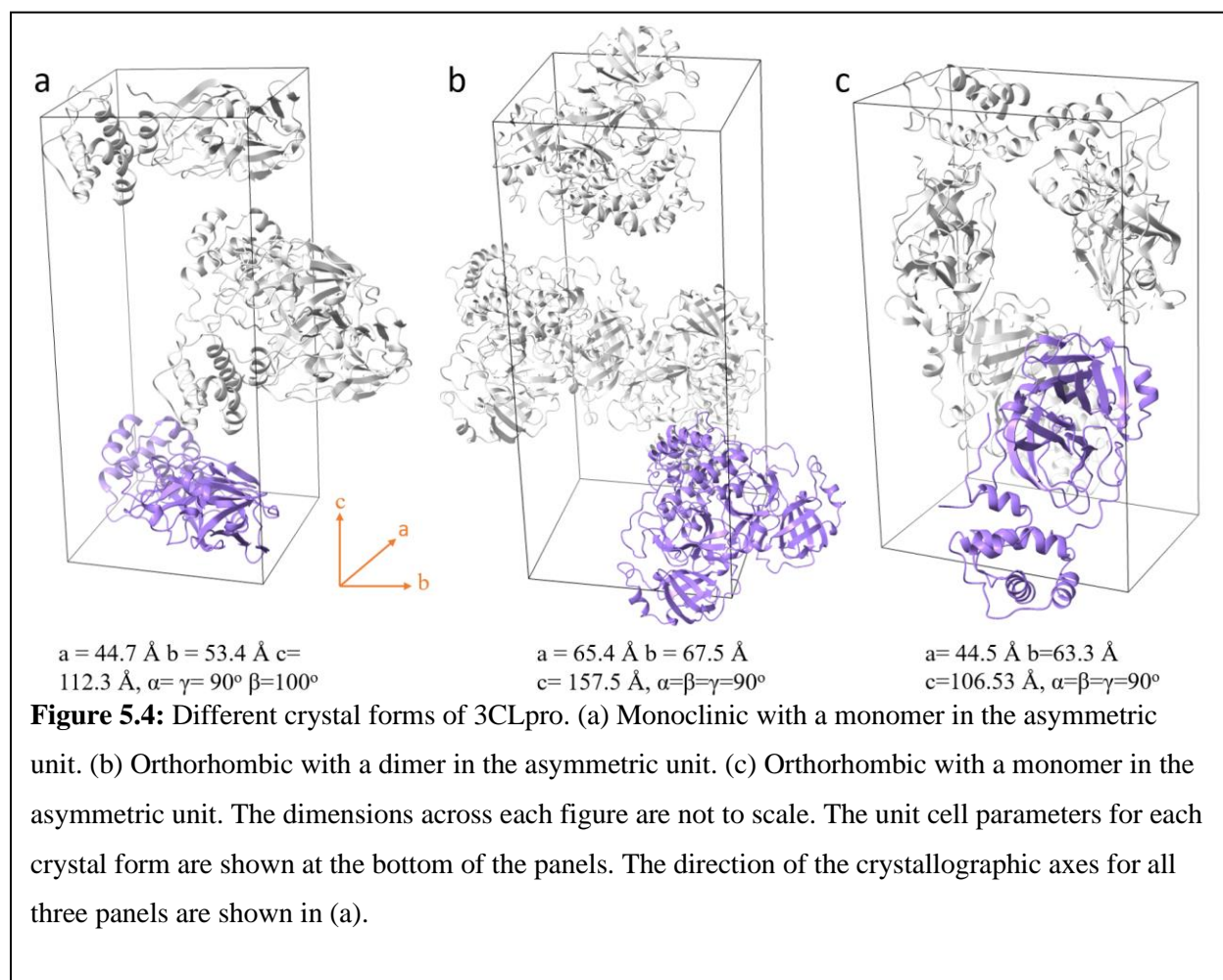


Figure 5.3: Molecular docking. The top ranked ligand position of molecular docking simulation on ascorbate binding to 3CLpro. The catalytic histidine and cysteine are marked. The hydrogen bonds made by ascorbate to the nearby amino acids are shown by blue dotted lines.

5.2.4 Molecular docking simulations

Molecular docking of ASC on 3CLpro dimer structure was performed with *AutoDock Vina 1.1.2* in *UCSF Chimera* (Eberhardt et al., 2021). A blind docking was performed on the dimer structure. The search box was large enough to cover the entire protein with a padding of 10 Å on all sides. The top ranked ligand on the active site had up to 7 hydrogen bonds with the surrounding residues (Fig. 5.3). Since, the specificity of ascorbate to the active site was established with blind docking, further docking simulations were performed focusing on the binding region. For this, both the dimer and the monomer structures were employed.

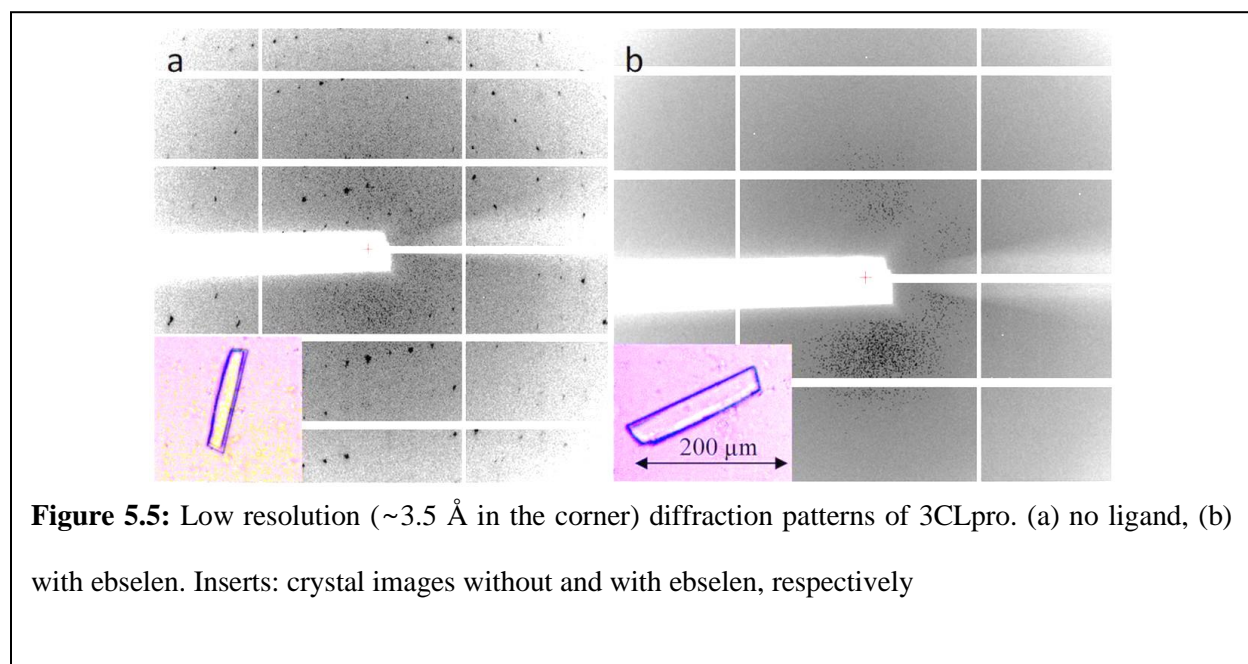


5.3 Results

5.3.1 Three different crystal forms

Each of the crystallization conditions yielded a different space group and a different composition in the asymmetric unit (ASU) (Fig. 5.3). Crystals from condition 1 resulted in a monoclinic crystal form with $C2$ space group with one monomer in the ASU (Fig 5.3 a). The unit cell consists of 4 such monomers. The functional dimer interface is made with the monomers from the adjacent unit cell. No large difference is found in the room temperature structure in this crystal form. The condition 2 yields an orthorhombic crystal form with $P2_12_12_1$ space group (Fig. 5.3 b). The ASU consists of functional dimer structure with 4 of these dimers in the unit cell. With condition 3, we obtain another form of orthorhombic crystal form with $P2_12_12$ space group (Fig. 5.3 c). The monomer is the ASU and there are 4 monomers in the unit cell.

5.3.1 Ebselen reacts with 3CLpro crystals



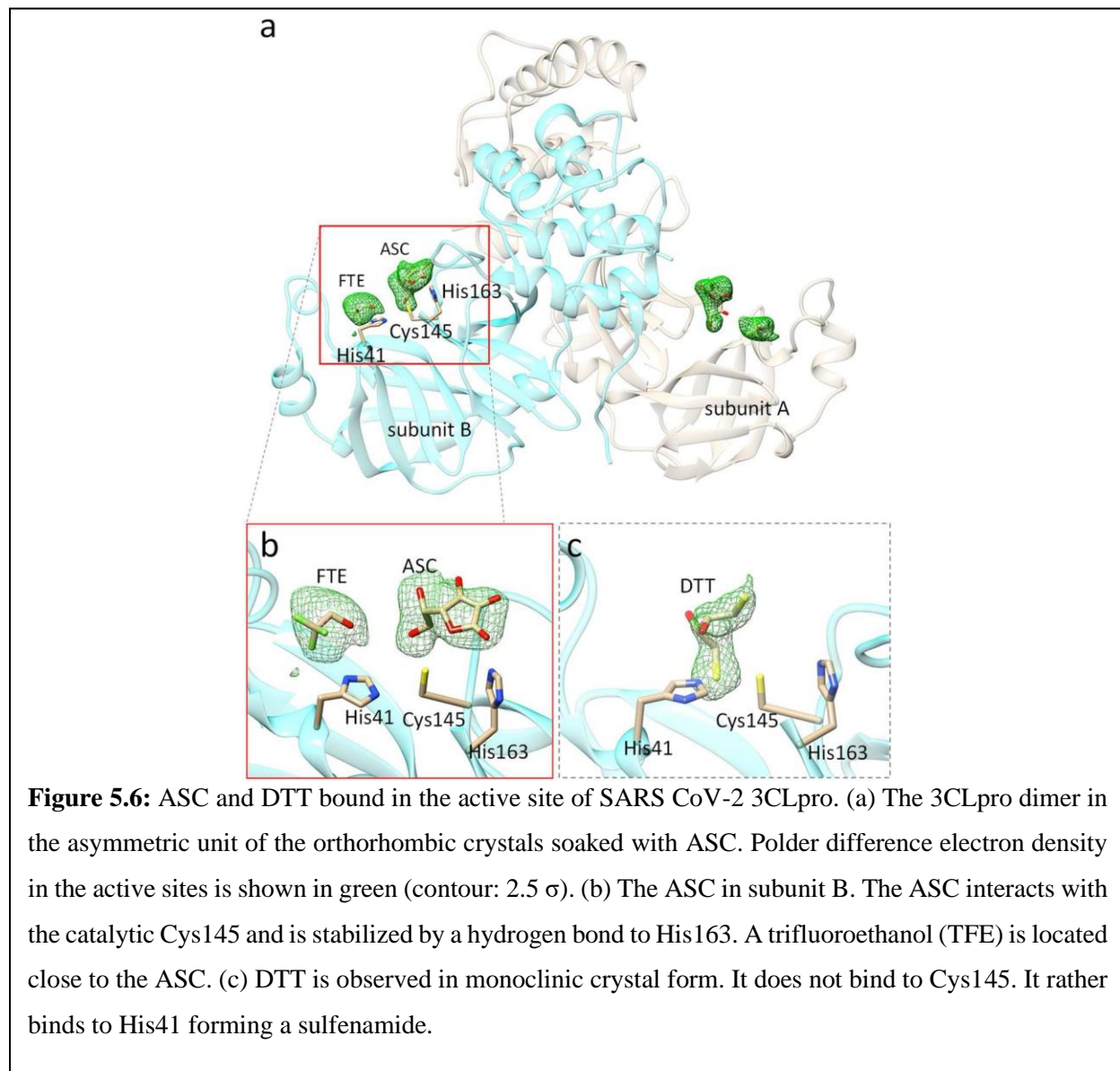
The C2 crystals maintained their morphology when soaked with ebselen powder for two days. While the unsoaked crystals diffracted beyond 2 Å, the crystals treated with ebselen did not show any Bragg reflections even at the lowest resolution (Fig. 5.5). All the trials were unsuccessful despite the visually crystalline shape. This effect is also observed in microcrystals soaked overnight with ebselen indicating a tight affinity to the 3CLpro. It is not clear what property of ebselen contributes to degrading the crystalline property of 3CLpro crystals.

5.3.3 Binding of ligands to the 3CLpro

Weak positive electron density appears between the catalytically active His145 and Cys41 in both the cryo and the room temperature structures of the C2 crystal form. A DTT molecule that is present in the protein buffer can be modeled there (Fig. 5.6 c). One of the sulfur atoms of the DTT binds to the catalytically active residue. The distance to one of the nitrogen atoms in His41 (1.5 Å) is substantially shorter than to the terminal sulfur atom in Cys145 (2.3 Å). It appears the DTT forms a sulfenamide bond with the histidine instead of a disulfide bond with the cysteine. A different reducing agent is required to prohibit DTT from blocking the active site. ASC is an excellent reducing agent which can be used instead of DTT.

The 3CLpro co-crystallized with ASC in the second condition shows evidence of potential binding of the ASC in both of the active sites (Fig. 5.6 a). The switch also resulted in change of space group from C2 to P2₁2₁2₁. Positive electron density corresponding to ASC appears in the DED_{omit} map at about 3 to 3.7 Å from the Cys145 sulfur atom. The interaction is rather weak as the occupancy is only about 60~70%. However, it forms a tight hydrogen bonding network with Asn142, Gly143, His163 and Gln166. In addition to the ASC electron density, an additional density feature is present in the active site (Fig. 5.6 b). The smaller pillow-like electron density is

interpreted with a trifluoroethanol (TFE) that has been provided as an additive to the crystallization buffer. The binding of ASC in subunit B is more pronounced than in subunit A.



The $P2_12_12$ crystals diffracted to the highest resolutions. The structures could be refined at 1.7 \AA . However, only the electron densities for the small additive molecules can be observed but the density supporting the ASC cannot be identified.

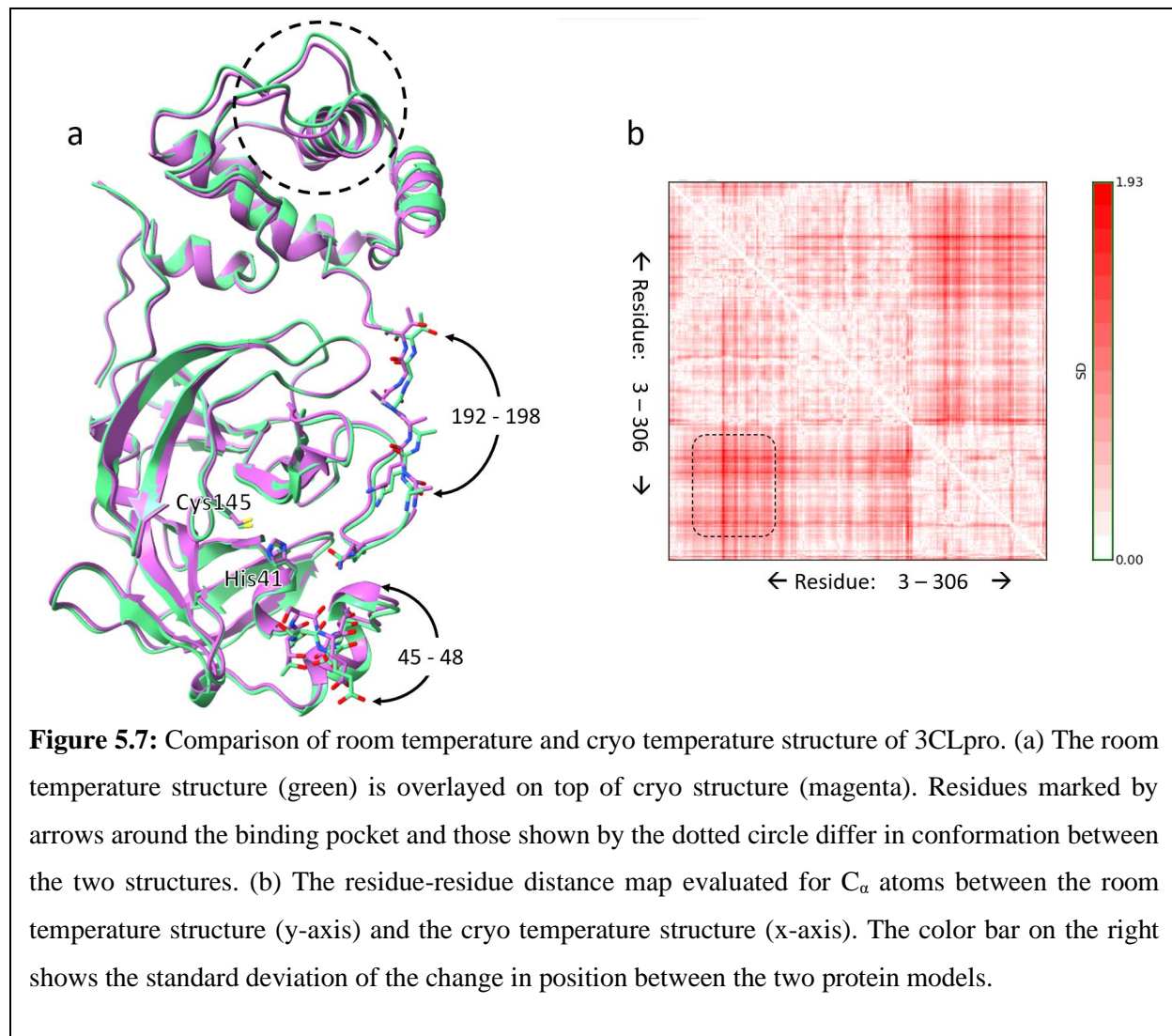
We performed an inhibition test using the *3CL Protease Assay Kit* (#78042-1, BPS Bioscience, San Diego, USA) to determine the potency of the ASC to inhibit 3CLpro. A fluorogenic substrate is mixed with 3CLpro. The substrate is an internally quenched 14-mer Förster resonance energy transfer (FRET) containing the donor (EDANS) and acceptor (DABCYL) fluorophores. When the substrate is intact, the EDANS and the DABCYL are in close proximity. The energy emitted by EDANS is quenched by the DABCYL. Upon proteolysis by 3CLpro, the substrate is cleaved to release the highly fluorescent peptide fragment containing EDANS. Thus, the fluorescence signal appears only when the enzyme is active. If the 3CLpro were to be inhibited, the fluorescence signal does not appear. Initially we measured the half maximal inhibitory concentration of (IC₅₀) of about ~40 mM. This is rather high compared to other potent inhibitors of 3CLpro whose IC₅₀ is in the range of μM . However, we also discovered that the ASC can react directly with the fluorescent fragment thereby quenching the fluorescence. It could not be determined with the available substrate if the absence of fluorescence is due to enzyme inhibition by ASC or due to the reaction of ASC with the fluorescent part. It is likely a combination of both.

5.4 Discussion

5.4.1 Structure plasticity of the active site of 3CLpro

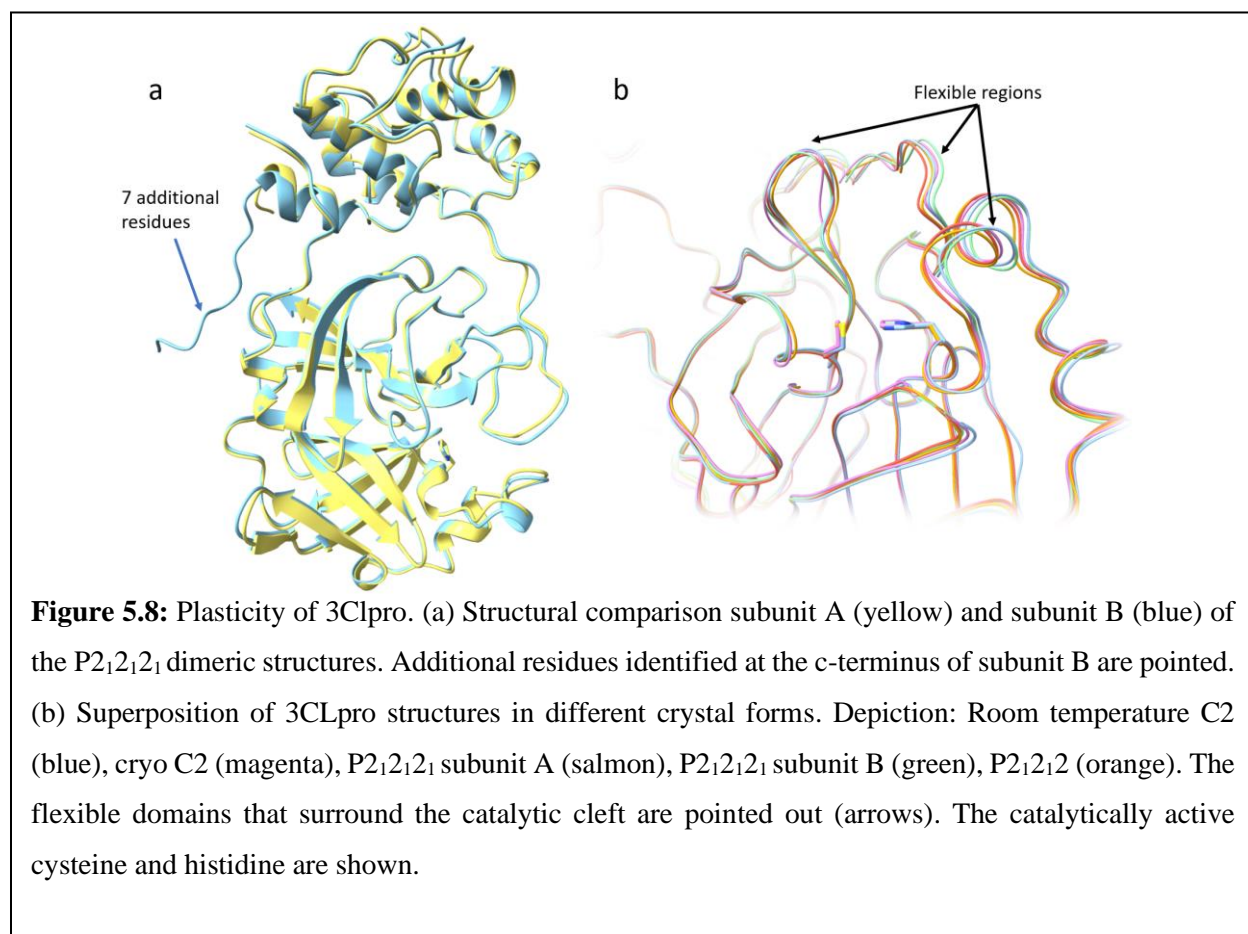
Since the structure of 3CLpro in C2 crystal form were determined at both cryo and room temperature, a structural can be performed to identify the differences between the two. Fig. 5.7 shows the comparison between the room temperature and the cryo temperature structures. The overall structures are similar with an R.M.S.D for C α atoms of 0.578 Å. This is higher than the previously reported difference of 0.32 Å by Kneller and colleagues (Kneller et al., 2020). However, the room temperature structure compared in that work was determined by a laboratory X-ray source where radiation damage is expected to persist. The room temperature structure presented

here is collected at an XFEL source where the diffraction patterns are collected from crystals free of radiation damage. The conformation of residues surrounding the active site differs between the room and the cryo temperature structures. Particularly the positions of the residues 45-58 and 189–198 have shifted by up to 1.7 Å. In addition, significant structural differences in the top region of the protease are marked by the dotted circle in Fig. 5.7 a. The displacements are easily visualized



in a residue-residue distance matrix (Fig. 5.7 b). The matrix helps in identification of displacement that are too small to identify solely by visualizing the structures. The red elements in the matrix marked by dotted rectangle indicate the residue pairs that have the highest variations in distance

in the two conformations. This corresponds to the flexible domains that are also observed in the top and bottom part of the protein in Fig. 5.7 a. Crystal structures are used for molecular docking simulations of various small molecules to screen potential therapeutics (Muralidharan et al., 2020; Talluri, 2020). For virtual screening of drug candidates using docking methods, the conformation of the target enzyme must be as close to its physiological state as possible (Ferreira et al., 2015). We believe, the radiation damage free conformations observed at room temperature may be more suitable for such screening studies.



It is also informative to compare the structure of the P₂₁2₁2₁ crystal form which has a native dimer in the asymmetric unit while in other crystal forms the dimer results from a monomer that is

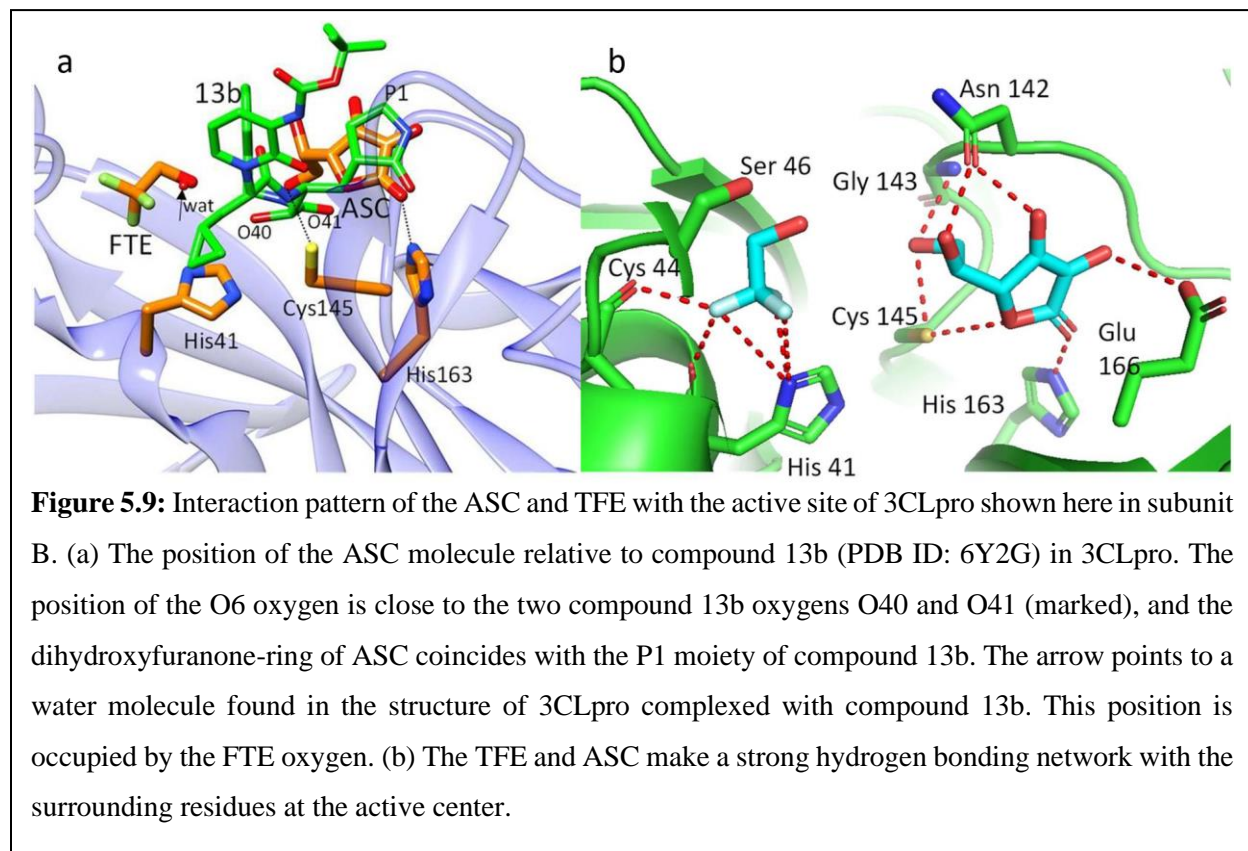
replicated by a crystallographic symmetry operation. The conformation of subunits differs significantly between the subunits (Fig. 5.8). In fact, 7 more residues including 2 histidines of the *hexa-his* tag are identified in the C-terminus of subunit B. When comparing only residues in the vicinity of the catalytic cleft, the structure of subunit B is more similar to room temperature than subunit A. This could be one of the reasons the ASC binding is more pronounced in the subunit B.

The comparison between 5 different structures of 3CLpro reveals significant structural flexibility of the enzyme in the vicinity of the active site (Fig. 5.8 b). Several secondary structure elements move by more than 1.5 Å away from their positions in the physiologically relevant room temperature structure. In particular, the displacement of the residues in subunit B of P2₁2₁2₁ is away from the active site in relation to the residues in room temperature C2 structure. This is expected since a large ligand is bound to the active site in this subunit and the surrounding residues move away to accommodate the ligand. Since, small ligands are bound to the other crystal forms, such conformational changes can also be characterized as induced fit due to ligand binding.

5.4.1 Potential binding of ascorbate to the 3CLpro

Although the inhibition of the 3CLpro by ASC could not be identified with inhibition tests, there is still evidence from the crystallographic data. Comparing the position of ASC/TFE with the position of compound 13b show similarities among the key atoms (Fig. 5.9 a). Compound 13b is a potent inhibitor of the 3CLpro. The positions of the two compound 13b oxygens O40 and O41 in the 3CLpro are close to the O6 oxygen of the ASC. The 5-member dihydroxyfuranone ring of the ASC (Fig. 5.9 a) occupies a similar position as the moiety P1 of compound 13b. The FTE oxygen position is reflected by a structural water found in the compound 13b complexed 3CLpro structure. In addition, the position of the ASC determined by the molecular docking simulation

overlaps the same location where the electron density for ASC was observed (Fig. 5.9 b). In this position the ASC makes up to 7 hydrogen bonds with the surrounding residues suggesting a strong binding affinity.



Vitamin C is a potent antioxidant and has been shown to have antiviral activity for more than half a century (Pauling, 1971). It is available in synthetic form and found naturally in citrus fruits and green leafy vegetables. Emerging literature suggests that ASC may also play an adjunctive role in the treatment of a variety of viral infections (Colunga Biancatelli et al., 2019; Fowler Iii et al., 2017). It has been suggested that Vitamin C in high dosages is directly virucidal (Furuya et al., 2008; Pauling, 1971). This assumption was based on *in vitro* studies, where very high doses of

ascorbate, in the presence of free copper and/or iron, has virucidal activity, presumably through the generation of hydrogen peroxide and other radical species (Furuya et al., 2008).

5.5 Outlook

In the last few decades, the world has suffered epidemics caused by new infectious agents, such as SARS and MERS. Emergence of such agents cannot be predicted. The development of effective antiviral drugs for immediate clinical use is challenging. New drug development normally takes years of investigation and cost a large amount of money. The repurposing of already approved drugs offers an alternative solution. The drugs can be screened for against potential drug targets and if effective will be on a fast track for clinical use. Attempts to determine binding of 3CLpro with Ebselen were not successful most likely due to two reasons: (i) Ebselen is not soluble enough to diffuse inside the protein crystals, and (ii) crystals soaked overnight with Ebselen lose their diffractive property. Nevertheless, the methods presented here can assist in the discovery of other drug leads with pharmaceutical potential. This is one of the effective ways of responding to new infectious diseases that currently lack specific drugs.

6. Summary

The three biological macromolecules investigated here each provided interesting cases for time-resolved experiments to determine function with near atomic structures. Both, pump-probe and mix-and-inject techniques were employed with serial crystallography to investigate photoreactive proteins and enzymes. Experiences gained from these experiments will be used to design new avenues to determine time-resolved cryo-EM structures. We already determined reference structures with cryo-EM (here for the bacteriophytochromes) of which only one is presented. We and our collaborators at NYSBC are looking forward to collecting time-points on a bacteriophytochrome that is excited by an intense laser pulse. This would constitute a groundbreaking experiment in cryo-EM. Data analysis will be different from the crystallographic counterpart, since cryo-EM is a single particle method and not an ensemble method as crystallography. Using the single-particle information, energy landscapes of intermediates and probable transition pathways between the intermediates can be determined (Dashti et al., 2020; Hosseinizadeh et al., 2021) to gain a more complete view of the trajectory of particles through conformational space.

References

- Abbe, E. (1873). Beiträge zur Theorie des Mikroskops und der mikroskopischen Wahrnehmung: I. Die Construction von Mikroskopen auf Grund der Theorie. *Archiv Für Mikroskopische Anatomie*, 9(1), 413–418. <https://doi.org/10.1007/BF02956173/METRICS>
- Adrian, M., Dubochet, J., Lepault, J., & McDowell, A. W. (1984). Cryo-electron microscopy of viruses. *Nature* 1984 308:5954, 308(5954), 32–36. <https://doi.org/10.1038/308032a0>
- Alberts, B., Heald, R., Johnson, A. D., Morgan, D. O., Raff, M. C., Roberts, K., & Walter, P. (2022). *Molecular biology of the cell* (7th ed.). W.W. Norton & Co.
- Allen, A. (2022, November 8). Pfizer’s Covid Cash Powers a ‘Marketing Machine’ on the Hunt for New Supernovas. *KFF Health News*.
- Alter, O., Brown, P. O., & Botstein, D. (2000). Singular value decomposition for genome-wide expression data processing and modeling. *Proceedings of the National Academy of Sciences*, 97(18), 10101–10106. <https://doi.org/10.1073/PNAS.97.18.10101>
- Ambler, R. P. (1980). The structure of β -lactamases. *Philosophical Transactions of the Royal Society of London. B, Biological Sciences*, 289(1036), 321–331. <https://doi.org/10.1098/RSTB.1980.0049>
- Auldridge, M. E., & Forest, K. T. (2011). Bacterial phytochromes: More than meets the light. *Critical Reviews in Biochemistry and Molecular Biology*, 46(1), 67–88. <https://doi.org/10.3109/10409238.2010.546389>
- Baneyx, F. (1999). Recombinant protein expression in Escherichia coli. *Current Opinion in Biotechnology*, 10(5), 411–421. [https://doi.org/10.1016/S0958-1669\(99\)00003-8](https://doi.org/10.1016/S0958-1669(99)00003-8)
- Barends, T. R. M., Foucar, L., Ardevol, A., Nass, K., Aquila, A., Botha, S., Doak, R. B., Falahati, K., Hartmann, E., Hilpert, M., Heinz, M., Hoffmann, M. C., Köfinger, J., Koglin, J. E., Kovacsova, G., Liang, M., Milathianaki, D., Lemke, H. T., Reinstein, J., ... Schlichting, I. (2015). Direct observation of ultrafast collective motions in CO myoglobin upon ligand dissociation. *Science*, 350(6259), 445–450. https://doi.org/10.1126/SCIENCE.AAC5492/SUPPL_FILE/BAREND.SM.REVISION.1.PDF
- Barouch, D. H. (2022). Covid-19 Vaccines — Immunity, Variants, Boosters. *New England Journal of Medicine*, 387(11), 1011–1020. https://doi.org/10.1056/NEJMRA2206573/SUPPL_FILE/NEJMRA2206573_DISCLOSURES.PDF
- Barty, A., Kirian, R. A., Maia, F. R. N. C., Hantke, M., Yoon, C. H., White, T. A., & Chapman, H. (2014). Cheetah: Software for high-throughput reduction and analysis of serial

- femtosecond X-ray diffraction data. *Journal of Applied Crystallography*, 47(3), 1118–1131. <https://doi.org/10.1107/S1600576714007626>
- Battye, T. G. G., Kontogiannis, L., Johnson, O., Powell, H. R., & Leslie, A. G. W. (2011). iMOSFLM: a new graphical interface for diffraction-image processing with MOSFLM. *Urn:Issn:0907-4449*, 67(4), 271–281. <https://doi.org/10.1107/S0907444910048675>
- Bendory, T., Bartesaghi, A., & Singer, A. (2020). Single-particle cryo-electron microscopy: Mathematical theory, computational challenges, and opportunities. *IEEE Signal Processing Magazine*, 37(2), 58. <https://doi.org/10.1109/MSP.2019.2957822>
- Berman, H. M., Westbrook, J., Feng, Z., Gilliland, G., Bhat, T. N., Weissig, H., Shindyalov, I. N., & Bourne, P. E. (2000). The Protein Data Bank. In *Nucleic Acids Research* (Vol. 28, Issue 1, pp. 235–242). Oxford University Press. <https://doi.org/10.1093/nar/28.1.235>
- Bernal, J. D., & Crowfoot, D. (1934). X-Ray Photographs of Crystalline Pepsin. *Nature 1934* 133:3369, 133(3369), 794–795. <https://doi.org/10.1038/133794b0>
- Blake, C. C. F., Koenig, D. F., Mair, G. A., North, A. C. T., Phillips, D. C., & Sarma, V. R. (1965). Structure of Hen Egg-White Lysozyme: A Three-dimensional Fourier Synthesis at 2 Å Resolution. *Nature 1965* 206:4986, 206(4986), 757–761. <https://doi.org/10.1038/206757a0>
- Bottou, L. (2010). Large-scale machine learning with stochastic gradient descent. *Proceedings of COMPSTAT 2010 - 19th International Conference on Computational Statistics, Keynote, Invited and Contributed Papers*, 177–186. https://doi.org/10.1007/978-3-7908-2604-3_16/COVER
- Bourgeois, D., & Royant, A. (2005). Advances in kinetic protein crystallography. *Current Opinion in Structural Biology*, 15(5), 538–547. <https://doi.org/10.1016/J.SBI.2005.08.002>
- Bourgeois, D., & Weik, M. (2008). Kinetic Protein Crystallography using Caged Compounds. In *Protein Science Encyclopedia* (pp. 410–434). Wiley-VCH Verlag GmbH & Co. KGaA. <https://doi.org/10.1002/9783527610754.fa19>
- Boutet, S., Cohen, A. E., & Wakatsuki, S. (2016). The New Macromolecular Femtosecond Crystallography (MFX) Instrument at LCLS. *Synchrotron Radiation News*, 29(1), 23–28. <https://doi.org/10.1080/08940886.2016.1124681>
- Boyd, S. E., Livermore, D. M., Hooper, D. C., & Hope, W. W. (2020). Metallo-β-Lactamases: Structure, Function, Epidemiology, Treatment Options, and the Development Pipeline. *Antimicrobial Agents and Chemotherapy*, 64(10). <https://doi.org/10.1128/AAC.00397-20>
- Bragg, M. W. L., Ragg, W. L. B., Communicated, B. A. (, Bragg, P. W. H., Friedrich, * W, Snippin, P., & Laue, M. (1913). The structure of some crystals as indicated by their diffraction of X-rays. *Proceedings of the Royal Society of London. Series A, Containing*

- Papers of a Mathematical and Physical Character*, 89(610), 248–277.
<https://doi.org/10.1098/RSPA.1913.0083>
- Bragg, W. H., & Bragg, W. L. (1913). The structure of the diamond. *Proceedings of the Royal Society of London. Series A, Containing Papers of a Mathematical and Physical Character*, 89(610), 277–291. <https://doi.org/10.1098/RSPA.1913.0084>
- Brandt Van Driel, T., Nelson, S., Armenta, R., Blaj, G., Boo, S., Boutet, S., Doering, D., Dragone, A., Hart, P., Haller, G., Kenney, C., Kwaitowski, M., Manger, L., Mckelvey, M., Nakahara, K., Oriunno, M., Sato, T., & Weaver, M. (2020). The ePix10k 2-megapixel hard X-ray detector at LCLS. *J. Synchrotron Rad*, 27, 608–615.
<https://doi.org/10.1107/S1600577520004257>
- Brenner, S., & Horne, R. W. (1959). A negative staining method for high resolution electron microscopy of viruses. *Biochimica et Biophysica Acta*, 34(C), 103–110.
[https://doi.org/10.1016/0006-3002\(59\)90237-9](https://doi.org/10.1016/0006-3002(59)90237-9)
- Broglie, L. de. (2009). XXXV. A tentative theory of light quanta. *The London, Edinburgh, and Dublin Philosophical Magazine and Journal of Science*, 47(278), 446–458.
<https://doi.org/10.1080/14786442408634378>
- Burgie, E. S., Bussell, A. N., Walker, J. M., Dubiel, K., & Vierstra, R. D. (2014). Crystal structure of the photosensing module from a red/far-red light-absorbing plant phytochrome. *Proceedings of the National Academy of Sciences of the United States of America*, 111(28), 10179–10184. <https://doi.org/10.1073/PNAS.1403096111/-/DCSUPPLEMENTAL>
- Burgie, E. S., Zhang, J., & Vierstra, R. D. (2016). Crystal Structure of Deinococcus Phytochrome in the Photoactivated State Reveals a Cascade of Structural Rearrangements during Photoconversion. *Structure*, 24(3), 448–457.
<https://doi.org/10.1016/J.STR.2016.01.001>
- Busch, H. (1926). Berechnung der Bahn von Kathodenstrahlen im axialsymmetrischen elektromagnetischen Felde. *Annalen Der Physik*, 386(25), 974–993.
<https://doi.org/10.1002/ANDP.19263862507>
- Bush, K., Macalintal, C., Rasmussen, B. A., Lee, V. J., & Yang, Y. (1993). Kinetic interactions of tazobactam with beta-lactamases from all major structural classes. *Antimicrobial Agents and Chemotherapy*, 37(4), 851–858. <https://doi.org/10.1128/AAC.37.4.851>
- Callaway, E. (2015). The revolution will not be crystallized: A new method sweeps through structural biology. *Nature*, 525(7568), 172–174. <https://doi.org/10.1038/525172A>
- Calvey, G. D., Katz, A. M., & Pollack, L. (2019). Microfluidic Mixing Injector Holder Enables Routine Structural Enzymology Measurements with Mix-and-Inject Serial Crystallography Using X-ray Free Electron Lasers. *Analytical Chemistry*, 91(11), 7139–7144.
<https://doi.org/10.1021/acs.analchem.9b00311>

- Calvey, G. D., Katz, A. M., Schaffer, C. B., & Pollack, L. (2016). Mixing injector enables time-resolved crystallography with high hit rate at X-ray free electron lasers. *Structural Dynamics*, 3(5). <https://doi.org/10.1063/1.4961971>
- Carrillo, M., Pandey, S., Sanchez, J., Noda, M., Poudyal, I., Aldama, L., Malla, T. N., Claesson, E., Wahlgren, W. Y., Feliz, D., Šrajcar, V., Maj, M., Castillon, L., Iwata, S., Nango, E., Tanaka, R., Tanaka, T., Fangjia, L., Tono, K., ... Schmidt, M. (2021). High-resolution crystal structures of transient intermediates in the phytochrome photocycle. *Structure (London, England : 1993)*, 29(7), 743. <https://doi.org/10.1016/J.STR.2021.03.004>
- Carslaw, H. S., & Jaeger, J. C. (1959). *Conduction of Heat in Solids* (2nd ed.). Oxford Science Publications.
- Chapman, H. N., Barty, A., Bogan, M. J., Boutet, S., Frank, M., Hau-Riege, S. P., Marchesini, S., Woods, B. W., Bajt, S., Benner, W. H., London, R. A., Plönjes, E., Kuhlmann, M., Treusch, R., Düsterer, S., Tschentscher, T., Schneider, J. R., Spiller, E., Möller, T., ... Hajdu, J. (2006). Femtosecond diffractive imaging with a soft-X-ray free-electron laser. *Nature Physics*, 2(12), 839–843. <https://doi.org/10.1038/nphys461>
- Chapman, H. N., Fromme, P., Barty, A., White, T. A., Kirian, R. A., Aquila, A., Hunter, M. S., Schulz, J., Deponte, D. P., Weierstall, U., Doak, R. B., Maia, F. R. N. C., Martin, A. V., Schlichting, I., Lomb, L., Coppola, N., Shoeman, R. L., Epp, S. W., Hartmann, R., ... Spence, J. C. H. (2011). Femtosecond X-ray protein nanocrystallography. *Nature*, 470(7332), 73–78. <https://doi.org/10.1038/nature09750>
- Cheng, Y., Grigorieff, N., Penczek, P. A., & Walz, T. (2015). A Primer to Single-Particle Cryo-Electron Microscopy. *Cell*, 161(3), 438–449. <https://doi.org/10.1016/J.CELL.2015.03.050>
- Claesson, E., Wahlgren, W. Y., Takala, H., Pandey, S., Castillon, L., Kuznetsova, V., Henry, L., Panman, M., Carrillo, M., Kübel, J., Nanekar, R., Isaksson, L., Nimmrich, A., Cellini, A., Morozov, D., Maj, M., Kurttila, M., Bosman, R., Nango, E., ... Westenhoff, S. (2020). The primary structural photoresponse of phytochrome proteins captured by a femtosecond X-ray laser. *ELife*, 9. <https://doi.org/10.7554/ELIFE.53514>
- Colunga Biancatelli, R. M. L., Berrill, M., & Marik, P. E. (2019). The antiviral properties of vitamin C. *Expert Review of Anti-infective Therapy*, 18(2), 99–101. <https://doi.org/10.1080/14787210.2020.1706483>
- Cui, J., Li, F., & Shi, Z. L. (2018). Origin and evolution of pathogenic coronaviruses. *Nature Reviews Microbiology* 2018 17:3, 17(3), 181–192. <https://doi.org/10.1038/s41579-018-0118-9>
- Dandey, V. P., Budell, W. C., Wei, H., Bobe, D., Maruthi, K., Kopylov, M., Eng, E. T., Kahn, P. A., Hinshaw, J. E., Kundu, N., Nimigean, C. M., Fan, C., Sukomon, N., Darst, S. A., Saecker, R. M., Chen, J., Malone, B., Potter, C. S., & Carragher, B. (2020). Time-resolved

- cryo-EM using Spotiton. *Nature Methods* 2020 17:9, 17(9), 897–900.
<https://doi.org/10.1038/s41592-020-0925-6>
- Dashti, A., Mashayekhi, G., Shekhar, M., Ben Hail, D., Salah, S., Schwander, P., des Georges, A., Singharoy, A., Frank, J., & Ourmazd, A. (2020). Retrieving functional pathways of biomolecules from single-particle snapshots. *Nature Communications*, 11(1).
<https://doi.org/10.1038/S41467-020-18403-X>
- De Rosier, D. J., & Klug, A. (1968). Reconstruction of Three Dimensional Structures from Electron Micrographs. *Nature* 1968 217:5124, 217(5124), 130–134.
<https://doi.org/10.1038/217130a0>
- Demain, A. L., & Vaishnav, P. (2009). Production of recombinant proteins by microbes and higher organisms. *Biotechnology Advances*, 27(3), 297–306.
<https://doi.org/10.1016/J.BIOTECHADV.2009.01.008>
- DePonte, D. P., Weierstall, U., Schmidt, K., Warner, J., Starodub, D., Spence, J. C. H., & Doak, R. B. (2008). Gas dynamic virtual nozzle for generation of microscopic droplet streams. *Journal of Physics D: Applied Physics*, 41(19), 195505. <https://doi.org/10.1088/0022-3727/41/19/195505>
- Dhara, A. K., & Nayak, A. K. (2022). Biological macromolecules: sources, properties, and functions. *Biological Macromolecules: Bioactivity and Biomedical Applications*, 3–22.
<https://doi.org/10.1016/B978-0-323-85759-8.00005-1>
- Dobson, C. M. (2003). Protein folding and misfolding. *Nature* 2003 426:6968, 426(6968), 884–890. <https://doi.org/10.1038/nature02261>
- Dods, R., Båth, P., Morozov, D., Gagnér, V. A., Arnlund, D., Luk, H. L., Kübel, J., Maj, M., Vallejos, A., Wickstrand, C., Bosman, R., Beyerlein, K. R., Nelson, G., Liang, M., Milathianaki, D., Robinson, J., Harimoorthy, R., Berntsen, P., Malmerberg, E., ... Neutze, R. (2020). Ultrafast structural changes within a photosynthetic reaction centre. *Nature* 2020 589:7841, 589(7841), 310–314. <https://doi.org/10.1038/s41586-020-3000-7>
- Drawz, S. M., & Bonomo, R. A. (2010). Three decades of beta-lactamase inhibitors. *Clinical Microbiology Reviews*, 23(1), 160–201. <https://doi.org/10.1128/CMR.00037-09>
- Dubochet, J., & McDowell, A. W. (1981). VITRIFICATION OF PURE WATER FOR ELECTRON MICROSCOPY. *Journal of Microscopy*, 124(3), 3–4.
<https://doi.org/10.1111/J.1365-2818.1981.TB02483.X>
- Eberhardt, J., Santos-Martins, D., Tillack, A. F., & Forli, S. (2021). AutoDock Vina 1.2.0: New Docking Methods, Expanded Force Field, and Python Bindings. *Journal of Chemical Information and Modeling*, 61(8), 3891–3898.
https://doi.org/10.1021/ACS.JCIM.1C00203/SUPPL_FILE/CI1C00203_SI_002.ZIP

- Elder, F. R., Gurewitsch, A. M., Langmuir, R. V., & Pollock, H. C. (1947). Radiation from Electrons in a Synchrotron. *Physical Review*, 71(11), 829. <https://doi.org/10.1103/PhysRev.71.829.5>
- Elings, W., Tassoni, R., van der Schoot, S. A., Luu, W., Kynast, J. P., Dai, L., Blok, A. J., Timmer, M., Florea, B. I., Pannu, N. S., & Ubbink, M. (2017). Phosphate Promotes the Recovery of Mycobacterium tuberculosis β -Lactamase from Clavulanic Acid Inhibition. *Biochemistry*, 56(47), 6257–6267. https://doi.org/10.1021/ACS.BIOCHEM.7B00556/ASSET/IMAGES/LARGE/BI-2017-00556R_0007.JPEG
- Ellen Jo Baron James H. Jorgensen, M. L. L., & Murray, M. A. P. W. P. R. (2007). Manual of Clinical Microbiology. In *Clinical Infectious Diseases* (9th ed., Issue 1). ASM press. <https://doi.org/10.1086/524076>
- Emma, P., Akre, R., Arthur, J., Bionta, R., Bostedt, C., Bozek, J., Brachmann, A., Bucksbaum, P., Coffee, R., Decker, F. J., Ding, Y., Dowell, D., Edstrom, S., Fisher, A., Frisch, J., Gilevich, S., Hastings, J., Hays, G., Hering, P., ... Galayda, J. (2010). First lasing and operation of an ångstrom-wavelength free-electron laser. *Nature Photonics* 2010 4:9, 4(9), 641–647. <https://doi.org/10.1038/nphoton.2010.176>
- Emsley, P., Lohkamp, B., Scott, W. G., & Cowtan, K. (2010). Features and development of Coot. *Urn:Issn:0907-4449*, 66(4), 486–501. <https://doi.org/10.1107/S0907444910007493>
- Fair, R. J., & Tor, Y. (2014). Antibiotics and Bacterial Resistance in the 21st Century. *Perspectives in Medicinal Chemistry*, 6(6), PMC.S14459. <https://doi.org/10.4137/PMC.S14459>
- Feiler, C., Fisher, A. C., Boock, J. T., Marrichi, M. J., Wright, L., Schmidpeter, P. A. M., Blankenfeldt, W., Pavelka, M., & DeLisa, M. P. (2013). Directed Evolution of Mycobacterium tuberculosis β -Lactamase Reveals Gatekeeper Residue That Regulates Antibiotic Resistance and Catalytic Efficiency. *PLOS ONE*, 8(9), e73123. <https://doi.org/10.1371/JOURNAL.PONE.0073123>
- Ferreira, L. G., Dos Santos, R. N., Oliva, G., & Andricopulo, A. D. (2015). Molecular Docking and Structure-Based Drug Design Strategies. *Molecules*, 20(7), 13384. <https://doi.org/10.3390/MOLECULES200713384>
- Fowler Iii, A. A., Kim, C., Lepler, L., Malhotra, R., Debesa, O., Natarajan, R., Fisher, B. J., Syed, A., DeWilde, C., Priday, A., & Kasirajan, V. (2017). Intravenous vitamin C as adjunctive therapy for enterovirus/rhinovirus induced acute respiratory distress syndrome. *World Journal of Critical Care Medicine*, 6(1), 85–90. <https://doi.org/10.5492/wjccm.v6.i1.85>
- Frank, J. (1975). Averaging of low exposure electron micrographs of non-periodic objects. *Ultramicroscopy*, 1(2), 159–162. [https://doi.org/10.1016/S0304-3991\(75\)80020-9](https://doi.org/10.1016/S0304-3991(75)80020-9)

- French, S., & Wilson, K. (1978). On the treatment of negative intensity observations. *Urn:Issn:0567-7394*, 34(4), 517–525. <https://doi.org/10.1107/S0567739478001114>
- Friedrich, W., Knipping, P., & Laue, M. (1913). Interferenzerscheinungen bei Röntgenstrahlen. *Annalen Der Physik*, 346(10), 971–988. <https://doi.org/10.1002/andp.19133461004>
- Furuya, A., Uozaki, M., Yamasaki, H., Arakawa, T., Arita, M., & Koyama, A. H. (2008). Antiviral effects of ascorbic and dehydroascorbic acids in vitro. *International Journal of Molecular Medicine*, 22(4), 541–545. https://doi.org/10.3892/IJMM_00000053/HTML
- Garman, E. F., & Owen, R. L. (2006). Cryocooling and radiation damage in macromolecular crystallography. *Acta Crystallographica Section D: Biological Crystallography*, 62(1), 32–47. <https://doi.org/10.1107/S0907444905034207>
- Genick, U. K., Borgstahl, G. E. O., Ng, K., Ren, Z., Pradervand, C., Burke, P. M., Šrajer, V., Teng, T. Y., Schildkamp, W., McRee, D. E., Moffat, K., & Getzoff, E. D. (1997). Structure of a protein photocycle intermediate by millisecond time-resolved crystallography. *Science*, 275(5305), 1471–1475. <https://doi.org/10.1126/SCIENCE.275.5305.1471/ASSET/AE45F94F-13BD-4F3E-900E-BC6E441A6620/ASSETS/GRAPHIC/SE0774791004.JPEG>
- Giacovazzo, Carmelo. (1992). *Fundamentals of crystallography*. 654. <https://www.scribd.com/doc/86472833/Fundamentals-of-Crystallography-Giacovazzo-2000>
- Givens, R., Kotala, M. B., & Lee, J.-I. (2005). Mechanistic Overview of Phototriggers and Cage Release. In *Dynamic Studies in Biology* (pp. 95–129). Wiley-VCH Verlag GmbH & Co. KGaA. <https://doi.org/10.1002/3527605592.ch2>
- Gorrec, F. (2021). A beginner's guide to macromolecular crystallization. *The Biochemist*, 43(1), 36–43. https://doi.org/10.1042/BIO_2020_108
- Grabowski, M., Cooper, D. R., Brzezinski, D., Macnar, J. M., Shabalin, I. G., Cymborowski, M., Otwinowski, Z., & Minor, W. (2021). Synchrotron radiation as a tool for macromolecular X-Ray Crystallography: A XXI century perspective. *Nuclear Instruments and Methods in Physics Research, Section B: Beam Interactions with Materials and Atoms*, 489, 30–40. <https://doi.org/10.1016/j.nimb.2020.12.016>
- Haas, D. J. (1968). X-ray studies on lysozyme crystals at -50°C . *IUCrJ*, 24(4), 604–604. <https://doi.org/10.1107/S056774086800292X>
- Haas, D. J. (2020). The early history of cryo-cooling for macromolecular crystallography. *IUCrJ*, 7(2), 148–157. <https://doi.org/10.1107/S2052252519016993>
- Helfand, M. S., Totir, M. A., Carey, M. P., Hujer, A. M., Bonomo, R. A., & Carey, P. R. (2003). Following the Reactions of Mechanism-Based Inhibitors with β -Lactamase by Raman

- Crystallography. *Biochemistry*, 42(46), 13386–13392.
https://doi.org/10.1021/BI035716W/SUPPL_FILE/BI035716W_S.PDF
- Helliwell, J. R. (1992). Macromolecular Crystallography with Synchrotron Radiation. *Macromolecular Crystallography with Synchrotron Radiation*.
<https://doi.org/10.1017/CBO9780511524264>
- Henderson, R. (1990). Cryo-protection of protein crystals against radiation damage in electron and X-ray diffraction. *Proceedings of the Royal Society of London. Series B: Biological Sciences*, 241(1300), 6–8. <https://doi.org/10.1098/RSPB.1990.0057>
- Henderson, R. (1995). The potential and limitations of neutrons, electrons and X-rays for atomic resolution microscopy of unstained biological molecules. *Quarterly Reviews of Biophysics*, 28(2), 171–193. <https://doi.org/10.1017/S003358350000305X>
- Henry, E. R., & Hofrichter, J. (1992). [8] Singular value decomposition: Application to analysis of experimental data. *Methods in Enzymology*, 210(C), 129–192.
[https://doi.org/10.1016/0076-6879\(92\)10010-B](https://doi.org/10.1016/0076-6879(92)10010-B)
- Herzik, M. A., Wu, M., & Lander, G. C. (2017). Achieving better than 3 Å resolution by single particle cryo-EM at 200 keV. *Nature Methods*, 14(11), 1075.
<https://doi.org/10.1038/NMETH.4461>
- Hess, G. P., & Rupley, J. A. (1971). Structure and function of proteins. *Annual Review of Biochemistry*, 40, 1013–1044. <https://doi.org/10.1146/ANNUREV.BI.40.070171.005053>
- Holton, J., & Alber, T. (2004). Automated protein crystal structure determination using ELVES. *Proceedings of the National Academy of Sciences of the United States of America*, 101(6), 1537–1542. <https://doi.org/10.1073/PNAS.0306241101>
- Hope, H. (1988). Cryocrystallography of biological macromolecules: a generally applicable method. *Acta Crystallographica Section B*, 44(1), 22–26.
<https://doi.org/10.1107/S0108768187008632>
- Hosseinizadeh, A., Breckwoldt, N., Fung, R., Sepehr, R., Schmidt, M., Schwander, P., Santra, R., & Ourmazd, A. (2021). Few-fs resolution of a photoactive protein traversing a conical intersection. *Nature* 2021 599:7886, 599(7886), 697–701. <https://doi.org/10.1038/s41586-021-04050-9>
- Huang, Z., & Kim, K. J. (2007). Review of x-ray free-electron laser theory. In *Physical Review Special Topics - Accelerators and Beams* (Vol. 10, Issue 3, p. 34801). American Physical Society. <https://doi.org/10.1103/PhysRevSTAB.10.034801>
- Hugonnet, J. E., & Blanchard, J. S. (2007). Irreversible inhibition of the Mycobacterium tuberculosis β -lactamase by clavulanate. *Biochemistry*, 46(43), 11998–12004.
https://doi.org/10.1021/BI701506H/SUPPL_FILE/BI701506H-FILE002.PDF

- Hunter, M. S., Segelke, B., Messerschmidt, M., Williams, G. J., Zatsepin, N. A., Barty, A., Henry Benner, W., Carlson, D. B., Coleman, M., Graf, A., Hau-Riege, S. P., Pardini, T., Marvin Seibert, M., Evans, J., Boutet, S., & Frank, M. (2014). Fixed-target protein serial microcrystallography with an x-ray free electron laser. *Scientific Reports* 2014 4:1, 4(1), 1–5. <https://doi.org/10.1038/srep06026>
- Hwu, Y., & Margaritondo, G. (2021). Synchrotron radiation and X-ray free-electron lasers (X-FELs) explained to all users, active and potential. *Urn:Issn:1600-5775*, 28(3), 1014–1029. <https://doi.org/10.1107/S1600577521003325>
- Ihee, H., Rajagopal, S., Srajer, V., Pahl, R., Anderson, S., Schmidt, M., Schotte, F., Anfinrud, P. A., Wulff, M., & Moffat, K. (2005). Visualizing reaction pathways in photoactive yellow protein from nanoseconds to seconds. *Proceedings of the National Academy of Sciences of the United States of America*, 102(20), 7145–7150. https://doi.org/10.1073/PNAS.0409035102/SUPPL_FILE/09035FIG9.JPG
- Ileri, N., Çalik, P., & Şengül, A. (2007). Phosphate enrichment and fed-batch operation for prolonged β -lactamase production by *Bacillus licheniformis*. *Journal of Applied Microbiology*, 102(5), 1418–1426. <https://doi.org/10.1111/J.1365-2672.2006.03163.X>
- Jamison, D. A., Anand Narayanan, S., Trovão, N. S., Guarnieri, J. W., Topper, M. J., Moraes-Vieira, P. M., Zaksas, V., Singh, K. K., Wurtele, E. S., & Beheshti, A. (2022). A comprehensive SARS-CoV-2 and COVID-19 review, Part 1: Intracellular overdrive for SARS-CoV-2 infection. *European Journal of Human Genetics* 2022 30:8, 30(8), 889–898. <https://doi.org/10.1038/s41431-022-01108-8>
- Joachimiak, A., Wilamowski, M., Sherrell, D., Kim, Y., Lavens, A., Henning, R., Lazarski, K., Shigemoto, A., Endres, M., Maltseva, N., Babnigg, G., & Burdette, S. (2022). *Time-Resolved β -lactam Cleavage by L1 Metallo- β -Lactamase*. <https://doi.org/10.21203/RS.3.RS-1514248/V1>
- Jones, R. N., Wilson, H. W., Thornsberry, C., & Barry, A. L. (1985). In vitro antimicrobial activity of cefoperazone-sulbactam combinations against 554 clinical isolates including a review and beta-lactamase studies. *Diagnostic Microbiology and Infectious Disease*, 3(6), 489–499. [https://doi.org/10.1016/S0732-8893\(85\)80005-5](https://doi.org/10.1016/S0732-8893(85)80005-5)
- Jumper, J., Evans, R., Pritzel, A., Green, T., Figurnov, M., Ronneberger, O., Tunyasuvunakool, K., Bates, R., Židek, A., Potapenko, A., Bridgland, A., Meyer, C., Kohl, S. A. A., Ballard, A. J., Cowie, A., Romera-Paredes, B., Nikolov, S., Jain, R., Adler, J., ... Hassabis, D. (2021). Highly accurate protein structure prediction with AlphaFold. *Nature* 2021 596:7873, 596(7873), 583–589. <https://doi.org/10.1038/s41586-021-03819-2>
- Jung, Y. O., Lee, J. H., Kim, J., Schmidt, M., Moffat, K., Šrajer, V., & Ihee, H. (2013). Volume-conserving trans–cis isomerization pathways in photoactive yellow protein visualized by picosecond X-ray crystallography. *Nature Chemistry* 2013 5:3, 5(3), 212–220. <https://doi.org/10.1038/nchem.1565>

- Kabsch, W. (2014). Processing of X-ray snapshots from crystals in random orientations. *Acta Crystallographica. Section D, Biological Crystallography*, 70(Pt 8), 2204–2216. <https://doi.org/10.1107/S1399004714013534>
- Keenan, A. K., Gal, A., Levitzki, A., Biophys, B., Waldo, G. L., Northrup, J. K., Perkins, J. P., Harden, T. K., MITCHELL Guss, J., MERRIT, E. A., Paul Phizackerley, R., Hedman, Brit., Murata, M., & Freeman, Han. C. (1988). Phase Determination by Multiple-Wavelength X-Ray Diffraction: Crystal Structure of a Basic ‘Blue’ Copper Protein from Cucumbers. *Science*, 241(4867), 806–811. <https://doi.org/10.1126/SCIENCE.3406739>
- Kendrew, J. C., Bodo, G., Dintzis, H. M., Parrish, R. G., Wyckoff, H., & Phillips, D. C. (1958). A three-dimensional model of the myoglobin molecule obtained by x-ray analysis. *Nature*, 181(4610), 662–666. <https://doi.org/10.1038/181662a0>
- Kendrew, J. C., Dickerson, R. E., Strandberg, B. E., Hart, R. G., Davies, D. R., Phillips, D. C., & Shore, V. C. (1960). Structure of myoglobin: A three-dimensional Fourier synthesis at 2 Å resolution. *Nature*, 185(4711), 422–427. <https://doi.org/10.1038/185422A0>
- Kirian, R. A., White, T. A., Holton, J. M., Chapman, H. N., Fromme, P., Barty, A., Lomb, L., Aquila, A., Maia, F. R. N. C., Martin, A. V., Fromme, R., Wang, X., Hunter, M. S., Schmidt, K. E., & Spence, J. C. H. (2011). Structure-factor analysis of femtosecond microdiffraction patterns from protein nanocrystals. *Acta Crystallographica. Section A, Foundations of Crystallography*, 67(Pt 2), 131–140. <https://doi.org/10.1107/S0108767310050981>
- Klose, C., Venezia, F., Hussong, A., Kircher, S., Schäfer, E., & Fleck, C. (2015). Systematic analysis of how phytochrome B dimerization determines its specificity. *Nature Plants* 2015 1:7, 1(7), 1–9. <https://doi.org/10.1038/nplants.2015.90>
- Kneller, D. W., Phillips, G., O’Neill, H. M., Jedrzejczak, R., Stols, L., Langan, P., Joachimiak, A., Coates, L., & Kovalevsky, A. (2020). Structural plasticity of SARS-CoV-2 3CL Mpro active site cavity revealed by room temperature X-ray crystallography. *Nature Communications* 2020 11:1, 11(1), 1–6. <https://doi.org/10.1038/s41467-020-16954-7>
- Kojadinovic, M., Laugraud, A., Vuillet, L., Fardoux, J., Hannibal, L., Adriano, J. M., Bouyer, P., Giraud, E., & Verméglio, A. (2008). Dual role for a bacteriophytochrome in the bioenergetic control of *Rhodospseudomonas palustris*: Enhancement of photosystem synthesis and limitation of respiration. *Biochimica et Biophysica Acta (BBA) - Bioenergetics*, 1777(2), 163–172. <https://doi.org/10.1016/J.BBABIO.2007.09.003>
- Kupitz, C., Olmos, J. L., Holl, M., Tremblay, L., Pande, K., Pandey, S., Oberthür, D., Hunter, M., Liang, M., Aquila, A., Tenboer, J., Calvey, G., Katz, A., Chen, Y., Wiedorn, M. O., Knoska, J., Meents, A., Majriani, V., Norwood, T., ... Schmidt, M. (2017). Structural enzymology using X-ray free electron lasers. *Structural Dynamics*, 4(4), 44003. <https://doi.org/10.1063/1.4972069>

- Lewis, K. (2013). Platforms for antibiotic discovery. In *Nature Reviews Drug Discovery* (Vol. 12, Issue 5, pp. 371–387). *Nat Rev Drug Discov*. <https://doi.org/10.1038/nrd3975>
- Liang, M., Williams, G. J., Messerschmidt, M., Seibert, M. M., Montanez, P. A., Hayes, M., Milathianaki, D., Aquila, A., Hunter, M. S., Koglin, J. E., Schafer, D. W., Guillet, S., Busse, A., Bergan, R., Olson, W., Fox, K., Stewart, N., Curtis, R., Miahnahri, A. A., & Boutet, S. (2015). The Coherent X-ray Imaging instrument at the Linac Coherent Light Source. *Urn:Issn:1600-5775*, 22(3), 514–519. <https://doi.org/10.1107/S160057751500449X>
- Liebschner, D., Afonine, P. V., Baker, M. L., Bunkoczi, G., Chen, V. B., Croll, T. I., Hintze, B., Hung, L. W., Jain, S., McCoy, A. J., Moriarty, N. W., Oeffner, R. D., Poon, B. K., Prisant, M. G., Read, R. J., Richardson, J. S., Richardson, D. C., Sammito, M. D., Sobolev, O. V., ... Adams, P. D. (2019). Macromolecular structure determination using X-rays, neutrons and electrons: Recent developments in Phenix. *Acta Crystallographica Section D: Structural Biology*, 75(10), 861–877. <https://doi.org/10.1107/S2059798319011471>
- Liebschner, D., Afonine, P. V., Moriarty, N. W., Poon, B. K., Sobolev, O. V., Terwilliger, T. C., & Adams, P. D. (2017). Polder maps: Improving OMIT maps by excluding bulk solvent. *Acta Crystallographica Section D: Structural Biology*, 73(2), 148–157. <https://doi.org/10.1107/S2059798316018210/BA5254SUP1.PDF>
- Lieuvin, M. (1994). Commissioning of the European Synchrotron Radiation Facility Magnets. *IEEE Transactions on Magnetics*, 30(4), 1555–1562. <https://doi.org/10.1109/20.305561>
- Long, F., Nicholls, R. A., Emsley, P., Gražulis, S., Merkys, A., Vaitkus, A., & Murshudov, G. N. (2017). AceDRG: A stereochemical description generator for ligands. *Acta Crystallographica Section D: Structural Biology*, 73(2), 112–122. <https://doi.org/10.1107/S2059798317000067/BA5260SUP2.TXT>
- Luheshi, L. M., Crowther, D. C., & Dobson, C. M. (2008). Protein misfolding and disease: from the test tube to the organism. *Current Opinion in Chemical Biology*, 12(1), 25–31. <https://doi.org/10.1016/J.CBPA.2008.02.011>
- Lupkin, S. (2022, February 1). Feds' contract with Pfizer for Paxlovid has some surprises. *NPR*.
- Madey, J. M. J. (1971). Stimulated emission of bremsstrahlung in a periodic magnetic field. *Journal of Applied Physics*, 42(5), 1906–1913. <https://doi.org/10.1063/1.1660466>
- Mair, D. B. (1926). The Crystal as Diffraction Grating. *Nature* 1926 117:2935, 117(2935), 157–158. <https://doi.org/10.1038/117157b0>
- Makrides, S. C. (1996). Strategies for achieving high-level expression of genes in *Escherichia coli*. *Microbiological Reviews*, 60(3), 512–538. <https://doi.org/10.1128/MR.60.3.512-538.1996>

- Malla, T. N. (2020). *RAPID DIFFUSION OBSERVED IN MICROCRYSTALS BY X-RAY FREE ELECTRON LASER MIX-AND-INJECT SERIAL CRYSTALLOGRAPHY*.
- Malla, T. N. (2023). *pySVD4TX*. <https://doi.org/10.5281/ZENODO.8206588>
- Malla, T. N., Pandey, S., Aldama, L., Feliz, D., Noda, M., Poudyal, I., Phillips, G. N., Stojković, E. A., & Schmidt, M. (2021). Vitamin C Binds to SARS Coronavirus-2 Main Protease Essential for Viral Replication. *BioRxiv*, 2021.05.02.442358. <https://doi.org/10.1101/2021.05.02.442358>
- Malla, T. N., Pandey, S., Poudyal, I., Feliz, D., Noda, M., Phillips, G., Stojkovic, E., & Schmidt, M. (2020). Ebselen reacts with SARS coronavirus-2 main protease crystals. In *bioRxiv*. <https://doi.org/10.1101/2020.08.10.244525>
- Malla, T. N., Zielinski, K., Aldama, L., Bajt, S., Feliz, D., Hayes, B., Hunter, M., Kupitz, C., Lisova, S., Knoska, J., Martin-Garcia, J., Mariani, V., Pandey, S., Poudyal, I., Sierra, R. G., Tolstikova, A., Yefanov, O., Yoon, C. H., Ourmazd, A., ... Schmidt, M. (2023). Heterogeneity in the M. tuberculosis β -lactamase inhibition by Sulbactam. *BioRxiv*, 2022.12.06.519319. <https://doi.org/10.1101/2022.12.06.519319>
- Mariani, V., Morgan, A., Yoon, C. H., Lane, T. J., White, T. A., O'grady, C., Kuhn, M., Aplin, S., Koglin, J., Barty, A., & Chapman, H. N. (2016). OnDA: online data analysis and feedback for serial X-ray imaging. *Journal of Applied Crystallography*, 49(Pt 3), 1073. <https://doi.org/10.1107/S1600576716007469>
- Marina, A., Waldburger, C. D., & Hendrickson, W. A. (2005). Structure of the entire cytoplasmic portion of a sensor histidine-kinase protein. *The EMBO Journal*, 24(24), 4247–4259. <https://doi.org/10.1038/SJ.EMBOJ.7600886>
- McCoy, A. J., Grosse-Kunstleve, R. W., Adams, P. D., Winn, M. D., Storoni, L. C., & Read, R. J. (2007). Phaser crystallographic software. *Urn:Issn:0021-8898*, 40(4), 658–674. <https://doi.org/10.1107/S0021889807021206>
- McPherson, A. (1991). A brief history of protein crystal growth. *Journal of Crystal Growth*, 110(1–2), 1–10. [https://doi.org/10.1016/0022-0248\(91\)90859-4](https://doi.org/10.1016/0022-0248(91)90859-4)
- McPherson, A., & Gavira, J. A. (2014). Introduction to protein crystallization. *Acta Crystallographica. Section F, Structural Biology Communications*, 70(Pt 1), 2. <https://doi.org/10.1107/S2053230X13033141>
- Mehrabi, P., Schulz, E. C., Dsouza, R., Müller-Werkmeister, H. M., Tellkamp, F., Dwayne Miller, R. J., & Pai, E. F. (2019). Time-resolved crystallography reveals allosteric communication aligned with molecular breathing. *Science*, 365(6458), 1167–1170. https://doi.org/10.1126/SCIENCE.AAW9904/SUPPL_FILE/AAW9904S1.MP4

- Milazzo, A. C., Cheng, A., Moeller, A., Lyumkis, D., Jacovetty, E., Polukas, J., Ellisman, M. H., Xuong, N. H., Carragher, B., & Potter, C. S. (2011). Initial evaluation of a direct detection device detector for single particle cryo-electron microscopy. *Journal of Structural Biology*, 176(3), 404–408. <https://doi.org/10.1016/J.JSB.2011.09.002>
- Millane, R. P. (1990). Phase retrieval in crystallography and optics. *Journal of The Optical Society of America A-Optics Image Science and Vision*, 7(3), 394–411. <https://doi.org/10.1364/JOSAA.7.000394>
- Minor, W., Cymborowski, M., Otwinowski, Z., & Chruszcz, M. (2006). HKL-3000: the integration of data reduction and structure solution – from diffraction images to an initial model in minutes. *Urn:Issn:0907-4449*, 62(8), 859–866. <https://doi.org/10.1107/S0907444906019949>
- Moffat, K. (1989). Time-Resolved Macromolecular Crystallography. *Annual Review of Biophysics and Biophysical Chemistry*, 18, 309–332. <https://doi.org/10.1146/ANNUREV.BB.18.060189.001521>
- Moffat, K. (2001). Time-resolved biochemical crystallography: A mechanistic perspective. *Chemical Reviews*, 101(6), 1569–1581. <https://doi.org/10.1021/cr990039q>
- Moffat, K. (2006). Laue crystallography: time-resolved studies. *International Tables for Crystallography*, 167–176. <https://doi.org/10.1107/97809553602060000670>
- Moffat, K. (2014). Time-resolved crystallography and protein design: Signalling photoreceptors and optogenetics. In *Philosophical Transactions of the Royal Society B: Biological Sciences* (Vol. 369, Issue 1647). Royal Society of London. <https://doi.org/10.1098/rstb.2013.0568>
- Moffat, K. (2019). Laue diffraction and time-resolved crystallography: a personal history. *Philosophical Transactions. Series A, Mathematical, Physical, and Engineering Sciences*, 377(2147), 20180243. <https://doi.org/10.1098/RSTA.2018.0243>
- Moffat, K., Szebenyi, D., & Bilderback, D. (1984). X-ray Laue Diffraction from Protein Crystals. *Science*, 223(4643), 1423–1425. <https://doi.org/10.1126/SCIENCE.223.4643.1423>
- Monaco, S., Gordon, E., Bowler, M. W., Delagenière, S., Guijarro, M., Spruce, D., Svensson, O., Mcsweeney, S. M., Mccarthy, A. A., Leonard, G., & Nanao, M. H. (2013). Automatic processing of macromolecular crystallography X-ray diffraction data at the ESRF. *Urn:Issn:0021-8898*, 46(3), 804–810. <https://doi.org/10.1107/S0021889813006195>
- Monteiro, D. C. F., Amoah, E., Rogers, C., & Pearson, A. R. (2021). Using photocaging for fast time-resolved structural biology studies. *Urn:Issn:2059-7983*, 77(10), 1218–1232. <https://doi.org/10.1107/S2059798321008809>
- Munro, I. H. (1997). Synchrotron Radiation Research in the UK. *IUCrJ*, 4(6), 344–358. <https://doi.org/10.1107/S090904959701176X>

- Muralidharan, N., Sakthivel, R., Velmurugan, D., & Gromiha, M. M. (2020). Computational studies of drug repurposing and synergism of lopinavir, oseltamivir and ritonavir binding with SARS-CoV-2 protease against COVID-19. *Journal of Biomolecular Structure and Dynamics*, 39(7), 2673–2678. <https://doi.org/10.1080/07391102.2020.1752802>
- Murray, P. R., Rosenthal, K. S., & Michael A. Pfaller. (2020). Medical Microbiology. In *Angewandte Chemie International Edition*, 6(11), 951–952. (9th ed.). Elsevier.
- Murshudov, G. N., Skubák, P., Lebedev, A. A., Pannu, N. S., Steiner, R. A., Nicholls, R. A., Winn, M. D., Long, F., & Vagin, A. A. (2011). REFMAC5 for the refinement of macromolecular crystal structures. *Acta Crystallographica. Section D, Biological Crystallography*, 67(Pt 4), 355–367. <https://doi.org/10.1107/S0907444911001314>
- Naas, T., Oueslati, S., Bonnin, R. A., Dabos, M. L., Zavala, A., Dortet, L., Retailleau, P., & Iorga, B. I. (2017). Beta-lactamase database (BLDB)—structure and function. *Journal of Enzyme Inhibition and Medicinal Chemistry*, 32(1), 917–919. https://doi.org/10.1080/14756366.2017.1344235/SUPPL_FILE/IENZ_A_1344235_SM8111.PDF
- Nagatani, A. (2010). Phytochrome: structural basis for its functions. *Current Opinion in Plant Biology*, 13(5), 565–570. <https://doi.org/10.1016/J.PBI.2010.07.002>
- Nelson, D. L., & Cox, M. M. (2017). *Lehninger Principles of Biochemistry* (7th ed.). W. H. Freeman.
- Netzer, W. J., & Hartl, F. U. (1998). Protein folding in the cytosol: Chaperonin-dependent and -independent mechanisms. *Trends in Biochemical Sciences*, 23(2), 68–73. [https://doi.org/10.1016/S0968-0004\(97\)01171-7](https://doi.org/10.1016/S0968-0004(97)01171-7)
- Neutzo, R., Wouts, R., Van Der Spoel, D., Weckert, E., & Hajdu, J. (2000). Potential for biomolecular imaging with femtosecond X-ray pulses. *Nature*, 406(6797), 752–757. <https://doi.org/10.1038/35021099>
- Olmos, J. L., Pandey, S., Martin-Garcia, J. M., Calvey, G., Katz, A., Knoska, J., Kupitz, C., Hunter, M. S., Liang, M., Oberthuer, D., Yefanov, O., Wiedorn, M., Heyman, M., Holl, M., Pande, K., Barty, A., Miller, M. D., Stern, S., Roy-Chowdhury, S., ... Schmidt, M. (2018). Enzyme intermediates captured ‘on the fly’ by mix-and-inject serial crystallography. *BMC Biology*, 16(1), 59. <https://doi.org/10.1186/s12915-018-0524-5>
- Otero, L. H., Klinke, S., Rinaldi, J., Velázquez-Escobar, F., Mroginski, M. A., Fernández López, M., Malamud, F., Vojnov, A. A., Hildebrandt, P., Goldbaum, F. A., & Bonomi, H. R. (2016). Structure of the Full-Length Bacteriophytochrome from the Plant Pathogen *Xanthomonas campestris* Provides Clues to its Long-Range Signaling Mechanism. *Journal of Molecular Biology*, 428(19), 3702–3720. <https://doi.org/10.1016/J.JMB.2016.04.012>

- Padayatti, P. S., Helfand, M. S., Totir, M. A., Carey, M. P., Carey, P. R., Bonomo, R. A., & van den Akker, F. (2005). High resolution crystal structures of the trans-enamine intermediates formed by sulbactam and clavulanic acid and E166A SHV-1 {beta}-lactamase. *The Journal of Biological Chemistry*, 280(41), 34900–34907. <https://doi.org/10.1074/JBC.M505333200>
- Palzkill, T. (2013). Metallo- β -lactamase structure and function. *Annals of the New York Academy of Sciences*, 1277(1), 91. <https://doi.org/10.1111/J.1749-6632.2012.06796.X>
- Pande, K., Hutchison, C. D. M., Groenhof, G., Aquila, A., Robinson, J. S., Tenboer, J., Basu, S., Boutet, S., DePonte, D. P., Liang, M., White, T. A., Zatsepin, N. A., Yefanov, O., Morozov, D., Oberthuer, D., Gati, C., Subramanian, G., James, D., Zhao, Y., ... Schmidt, M. (2016). Femtosecond structural dynamics drives the trans/cis isomerization in photoactive yellow protein. *Science*, 352(6286), 725–729. <https://doi.org/10.1126/science.aad5081>
- Pandey, S., Bean, R., Sato, T., Poudyal, I., Bielecki, J., Cruz Villarreal, J., Yefanov, O., Mariani, V., White, T. A., Kupitz, C., Hunter, M., Abdellatif, M. H., Bajt, S., Bondar, V., Echelmeier, A., Doppler, D., Emons, M., Frank, M., Fromme, R., ... Schmidt, M. (2019). Time-resolved serial femtosecond crystallography at the European XFEL. *Nature Methods* 2019 17:1, 17(1), 73–78. <https://doi.org/10.1038/s41592-019-0628-z>
- Pandey, S., Calvey, G., Katz, A. M., Malla, T. N., Koua, F. H. M., Martin-Garcia, J. M., Poudyal, I., Yang, J. H., Vakili, M., Yefanov, O., Zielinski, K. A., Bajt, S., Awel, S., Doerner, K., Frank, M., Gelisio, L., Jernigan, R., Kirkwood, H., Kloos, M., ... Schmidt, M. (2021). Observation of substrate diffusion and ligand binding in enzyme crystals using high-repetition-rate mix-and-inject serial crystallography. *Urn:Issn:2052-2525*, 8(6), 878–895. <https://doi.org/10.1107/S2052252521008125>
- Pauling, L. (1971). Vitamin C and Common Cold. *JAMA*, 216(2), 332–332. <https://doi.org/10.1001/JAMA.1971.03180280086025>
- Penczek, P. A. (2010). Image Restoration in Cryo-electron Microscopy. *Methods in Enzymology*, 482(C), 35. [https://doi.org/10.1016/S0076-6879\(10\)82002-6](https://doi.org/10.1016/S0076-6879(10)82002-6)
- Phillips, J. C., Wlodawer, A., Yevitz, M. M., & Hodgson, K. O. (1976). Applications of synchrotron radiation to protein crystallography: preliminary results. *Proceedings of the National Academy of Sciences of the United States of America*, 73(1), 128. <https://doi.org/10.1073/PNAS.73.1.128>
- Popa, I., & Berkovich, R. (2023). *Mechanical Unfolding Response of Proteins*. <https://doi.org/10.1021/ACSINFOCUS.7E7015>
- Punjani, A., Rubinstein, J. L., Fleet, D. J., & Brubaker, M. A. (2017). cryoSPARC: algorithms for rapid unsupervised cryo-EM structure determination. *Nature Methods* 2017 14:3, 14(3), 290–296. <https://doi.org/10.1038/nmeth.4169>

- Raicu, V., & Popescu, A. (2008). Integrated molecular and cellular biophysics. In *Integrated Molecular and Cellular Biophysics*. Springer Netherlands. <https://doi.org/10.1007/978-1-4020-8268-9>
- Rayment, I. (2002). Small-Scale Batch Crystallization of Proteins Revisited: An Underutilized Way to Grow Large Protein Crystals. *Structure*, *10*(2), 147–151. [https://doi.org/10.1016/S0969-2126\(02\)00711-6](https://doi.org/10.1016/S0969-2126(02)00711-6)
- Ren, Z., Bourgeois, D., Helliwell, J. R., Moffat, K., Šrajer, V., & Stoddard, B. L. (1999). Laue crystallography: coming of age. *Urn:Issn:0909-0495*, *6*(4), 891–917. <https://doi.org/10.1107/S0909049599006366>
- Ren, Z., Perman, B., Šrajer, V., Teng, T. Y., Pradervand, C., Bourgeois, D., Schotte, F., Ursby, T., Kort, R., Wulff, M., & Moffat, K. (2001a). A molecular movie at 1.8 Å resolution displays the photocycle of photoactive yellow protein, a eubacterial blue-light receptor, from nanoseconds to seconds. *Biochemistry*, *40*(46), 13788–13801. https://doi.org/10.1021/BI0107142/SUPPL_FILE/BI0107142_S.PDF
- Ren, Z., Perman, B., Šrajer, V., Teng, T. Y., Pradervand, C., Bourgeois, D., Schotte, F., Ursby, T., Kort, R., Wulff, M., & Moffat, K. (2001b). A molecular movie at 1.8 Å resolution displays the photocycle of photoactive yellow protein, a eubacterial blue-light receptor, from nanoseconds to seconds. *Biochemistry*, *40*(46), 13788–13801. <https://doi.org/10.1021/BI0107142>
- Robinson, I., Gruebel, G., & Mochrie, S. (2010). Focus on X-ray Beams with High Coherence. *New Journal of Physics*, *12*(3), 035002. <https://doi.org/10.1088/1367-2630/12/3/035002>
- Roessler, C. G., Agarwal, R., Allaire, M., Alonso-Mori, R., Andi, B., Bachega, J. F. R., Bommer, M., Brewster, A. S., Browne, M. C., Chatterjee, R., Cho, E., Cohen, A. E., Cowan, M., Datwani, S., Davidson, V. L., Defever, J., Eaton, B., Ellson, R., Feng, Y., ... Zouni, A. (2016). Acoustic Injectors for Drop-On-Demand Serial Femtosecond Crystallography. *Structure*, *24*(4), 631–640. <https://doi.org/10.1016/J.STR.2016.02.007>
- Rohou, A., & Grigorieff, N. (2015). CTFFIND4: Fast and accurate defocus estimation from electron micrographs. *Journal of Structural Biology*, *192*(2), 216. <https://doi.org/10.1016/J.JSB.2015.08.008>
- Röntgen, W. C. (1898). Ueber eine neue Art von Strahlen. *Annalen Der Physik*, *300*(1), 1–11. <https://doi.org/10.1002/ANDP.18983000102>
- Rosenbaum, G., Alkire, R. W., Evans, G., Rotella, F. J., Lazarski, K., Zhang, R. G., Ginell, S. L., Duke, N., Naday, I., Lazarz, J., Molitsky, M. J., Keefe, L., Gonczy, J., Rock, L., Sanishvili, R., Walsh, M. A., Westbrook, E., & Joachimiak, A. (2006). The Structural Biology Center 19ID undulator beamline: facility specifications and protein crystallographic results. *Journal of Synchrotron Radiation*, *13*(Pt 1), 30. <https://doi.org/10.1107/S0909049505036721>

- Rosenthal, P. B., & Henderson, R. (2003). Optimal determination of particle orientation, absolute hand, and contrast loss in single-particle electron cryomicroscopy. *Journal of Molecular Biology*, 333(4), 721–745. <https://doi.org/10.1016/j.jmb.2003.07.013>
- Rossmann, M. G. (1990). The molecular replacement method. *IUCrJ*, 46(2), 73–82. <https://doi.org/10.1107/S0108767389009815>
- Rupp, B., & Wang, J. (2004). Predictive models for protein crystallization. *Methods*, 34(3), 390–407. <https://doi.org/10.1016/j.ymeth.2004.03.031>
- Ruska, E. (1934). über Fortschritte im Bau und in der Leistung des magnetischen Elektronenmikroskops. *Zeitschrift Für Physik*, 87(9–10), 580–602. <https://doi.org/10.1007/BF01333326/METRICS>
- Ruska, E., & Knoll, M. (1931). Die magnetische Sammelspule für schnelle Elektronenstrahlen. *The Magnetic Concentrating Coil for Fast Electron Beams.* *Z. Techn. Physik*, 12, 389–400.
- Ruska, H., Borries, B. v., & Ruska, E. (1939). Die Bedeutung der Übermikroskopie für die Virusforschung. *Archiv Für Die Gesamte Virusforschung*, 1(1), 155–169. <https://doi.org/10.1007/BF01243399/METRICS>
- Sanchez, J. C., Carrillo, M., Pandey, S., Noda, M., Aldama, L., Feliz, D., Claesson, E., Wahlgren, W. Y., Tracy, G., Duong, P., Nugent, A. C., Field, A., Šrajcar, V., Kupitz, C., Iwata, S., Nango, E., Tanaka, R., Tanaka, T., Fangjia, L., ... Stojković, E. A. (2019). High-resolution crystal structures of a myxobacterial phytochrome at cryo and room temperatures. *Structural Dynamics*, 6(5), 054701. <https://doi.org/10.1063/1.5120527>
- Sauter, N. K., Hattne, J., Grosse-Kunstleve, R. W., & Echols, N. (2013). New Python-based methods for data processing. *Acta Crystallographica. Section D, Biological Crystallography*, 69(Pt 7), 1274–1282. <https://doi.org/10.1107/S0907444913000863>
- Scheres, S. H. W. (2015). Semi-automated selection of cryo-EM particles in RELION-1.3. *Journal of Structural Biology*, 189(2), 114. <https://doi.org/10.1016/J.JSB.2014.11.010>
- Schlichting, I., Almo, S. C., Rapp, G., Wilson, K., Petratos, K., Lentfer, A., Wittinghofer, A., Kabsch, W., Pai, E. F., Petsko, G. A., & Goody, R. S. (1990). Time-resolved X-ray crystallographic study of the conformational change in Ha-Ras p21 protein on GTP hydrolysis. *Nature* 1990 345:6273, 345(6273), 309–315. <https://doi.org/10.1038/345309a0>
- Schmidt, M. (2013). Mix and inject: Reaction initiation by diffusion for time-resolved macromolecular crystallography. *Advances in Condensed Matter Physics*, 2013. <https://doi.org/10.1155/2013/167276>
- Schmidt, M. (2019). Time-Resolved Macromolecular Crystallography at Pulsed X-ray Sources. *International Journal of Molecular Sciences*, 20(6), 1401. <https://doi.org/10.3390/ijms20061401>

- Schmidt, M. (2020). Reaction Initiation in Enzyme Crystals by Diffusion of Substrate. *Crystals*, 10(2), 116. <https://doi.org/10.3390/cryst10020116>
- Schmidt, M., Pahl, R., Srajer, V., Anderson, S., Ren, Z., Ihee, H., Rajagopal, S., & Moffat, K. (2004). Protein kinetics: Structures of intermediates and reaction mechanism from time-resolved x-ray data. *Proceedings of the National Academy of Sciences of the United States of America*, 101(14), 4799–4804. https://doi.org/10.1073/PNAS.0305983101/SUPPL_FILE/05983FIG8.JPG
- Schmidt, M., Rajagopal, S., Ren, Z., & Moffat, K. (2003). Application of singular value decomposition to the analysis of time-resolved macromolecular x-ray data. *Biophysical Journal*, 84(3), 2112–2129. [https://doi.org/10.1016/S0006-3495\(03\)75018-8](https://doi.org/10.1016/S0006-3495(03)75018-8)
- Schotte, F., Cho, H. S., Kaila, V. R. I., Kamikubo, H., Dashdorj, N., Henry, E. R., Graber, T. J., Henning, R., Wulff, M., Hummer, G., Kataoka, M., & Anfinrud, P. A. (2012). Watching a signaling protein function in real time via 100-ps time-resolved Laue crystallography. *Proceedings of the National Academy of Sciences of the United States of America*, 109(47), 19256–19261. https://doi.org/10.1073/PNAS.1210938109/SUPPL_FILE/SM04.MP4
- Schotte, F., Lim, M., Jackson, T. A., Smirnov, A. V., Soman, J., Olson, J. S., Phillips, G. N., Wulff, M., & Anfinrud, P. A. (2003). Watching a protein as it functions with 150-ps time-resolved x-ray crystallography. *Science (New York, N.Y.)*, 300(5627), 1944–1947. <https://doi.org/10.1126/SCIENCE.1078797>
- Sharrock, R. A., & Clack, T. (2004). Heterodimerization of type II phytochromes in Arabidopsis. *Proceedings of the National Academy of Sciences of the United States of America*, 101(31), 11500–11505. https://doi.org/10.1073/PNAS.0404286101/SUPPL_FILE/04286FIG8.PDF
- Shaw, P. J., & Rawlins, D. J. (1991). The point-spread function of a confocal microscope: its measurement and use in deconvolution of 3-D data. *Journal of Microscopy*, 163(2), 151–165. <https://doi.org/10.1111/J.1365-2818.1991.TB03168.X>
- Sierra, R. G., Gati, C., Laksmono, H., Dao, E. H., Gul, S., Fuller, F., Kern, J., Chatterjee, R., Ibrahim, M., Brewster, A. S., Young, I. D., Michels-Clark, T., Aquila, A., Liang, M., Hunter, M. S., Koglin, J. E., Boutet, S., Junco, E. A., Hayes, B., ... DeMirci, H. (2015). Concentric-flow electrokinetic injector enables serial crystallography of ribosome and photosystem II. *Nature Methods* 2016 13:1, 13(1), 59–62. <https://doi.org/10.1038/nmeth.3667>
- Skarina, T., Xu, X., Evdokimova, E., & Savchenko, A. (2014). High-throughput crystallization screening. *Methods in Molecular Biology*, 1140, 159–168. https://doi.org/10.1007/978-1-4939-0354-2_12/COVER
- Smith, H. (2000). Phytochromes and light signal perception by plants—an emerging synthesis. *Nature* 2000 407:6804, 407(6804), 585–591. <https://doi.org/10.1038/35036500>

- Šrajer, V., Teng, T. Y., Ursby, T., Pradervand, C., Ren, Z., Adachi, S. I., Schildkamp, W., Bourgeois, D., Wulff, M., & Moffat, K. (1996). Photolysis of the Carbon Monoxide Complex of Myoglobin: Nanosecond Time-Resolved Crystallography. *Science*, *274*(5293), 1726–1729. <https://doi.org/10.1126/SCIENCE.274.5293.1726>
- Stagno, J. R., Liu, Y., Bhandari, Y. R., Conrad, C. E., Panja, S., Swain, M., Fan, L., Nelson, G., Li, C., Wendel, D. R., White, T. A., Coe, J. D., Wiedorn, M. O., Knoska, J., Oberthuer, D., Tuckey, R. A., Yu, P., Dyba, M., Tarasov, S. G., ... Wang, Y. X. (2017). Structures of riboswitch RNA reaction states by mix-and-inject XFEL serial crystallography. *Nature*, *541*(7636), 242. <https://doi.org/10.1038/NATURE20599>
- Steinfeld, J. I., Francisco, J. Salvadore., & Hase, W. L. (1998). *Chemical Kinetics and Dynamics (2nd Edition)*. 560. https://books.google.com/books/about/Chemical_Kinetics_and_Dynamics.html?id=I1jwAA AMAAJ
- Stevens, R. C. (2000). Design of high-throughput methods of protein production for structural biology. *Structure*, *8*(9), R177–R185. [https://doi.org/10.1016/S0969-2126\(00\)00193-3](https://doi.org/10.1016/S0969-2126(00)00193-3)
- Stoddard, B. L., Cohen, B. E., Brubaker, M., Mesecar, A. D., & Koshland, D. E. (1998). Millisecond Laue structures of an enzyme–product complex using photocaged substrate analogs. *Nature Structural Biology* *1998 5:10*, *5*(10), 891–897. <https://doi.org/10.1038/2331>
- Takala, H., Björling, A., Berntsson, O., Lehtivuori, H., Niebling, S., Hoernke, M., Kosheleva, I., Henning, R., Menzel, A., Ihalainen, J. A., & Westenhoff, S. (2014). Signal amplification and transduction in phytochrome photosensors. *Nature* *2014 509:7499*, *509*(7499), 245–248. <https://doi.org/10.1038/nature13310>
- Talluri, S. (2020). Molecular Docking and Virtual Screening Based Prediction of Drugs for COVID-19. *Combinatorial Chemistry & High Throughput Screening*, *24*(5), 716–728. <https://doi.org/10.2174/1386207323666200814132149>
- Tassoni, R., Blok, A., Pannu, N. S., & Ubbink, M. (2019). New Conformations of Acylation Adducts of Inhibitors of β -Lactamase from Mycobacterium tuberculosis. *Biochemistry*, *58*(7). <https://doi.org/10.1021/ACS.BIOCHEM.8B01085>
- Taylor, G. (2003). The phase problem. *Acta Crystallographica. Section D, Biological Crystallography*, *59*(Pt 11), 1881–1890. <https://doi.org/10.1107/S0907444903017815>
- Tenboer, J., Basu, S., Zatsepin, N., Pande, K., Milathianaki, D., Frank, M., Hunter, M., Boutet, S., Williams, G. J., Koglin, J. E., Oberthuer, D., Heymann, M., Kupitz, C., Conrad, C., Coe, J., Roy-Chowdhury, S., Weierstall, U., James, D., Wang, D., ... Schmidt, M. (2014). Time-resolved serial crystallography captures high-resolution intermediates of photoactive yellow protein. *Science*, *346*(6214), 1242–1246. https://doi.org/10.1126/SCIENCE.1259357/SUPPL_FILE/TENBOER.SM.PDF

- Teng, T.-Y. (1990). Mounting of crystals for macromolecular crystallography in a free-standing thin film. *Journal of Applied Crystallography*, 23(5), 387–391. <https://doi.org/10.1107/S0021889890005568>
- Thomson, J. J. (1897). XL. Cathode Rays . *The London, Edinburgh, and Dublin Philosophical Magazine and Journal of Science*, 44(269), 293–316. <https://doi.org/10.1080/14786449708621070>
- Tosha, T., Nomura, T., Nishida, T., Saeki, N., Okubayashi, K., Yamagiwa, R., Sugahara, M., Nakane, T., Yamashita, K., Hirata, K., Ueno, G., Kimura, T., Hisano, T., Muramoto, K., Sawai, H., Takeda, H., Mizohata, E., Yamashita, A., Kanematsu, Y., ... Kubo, M. (2017). Capturing an initial intermediate during the P450_{nor} enzymatic reaction using time-resolved XFEL crystallography and caged-substrate. *Nature Communications* 2017 8:1, 8(1), 1–9. <https://doi.org/10.1038/s41467-017-01702-1>
- Totir, M. A., Helfand, M. S., Carey, M. P., Sheri, A., Buynak, J. D., Bonomo, R. A., & Carey, P. R. (2007). Sulbactam forms only minimal amounts of irreversible acrylate-enzyme with SHV-1 β -lactamase. *Biochemistry*, 46(31), 8980–8987. https://doi.org/10.1021/BI7006146/SUPPL_FILE/BI7006146-FILE002.PDF
- Tremblay, L. W., Hugonnet, J. E., & Blanchard, J. S. (2008). Structure of the covalent adduct formed between Mycobacterium tuberculosis β -lactamase and clavulanate. *Biochemistry*, 47(19), 5312–5316. https://doi.org/10.1021/BI8001055/SUPPL_FILE/BI8001055-FILE001.PDF
- Tremblay, L. W., Xu, H., & Blanchard, J. S. (2010). Structures of the Michaelis complex (1.2 Å) and the covalent acyl intermediate (2.0 Å) of cefamandole bound in the active sites of the mycobacterium tuberculosis β -lactamase K73A and E166A mutants. *Biochemistry*, 49(45), 9685–9687. <https://doi.org/10.1021/bi1015088>
- Unwin, N., & Fujiyoshi, Y. (2012). Gating Movement of Acetylcholine Receptor Caught by Plunge-Freezing. *Journal of Molecular Biology*, 422(5), 617–634. <https://doi.org/10.1016/J.JMB.2012.07.010>
- Urzhumtsev, A. G., & Lunin, V. Y. (2019). Introduction to crystallographic refinement of macromolecular atomic models. *Https://Doi.Org/10.1080/0889311X.2019.1631817*, 25(3), 164–262. <https://doi.org/10.1080/0889311X.2019.1631817>
- Von Laue, M., Wagner, E. H., & Chako, N. (1962). Röntgenstrahlinterferenzen. *Physics Today*, 15(8), 54–54. <https://doi.org/10.1063/1.3058327>
- Wagner, T., Merino, F., Stabrin, M., Moriya, T., Antoni, C., Apelbaum, A., Hagel, P., Sitsel, O., Raisch, T., Prumbaum, D., Quentin, D., Roderer, D., Tacke, S., Siebolds, B., Schubert, E., Shaikh, T. R., Lill, P., Gatsogiannis, C., & Raunser, S. (2019). SPHIRE-crYOLO is a fast and accurate fully automated particle picker for cryo-EM. *Communications Biology*, 2(1). <https://doi.org/10.1038/S42003-019-0437-Z>

- Walsh, C. (2000). Molecular mechanisms that confer antibacterial drug resistance. In *Nature* (Vol. 406, Issue 6797, pp. 775–781). Nature Publishing Group.
<https://doi.org/10.1038/35021219>
- Wang, F., Cassidy, C., & Sacchettini, J. C. (2006). Crystal structure and activity studies of the *Mycobacterium tuberculosis* β -lactamase reveal its critical role in resistance to β -lactam antibiotics. *Antimicrobial Agents and Chemotherapy*, 50(8), 2762–2771.
<https://doi.org/10.1128/AAC.00320-06/ASSET/88CFA3E1-1430-475D-A7A6-01489A063279/ASSETS/GRAPHIC/ZAC0080659600007.JPEG>
- Weierstall, U. (2014). Liquid sample delivery techniques for serial femtosecond crystallography. *Philosophical Transactions of the Royal Society B: Biological Sciences*, 369(1647).
<https://doi.org/10.1098/RSTB.2013.0337>
- Weierstall, U., James, D., Wang, C., White, T. A., Wang, D., Liu, W., Spence, J. C. H., Bruce Doak, R., Nelson, G., Fromme, P., Fromme, R., Grotjohann, I., Kupitz, C., Zatsepin, N. A., Liu, H., Basu, S., Wacker, D., Won Han, G., Katritch, V., ... Cherezov, V. (2014). Lipidic cubic phase injector facilitates membrane protein serial femtosecond crystallography. *Nature Communications* 2014 5:1, 5(1), 1–6. <https://doi.org/10.1038/ncomms4309>
- White, T. A. (2019). Processing serial crystallography data with crystFEL: A step-by-step guide. *Acta Crystallographica Section D: Structural Biology*, 75(2), 219–233.
<https://doi.org/10.1107/S205979831801238X/BA5291SUP2.TXT>
- White, T. A., Kirian, R. A., Martin, A. V., Aquila, A., Nass, K., Barty, A., & Chapman, H. N. (2012). CrystFEL: A software suite for snapshot serial crystallography. *Journal of Applied Crystallography*, 45(2), 335–341. <https://doi.org/10.1107/S0021889812002312>
- WHO Coronavirus (COVID-19) Dashboard With Vaccination Data.* (2023).
<https://covid19.who.int/>
- Wimberly, B. T., Brodersen, D. E., Clemons, W. M., Morgan-Warren, R. J., Carter, A. P., Vornrhein, C., Hartsch, T., & Ramakrishnan, V. (2000). Structure of the 30S ribosomal subunit. *Nature* 2000 407:6802, 407(6802), 327–339. <https://doi.org/10.1038/35030006>
- Winn, M. D., Ballard, C. C., Cowtan, K. D., Dodson, E. J., Emsley, P., Evans, P. R., Keegan, R. M., Krissinel, E. B., Leslie, A. G. W., McCoy, A., McNicholas, S. J., Murshudov, G. N., Pannu, N. S., Potterton, E. A., Powell, H. R., Read, R. J., Vagin, A., & Wilson, K. S. (2011). Overview of the CCP4 suite and current developments. *Acta Crystallographica. Section D, Biological Crystallography*, 67(Pt 4), 235–242.
<https://doi.org/10.1107/S0907444910045749>
- Woitowich, N. C., Halavaty, A. S., Waltz, P., Kupitz, C., Valera, J., Tracy, G., Gallagher, K. D., Claesson, E., Nakane, T., Pandey, S., Nelson, G., Tanaka, R., Nango, E., Mizohata, E., Owada, S., Tono, K., Joti, Y., Nugent, A. C., Patel, H., ... Stojković, E. A. (2018). Structural basis for light control of cell development revealed by crystal structures of a

myxobacterial phytochrome. *Urn:Issn:2052-2525*, 5(5), 619–634.
<https://doi.org/10.1107/S2052252518010631>

World Health Organization. (2021). Global tuberculosis report. *Global Tuberculosis Report*.
<https://www.who.int/teams/global-tuberculosis-programme/tb-reports/global-tuberculosis-report-2021>

Xie, H., Mire, J., Kong, Y., Chang, M., Hassounah, H. A., Thornton, C. N., Sacchetti, J. C., Cirillo, J. D., & Rao, J. (2012). Rapid point-of-care detection of the tuberculosis pathogen using a BlaC-specific fluorogenic probe. *Nature Chemistry* 2012 4:10, 4(10), 802–809.
<https://doi.org/10.1038/nchem.1435>

Yang, Y., Janota, K., Tabei, K., Huang, N., Siegel, M. M., Lin, Y.-I., Rasmussen, B. A., & Shlaes, D. M. (2000). Mechanism of Inhibition of the Class A β -Lactamases PC1 and TEM-1 by Tazobactam: OBSERVATION OF REACTION PRODUCTS BY ELECTROSPRAY IONIZATION MASS SPECTROMETRY. *Journal of Biological Chemistry*, 275(35), 26674–26682. [https://doi.org/10.1016/S0021-9258\(19\)61429-8](https://doi.org/10.1016/S0021-9258(19)61429-8)

Yefanov, O., Mariani, V., Gati, C., White, T. A., Chapman, H. N., Barty, A., Chapman, H. N., Fromme, P., Barty, A., White, T. A., Kirian, R. A., Aquila, A., Hunter, M. S., Schulz, J., DePonte, D. P., Weierstall, U., Doak, R. B., N C Maia, F. R., Martin, A. V., ... Marsh, B. (2015). Accurate determination of segmented X-ray detector geometry. *Optics Express*, Vol. 23, Issue 22, Pp. 28459-28470, 23(22), 28459–28470.
<https://doi.org/10.1364/OE.23.028459>

Young, J. Y., Berrisford, J., & Chen, M. (2021). A new era of synchrotron-enabled macromolecular crystallography. *Nature Methods* 2021 18:5, 18(5), 433–434.
<https://doi.org/10.1038/s41592-021-01146-y>

Zhao, Y., & Schmidt, M. (2009). New software for the singular value decomposition of time-resolved crystallographic data. *Urn:Issn:0021-8898*, 42(4), 734–740.
<https://doi.org/10.1107/S0021889809019050>

Zhu, Y., Ouyang, Q., & Mao, Y. (2017). A deep convolutional neural network approach to single-particle recognition in cryo-electron microscopy. *BMC Bioinformatics*, 18(1).
<https://doi.org/10.1186/S12859-017-1757-Y>

Curriculum Vitae

Tek Narsingh Malla, PhD

Department of Physics, University of Wisconsin-Milwaukee, Milwaukee, WI, 53211
tmalla@uwm.edu | (414) 530-8123

Education

- 2023 Ph.D in Physics (Biophysics focus), University of Wisconsin-Milwaukee (UWM)
Dissertation: Time-Resolved Investigations on Biological Macromolecules
- 2020 MSc in Physics, UWM
Thesis: Rapid Diffusion Observed in Microcrystals by X-ray Free Electron Laser
Mix-and- Inject Serial Crystallography
- 2017 BSc in Applied Physics, Kathmandu University (KU), Dhulikhel, Nepal

Fellowships and awards

- 2023, 2019 David Lichtman Research Fellowship, UWM
- For outstanding research in experimental physics at the Department of Physics
- 2022 – 2023 Distinguished Dissertator Fellowship, UWM
- For achieving dissertator status with academically excellent record. Competed campus wide following department nomination.
- 2021 Semifinalist at the Reach Out Science Slams, Museum of Science, Boston, USA
- For telling science story to general public in three minutes. A YouTube video is available at <https://www.youtube.com/watch?v=O90heEufIOs>
- 2018 – 2023 Physics Research Excellence Award, UWM
- For outstanding research performed in the Department of Physics
- 2018 – 2023 Chancellor's Graduate Student Award, UWM
- For academic excellence at UWM
- 2013 – 2017 KU School of Science Merit Based Scholarship
- Awarded semesterly for students with highest grades in the class
- 2017 Korea Government Invitation Program (KGIP) Award, Korean Embassy in Nepal
- For best performance in after school Korean language class and assisting Korean volunteers with translation and local community coordination
- 2017 Korean Overseas Volunteers Association (KOVA) scholarship
- Same as above

Invited talks

- Sep 2023 *Heterogeneity in M. tuberculosis β -lactamase Inhibition by Sulbactam*
SSRL/LCLS Users' Meeting, SLAC National Accelerator Laboratory, California, USA
- Aug 2023 *Analysis of Mix-and-Inject Serial Crystallography Time-Resolved Data with Singular Value Decomposition*
Workshop on "Novel data methods for crystallography and beyond" conducted at the 26th Congress and General Assembly of the IUCr, Melbourne, Australia
- May 2023 *Heterogeneity in M. tuberculosis β -lactamase inhibition by sulbactam*
BioXFEL 10th Annual International Conference, Puerto Rico, USA

- May 2023 *Visualizing Biological Molecules in Action*
UWM Physics Symposium, Wisconsin, USA
- Sep 2022 *Pushing the Time Resolution of Mix-and-Inject Serial Crystallography to the Limit*
SSRL/LCLS Users' Meeting (virtual)
- Apr 2021 *Structure Determination of Biological Macromolecules at Atomic Resolution*
UWM Physics Symposium (virtual)

Poster presentations

- Jun 2023 *Probing Magnetically Triggered Reactions in Proteins Using Time-Resolved Crystallography*
Ultrafast X-ray Summer School, Hamburg, Germany
*This won the first prize for a mock proposal competition where we proposed a viable experiment that can be conducted at the European X-ray Free Electron Laser.
- Oct 2022 *Diversity in β -lactamase Inhibition by Sulbactam*
Aspects of Imaging, Diffraction, and Crystallography, Arizona, USA
- Mar 2022 *Fundamental Events of the Z to E Isomerization Reaction of a Bacterial Red-Light Photoreceptor*
Gordon Research Conference: Photosensory Receptors and Signal Transduction, California, USA
- Feb 2022 *Pushing the Time Resolution of Mix-and-Inject Serial Crystallography to the Limit*
BioXFEL 9th Annual International Conference (virtual)
*Best poster award
- Dec 2021 *Mix-and-Inject Serial Crystallography at the X-ray Free Electron Lasers*
Pacifichem: The International Chemical Congress of Pacific Basin Societies (virtual)
- May 2021 *Time-Resolved Enzymology to Capture a Full Catalytic Series*
PDB 50th Anniversary Symposium (virtual)
- Feb 2021 *Time-Resolved Investigation on β -lactamase Reacting with an Inhibitor*
BioXFEL 8th Annual International Conference (virtual)
- Jan 2020 *Pushing XFEL Single-Particle Imaging Towards Near-Atomic Resolution*
BioXFEL 7th Annual International Conference, Puerto Rico, USA
- Nov 2019 *Proteins and Enzymes: How Many Single-Particle Snapshots we Need?*
Nature Conference: Functional dynamics – Visualizing Molecules in Action, Arizona, USA

Manuscripts under review

- 2023 *Signal transduction within a bacterial photoreceptor enzyme revealed by Cryo-EM*
T. N. Malla, Joshua Mendez, David Menendez, Dorina Bizhga, Carolina Hernandez, Srinivasan Muniyappan, Peter Schwander, E. Stojkovic, M. Schmidt
Science (2023), submitted
- 2023 *KINNTREX: A Neural Network Unveils Protein Mechanism from Time Resolved X-ray Crystallography*
G. Biener, **T.N. Malla**, P. Schwander, M. Schmidt
IUCrJ (2023), Under review

Peer reviewed publications

- 2023 *Femtosecond conformational changes in a photolyase guide long-range electron transfer as resolved by serial crystallography*
A. Cellini, M. Shankar, A. Nimmrich, J. Mutisya, A. Furrer, E. Beale, M. Carrillo, **T. N. Malla**, P. Maj, L. Vrhovac, F. Dworkowski, C. Cirelli, P. Johnson, D. Ozerov, C. Bacellar, J. Standfuss, M. Schmidt, T. Weinert, J. Ihalainen, W. Wahlgren, S. Westenhoff
Nature Chemistry (2023), accepted for publication

- 2023 *Heterogeneity in the M. tuberculosis β -Lactamase Inhibition by Sulbactam*
T. N. Malla, K. Zielinski, L. Aldama, S. Bajt, D. Feliz, B. Hayes, M. Hunter, C. Kupitz, S. Lisova, J. Knoska, J. Martin-Garcia, V. Mariani, S. Pandey, I. Poudyal, R. G. Sierra, A. Tolstikova, O. Yefanov, C. H. Yoon, A. Ourmazd, P. Fromme, P. Schwander, A. Barty, H. N. Chapman, E. A. Stojkovic, A. Batyuk, S. Boutet, G. N. Phillips Jr., L. Pollack, M. Schmidt
 Nature Communications (2023) Vol 14, 5507
- 2022 *Transient State Measurements on Proteins by Time-Resolved Crystallography*
T.N. Malla, M. Schmidt
 Current Opinion in Structural Biology (2022) Vol 74, 102376
- 2022 *Optical, Structural and Thermal Performances of Black Nickel Selective Coating based Solar Thermal Collectors*
 B. P. Kafle, B. Basnet, B. Timalisina, A. Deo, **T. N. Malla**, N. Acharya, A. Adhikari
 Solar Energy (2022) Vol 234, 262-274
- 2021 *Observation of Substrate Diffusion and Ligand Binding in Enzyme Crystals Using High-repetition Rate Mix-and-Inject Serial Crystallography*
 S. Pandey, G. Calvey, A. M. Katz, **T. N. Malla**, F. H. M. Koua, I. Poudyal, J.H. Yang, M. Vakili, J. Martin-Garcia, O. Yefanov, K. A. Zielinski, S. Bajt, K. Doerner, M. Frank, L. Gelesio, R. Jernigan, M. Kloos, V. Mariani, M. D. Miller, G. Nelson, J. Olmos, A. Ourmazd, A. Sadri, A. Salah, A. Tolstikova, J. Spence, P. Schwander, A. Barty, H. Chapman, P. Fromme, A. Mancuso, G. Phillips, R. Bean, L. Pollack, M. Schmidt
 IUCrJ (2021) Vol 8, Part 6, 878-895
- 2021 *High-resolution Crystal Structures of Transient Intermediates in the Phytochrome Photocycle*
 M. Carrillo, S. Pandey, J. Sanchez, M. Noda, I. Poudyal, L. Aldama, **T. N. Malla**, E. Claesson, W. Yuan Wahlgren, D. Feliz, V. Šrajcar, M. Maj, L. Castillon, S. Iwata, E. Nango, R. Tanaka, T. Tanaka, L. Fangjia, K. Tono, S. Owada, S. Westenhoff, E. A. Stojkovic, M. Schmidt
 Structure (2021) Vol 29, Issue 7, 743-754
- 2020 *Pump-Probe Time-Resolved Serial Femtosecond Crystallography at X-Ray Free Electron Lasers*
 S. Pandey; I. Poudyal; **T.N. Malla*** [co-corresponding author]
 Crystals (2020) Vol 10, Issue 7, 628

Preprints and manuscripts under preparation

- 2023 *Fundamental Events of the Z to E Isomerization Reaction of a Bacterial Red-Light Photoreceptor*
T. N. Malla, L. Aldama, D. Feliz, V. Leon, H. Hu, I. Thomas, A. Cellini, A. Nimmrich, S. Botha, R. Sierra, M. Hunter, F. Potevin, R. Jernigan, C. Kupitz, M. Lady, A. Tolstikova, V. Mariani, A. Barty, F. Moss, S. Boutet, P. Schwander, P. Fromme, S. Westenhoff, E. Stojkovic, M. Schmidt
 to be submitted to Proceedings of the National Academy of Sciences
- 2021 *Vitamin C Binds to SARS Coronavirus-2 Main Protease Essential for Viral Replication*
T. N. Malla, S. Pandey, I. Poudyal, L. Aldama, D. Feliz, M. Noda, G. Phillips, E. Stojkovic, M. Schmidt
 BioRxiv
- 2020 *Ebselen Reacts with SARS Coronavirus-2 Main Protease Crystals*
T.N. Malla, S. Pandey, I. Poudyal, D. Feliz, M. Noda, G. Phillips, E. Stojkovic, M. Schmidt
 BioRxiv